TEMPORAL AND DYNAMICAL SPECTRAL ANALYSIS OF SELECT NARROW LINE SEYFERT 1 GALAXIES

by

Andrew Cargill Liebmann

A dissertation submitted in partial fulfillment
of the requirements for the degree

of

Doctor of Philosophy

in

Physics

MONTANA STATE UNIVERSITY
Bozeman, Montana

November, 2010

APPROVAL

of a dissertation submitted by

Andrew Cargill Liebmann

This dissertation has been read by each member of the dissertation committee and has been found to be satisfactory regarding content, English usage, format, citations, bibliographic style, and consistency, and is ready for submission to the Division of Graduate Education.

Dr. Sachiko Tsuruta

Approved for the Department of Physics

Dr. Richard Smith

Approved for the Division of Graduate Education

Dr. Carl A. Fox

STATEMENT OF PERMISSION TO USE

Andrew Cargill Liebmann

November, 2010

ACKNOWLEDGEMENTS

While there are far too many to thank in the given space, I would like to thank those who have really been of great help. Professor Sachiko Tsuruta, her for years of guidance, patience and expertise. Professor Hideyo Kunieda and Dr Yoshito Haba of Nagoya University for their help with NGC 4051 and Mrk 766 and being wonderful hosts. Professor Masaaki Takahashi and Dr Rohta Takahashi for help in numerous fields. Dr Dirk Grupe for the IRAS F12397+3333 data, the recommendation of Mrk 766 and his enthusiasm. Dr. Keigo Fukumura for the recommendation of NGC 4051. Dr. Marcu Teter for a fortuitous introduction. My committee, Doctors Neil Cornish, Piet Martens, John Carlsten, Charles Kankelborg and Suzanne Christopher for their hard work as educators and helping me improve my dissertation. And finally my parents without whom none of this would be possible because of their support and help when it was needed. To those friends, family, teachers, collaborators, and inspirers I have not mentioned, thank you.

TABLE OF CONTENTS

TABLE OF CONTENTS – CONTINUED

LIST OF TABLES

LIST OF TABLES – CONTINUED

Table Page

LIST OF FIGURES

LIST OF FIGURES – CONTINUED

Figure Page

LIST OF FIGURES – CONTINUED

Figure Page

LIST OF FIGURES – CONTINUED

Figure Page

LIST OF FIGURES – CONTINUED

Figure Page

LIST OF FIGURES – CONTINUED

Figure Page

ABSTRACT

Presented is the detailed analysis of three Narrow Line Seyfert 1 galaxies using the method of dynamical spectral analysis. These are NGC 4051, IRAS F12397+3333 and Mrk 766.

The highly variable NGC 4051 exhibits some dramatic changes over the course of two observations. These dramatic changes are attributed to a variable emission region being partially covered by a fixed, thick absorbing cloud. A unique time region was found where the emission region becomes smaller than the absorbing cloud. Source enters a true minimal phase and appears quite stable, appearing to "turn off." When in its lowest flux states NGC 4051 has a thermal plasma feature suggesting starburst activity in the nucleus. The possibility of starburst activity proves an important link in the understanding of the evolution of Active Galactic Nuclei.

IRAS F12397+3333, a little studied source, was found to possess a complex, dusty, warm absorber spectrum of helium- and hydrogen-like carbon, nitrogen, oxygen, neon and several ionic species of iron. This is similar to the spectrum of IRAS 13349+2348. A two-phase gas was used to model this spectrum. The location of the gas is consistent with being located in the narrow line region.

Two types of variability were found in the rapidly varying Mrk 766. The long-term variability and its associated spectral flattening seen in two observations are caused by a thick partially covering cloud and variable emission region. However the average spectral behavior shows partial covering of a thinner cloud. The result is a "lumpy cloud." When the source is dim a thicker portion of the clouds covers it, but as the source brightens and enlarges the thinner portion plays a more dominant role in the covering. The short, rapid variability is caused by the combination of a highly variable power law component and a stable reflected component, referred to here as ionized relativistic reflection. Finally, some unique flares were discovered. Unlike the other flares seen in the lightcurves, these occur only in the 0.3-2.0 keV band. They are attributed as a 'hot spot' on the accretion disk.

INTRODUCTION

Active Galactic Nuclei (AGN) are among the most energetic and luminous objects in the universe. They are a key to understanding galactic evolution. Seen in every band of the electro-magnetic spectrum, each new advance in telescope technology further increases our ability to study these objects. The past decade has brought a huge increase in the ability to study the X-Ray sources with observatories such as Chandra X-Ray Observatory, Rossi X-Ray Time Explorer, Suzaku, and XMM-Newton.

Since the launch of XMM-Newton, the ability to study the phenomenon of AGN has increased dramatically. With its large effective area and long elliptical orbits, XMM Newton has the ability to observe objects in the X-Ray band like few other observatories. For the first time it is now possible to study objects with short-term and long-term variability using a dynamical spectral analysis method. In this work the method of dynamical spectral analysis is applied to several promising sources: NGC 4051, IRAS F12397+3333 and Markarian 766.

The method of dynamical spectral analysis takes the spectrum of an object and divides it into groups of like behavior. Typically in other methods when the spectrum is split into different regions it is done rather blindly. Data is cut into even sized time regions or by flux level regardless of what is actually occurring. Rather than blindly slicing a data set into arbitrary and uniform chunks, in the dynamical spectral method like data are kept together. Rising and falling portions can be grouped together, flares

and non-flares, and other periods of interest. In this work flares and non-flares are generally grouped together. If, however, a period of interest should occur, they were grouped separately.

The goal in taking the time to look at the data in this way is to gain an understanding of the objects' variability, taking into account the multitude of factors that can cause such variability. As it includes both temporal as well as spectral variability, a more complete picture is formed.

Dynamical spectral analysis has been used with previous X-Ray observatories, but with limited success. This is due to the fact that the observatory either lacked a large enough effective area to make splitting the data set statistically viable or could not observe the target long enough to generate a data set that could be split. As a result, this method has seen limited use in the study of AGN. However with accumulation of multiple long observations of highly variable AGN with XMM-Newton the situation has now changed. It is now possible to perform this type of analysis. As such the dynamical method is used throughout this work yielding several key findings. Amongst these include regions of minimal spectral activity, inhomogeneous absorption regions and flares generated by accretion disk hot spots.

The structure of this work is as follows:

Chapter 2 provides a background on the field of AGN. Their various subtypes and a brief history of their discovery and understanding are given. Then a general overview of the broadband spectral features is given. This covers radio through gamma ray,

with special emphasis given to X-Rays as the primary focus of this work. This is followed by a brief description of the basic physics of accretion powered AGN and the current unified model of how the various subtypes are related.

Chapter 3 provides a basic overview of XMM-Newton, the X-Ray observatory used in this work. Descriptions of the spacecraft, X-Ray telescopes and instruments are given. A brief introduction is given to the software used with this work. Then the data reduction method is provided.

Chapter 4 covers NGC 4051. This Narrow Line Seyfert 1 galaxy is known for its large violently variable changes, periods of limited activity and prominent Fe Kα line. Here the primary focus has been in understanding a period of low activity in relation to its flaring events by extending some early work. Previously, a cloud that partially covers the primary source has been proposed to explain the variability of NGC 4051. This model was explored in relationship to the low activity seen and a particularly interesting region of extremely low activity. This region has not previously been understood.

Chapter 5 looks at IRAS F12397+3333. This is a little studied Narrow Line Seyfert 1 that exhibits interesting behavior in its absorption features. A high degree of optical polarization and reddening cause this object to exhibit absorption features that have recently become of interest. IRAS F12397+3333 shares a number of features with IRAS 13349+2438, a galaxy that has revolutionized the way the phenomenon of the 'warm absorber' is viewed and understood.

Chapter 6 investigates Markarian 766. This is another Narrow Line Seyfert 1 galaxy known for its high variability and broad Fe Kα line. In this instance the variability is quite rapid, in timescale less than an hour. But it also exhibits long-term variability. The source exhibits some unusual spectral behavior at low flux as well as peculiar high flux behavior. During a period of low flux Mrk 766 takes on temporal and spectral behavior unlike its average behavior, before changing back to the average in a short period of time. During the high flux state three flares were discovered that appear to represent a different physical emission mechanism, as they appear to be spectrally independent of the main continuum. Neither of these phenomena have been previously identified.

Chapter 7 provides some concluding remarks on each of these sources. Possible direction for future work on these sources and others are also addressed.

Appendix A covers basic spectral models used in this work. A brief description of each model is given, a description of the model parameters and references are also given when necessary.

Appendixes B, C and D provide additional tables associated with the spectral fitting of NGC 4051 and Markarian 766 that were too long to fit into the main text.

OVERVIEW OF ACTIVE GALACTIC NUCLEI

2.1. Introduction

In the broadest sense, galaxies can be divided into two groups: normal and active. In active galaxies a very large fraction of the energy radiated by the galaxy comes from the nucleus, hence the name Active Galactic Nuclei (AGN). The nuclei of these galaxies can outshine the host galaxy in many cases. All radiate energy from the infrared to X-Ray and can have strong Radio and gamma ray emissions. Most are strong X-Ray sources.

AGN are classified into several subgroups. Four types of AGN will be discussed here: Seyferts, Quasars, Radio Galaxies and Blazers/BL Lacs.

2.1.1. Seyferts

The first type of AGN to be identified was the Seyfert type. These galaxies were named after Carl Seyfert, who in the early 1940's began to group galaxies together based on their morphological characteristics (Seyfert, 1943). Historically the first observations of AGN were made by E.A. Fath in 1908 at the Lick Observatory. Fath was able to get a spectrum from NGC 1068. This "spiral nebula" was notable because it showed several prominent emission lines normally seen in gaseous nebulae (Fath, 1909). In 1917, Vesto M. Slipher, also at the Lick Observatory, was able to produce a much higher quality spectrum for NGC 1068 and saw more emission lines (Slipher, 1917).

Carl Seyfert studied a group of six galaxies: NGC 1068, NGC 1275, NGC 3516, NGC 4051, NGC 4151, and NGC 7469. He realized these galaxies formed a distinct class based on shared morphological characteristics. The characteristics that Seyfert identified are spiral galaxies with a very bright central core that is stellar in appearance and with emission lines from highly ionized atoms. The optical spectra were dominated by the emission lines and were notable as being quite broad. Seyfert galaxies were generally ignored until 1955, when NGC 1068 and NGC 1275 were identified as radio sources.

From studies of these emission lines in Seyfert galaxies, Khachikian & Weedman (1974) recognized that Seyferts fell into two subgroups: Seyfert Type 1 and Seyfert Type 2. Two types of emission lines were identified. 'Narrow lines' show the characteristics of arising from low density ionized gas with line widths of a couple hundred km sec^{-1}. 'Broad lines', on the other hand, arise from high density ionized gas with line widths as high as 10^4 km sec^{-1}. Seyfert 1 galaxies show both broad and narrow lines. Seyfert 2's have only narrow lines.

Realizing that Seyferts form a continuum of objects rather two fixed groups, Osterbrock (1981) introduced the notation of Seyfert 1.5, 1.8 and 1.9 for the intermediate groups. The higher number indicates progressively weaker broad lines. An important subgroup of the Seyfert 1 galaxies are the Narrow Line Seyfert 1 (NLS1). This group was identified by Osterbrock & Pogge (1985). They are characterized by the narrow Balmer emission lines, with 2000 km sec^{-1}, ratio of [O III] 5007 Å to Hβ of less than

3, and strong Fe II emissions. NLS1 show very large changes in variability. In the case of IRAS 13224-3809, an intensity increase of a factor of 10 has been observed occurring in a few hours (Boller et al., 1997).

2.1.2. Quasars

Beginning in the late 1950's, large radio sky surveys were conducted for the first time. Radio astronomy had reached the point where the resolution of the radio telescopes were of great enough resolution to identity radio objects with optical objects. Many of these radio sources could be tied to known optical galaxies. However, there were some radio sources for which the only optical counterpart that could be found was a star. These "stars" showed very unusual spectra with a multitude of unknown emission lines. They became known by the name quasi-stellar radio sources, QSRs, or more simply quasars.

The key to understanding these objects lay in identifying the emission lines. The breakthrough came from Maarten Schmidt and the quasar 3C 273. Schmidt (1963) realized that the lines he was seeing in 3C 273 were the Balmer series of hydrogen, only red-shifted. The red-shift Schmidt needed was z = 0.158, one of the largest known at that time. More disturbing than the large red-shift was the colossal luminosity implied. 3C 273 remains the brightest quasar known in terms of apparent magnitude. With the understanding that these objects reside at large red-shifts, the lines of other quasars were soon identified (Greenstein & Matthews, 1963).

Schmidt had soon studied enough of these objects to identify the shared characteristics of them. What Schmidt identified as common to quasars are: all these radio sources have star-like optical counterparts, they have a large red-shift, broad emission lines, large UV fluxes and time-variable continua (Schmidt, 1969). An important feature that would be added to the list later with the maturity of X-Ray astronomy is that all are strong X-Ray sources (Elvis et al., 1978).

Searching the radio catalogs to find quasars was a slow process. A better method was to search for stars that had an U-excess to generate a list of candidates (Ryle & Sandage, 1964). This list of candidates could then have their spectrum taken and a radio counterpart searched for. However, this search method yielded a very interesting result. Roughly 90% of the objects found this way were radio-quiet objects. Only about 10% were radio-loud. To distinguish these objects from QSRs, they were called quasi-stellar objects (QSOs). The term quasar is now used interchangeable between the two.

Quasar's spectra show several similarities to that of Seyferts 1. Both show broad and narrow lines but the narrow lines are weaker in quasars. Stellar absorption features are also much weaker in quasars. Whereas Seyferts clearly show the host galaxy, quasars have what is called 'quasar fuzz.' This is a halo of low surface brightness material that is attributed to starlight from the host galaxy. Recent observations with the Hubble Space Telescope and ground-based observatories with advanced optics

have revealed the host galaxy of the quasars for the first time, see Aretxaga et al. (1998); Lehnert et al. (1999); McLeod & McLeod (2001).

2.1.3. Radio Galaxies

In addition to finding quasi-stellar radio sources, the radio surveys of the 1950's also discovered strong radio sources that were clearly identifiable with a host galaxy. These sources have been dubbed radio galaxies. Morphologically radio galaxies come in two varieties: lobe dominated and core dominated. Lobe dominated radio galaxies have large lobes that extend from the host galaxy and are responsible for the majority of the radio emission. In core dominated radio galaxies the radio emission comes from an compact area that is unresolved at 1" scales. Radio galaxies are found to be almost exclusively giant elliptical galaxies (Adams, 1977).

Lobe dominated radio galaxies have major morphological features in large lobes or jets that extend from the galaxy. The radio spectra are quite steep in these sources. Often the lobes are found to be in pairs and are approximately symmetric. The lobes are large, extended radio sources. The typical size is a few hundred kiloparsecs, but can be a megaparsec or bigger. Due to their size they are optically thin and the emission mechanism is synchrotron radiation. Radio lobes can be classified as two types based on the work of Fanaroff & Riley (1974) (FR). Class 1 (FR 1) are weaker sources with a bright center that falls off towards the edges. Class 2 (FR 2) are stronger sources that are limb-brightened and show regions of embedded structure or enhanced emission. It should be noted that Seyferts lack radio lobes.

Radio galaxies have some basic similarities to Seyferts in that they show Type 1 and Type 2 optical spectral features, as described in Section 2.1.1. Broad Line Radio Galaxies (BLRG) have a Type 1 optical spectrum showing both broad and narrow lines. Narrow Line Radio Galaxies (NLRG) have only narrow lines like a Type 2 optical spectrum. These are considered to be the radio loud version of Seyfert galaxies.

Core dominated radio galaxies produce most of their radio emissions in a compact area equal to or less than 1". The radio spectrum for these sources is much flatter and extends over a farther range than lobe dominated radio galaxies (Tornikoski et al., 1993). The variability of the core dominated is also much greater than the lobe dominated. Jets are commonly found in these sources. Core dominated radio galaxies are closely related to blazars.

2.1.4. Blazars

A small subgroup of the AGN are known as blazars. The phrase was coined by E. Spiegel during a talk in 1978. It is a grouping of two similar types of objects, BL Lacertae objects and Optically Violently Variable quasars. Both are loud radio sources, highly variable, and notable for their smooth continua. Blazars represent less than 1% of all AGN.

BL Lacertae (BL Lac) was thought for more than 20 years to be a variable star. It was known for its short term, large magnitude changes. Its light was also highly polarized. The spectrum, however, was unlike that of most stars. The continuum

was nearly featureless with only weak absorption. In 1968, the connection between a strong radio source and BL Lac was made by Schmitt (1968). BL Lac became the prototype object for a class of objects called BL Lacertae Objects or simply BL Lacs in 1972 (Epstein et al., 1972). Then in 1974, it was shown that BL Lac itself was not a star but an AGN when it was shown be to be at cosmological distance (Oke & Gunn, 1974).

A similar class of objects to the BL Lacs are the Optically Violently Variable (OVV) quasars. These are quasars that show very large, non-periodic changes in magnitude on a short time scale. A typical change in magnitude is 0.1 in one day. Such changes for an object as large as a galaxy are very unusual. The light is highly polarized and the polarization is also variable.

2.2. AGN Central Engine

Observations of Seyfert galaxies, radio galaxies and more recently of quasars have shown that the very luminous emissions of AGN come from a very "small" area in the nucleus of the host galaxy. In order to produce such a bright source over such a large spectral range in such a small area, it takes a very unique power source. This power source is dubbed the central engine. Many theories have been put forward to explain the central engine, but nearly all have fallen away, being unsupported by observation, unable to explain certain phenomenon, or simply being unphysical in favor of the black hole paradigm. At its simplest, the black hole paradigm states that

AGN are powered by a black hole at the center of the galaxy. There are two non-contradictory ways in which the black hole can power an AGN; accretion powered or rotation powered.

In an accretion powered AGN, accreted matter releases energy as it falls in to the black hole. The basic structure of the system is: A black hole forms the very center of the system. An accretion disk extends out from very near the black hole, which can extend to hundreds of gravitational radii. Surrounding the disk and black hole are regions with ionized clouds of gas called the Broad Line Regions. A dust torus rings the system. And finally there are more ionized gas clouds in Narrow Line Regions farther away. Seyferts, BLRG, NLRG and quasars are accretion powered.

AGN can also be rotation powered. If the black hole is rotating in a magnetic field a simple dymo action is created. By a simple application of Faraday's law, Blandford & Znajek (1977) showed how power could be extracted from a rotating black hole. Material from the accretion disk or ergosphere of a rotating black hole flows along the magnetic field lines. Material ejected from the system forms the jets. The magnetic field, via a mechanism not well understood, collimates the material in the large jets, such as those seen in lobe dominated radio galaxies. Radio galaxies, blazars and QSRs are predominantly rotation powered.

2.3. General Spectral Features

Before discussing how all of these phenomena are related to each other, the general spectral features will be discussed more in-depth. This will finish laying the groundwork for that discussion. The discussion will start with the low energy continuum emissions and move to the higher energies, ending with gamma rays. This discussion is meant to talk about predominately the spectra of Seyfert and QSO AGN. Blazar spectra are significantly different from other types of AGN that they would warrant a separate section to discuss their spectra and that is beyond the scope of this work.

2.3.1. Radio

Radio sources in AGN come in two major types: compact and extended. Compact radio sources are sources that are unresolved at resolutions of 1" and optically thick, whereas extended sources are resolved at this same resolution and optically thin . Extended sources are the radio lobes or jets of Radio galaxies and QSR's. Compact sources are associated with the optical nucleus of the AGN. Both are generated by synchrotron emission (Alfvén & Herlofson, 1950; Shklovskii, 1953).

Although both may be generated from the same non-thermal emission mechanism, they have different types of spectra. Extended sources have steep power law spectra with energy indexes typically between 1 and 2. In contrast, compact sources are flat. They have a typical energy index of 0 and can fit over a wide range of frequencies. The low frequency radio cut-off occurs due to synchrotron self absorption.

2.3.2. Infrared

The infrared (IR) continuum is believed to be thermal and connected to dust in the torus that surrounds the nucleus (Rees et al., 1969; Rieke, 1978; Lebofsky & Rieke, 1980). The most prominent feature of AGN in the IR is a local minimum located at 1 µm and a smooth bump at longer wavelengths known as the 'IR bump' (Sanders et al., 1989). Dust in the torus is heated by the central source and is re-radiated as the warm thermal component forming the IR bump. The 1 µm minimum is a local minimum between hot thermal emission of UV/optical source and warm thermal of the IR bump. A sub-millimeter break in radio quiet AGN causes the spectrum to drop off quickly toward the radio and is consistent with thermal spectral cut-off due to dust grains (Draine & Lee, 1984).

The IR continuum is also notable for its variability. It shows a similar type of variability to that of the UV/optical variability but with significant time delay (Clavel et al., 1989). The interpretation of this delay is from the light travel time. The UV/optical source is the central accretion disk, and it is separated from the dust torus by a few parsecs.

2.3.3. Optical

The optical continuum is thought to originate more from the accretion disk and is hence thermal in nature. As follows from the discussion on the accretion disk, the disk is seen basically as a series of blackbodies at increasingly large radial distances from the central engine, all superimposed on one another. So instead of seeing a

single blackbody spectrum, like a star, what is seen is a series of blackbodies, giving the appearance of a power law.

Most AGN's optical spectra are dominated by their emission lines. As was stated earlier these emission lines come in two types: broad lines and narrow lines. Broad lines are seen as a broad wing superimposed on a narrow core. The Balmer series is a highly important series used to identify red-shift in both Type 1 and Type 2 spectra. Some of the largest velocity widths of the broad lines are normally seen in the Balmer series.

Other important emission lines in the optical include [O III] 5007 Å, 4959 Å and 4363 Å, He II 4686 Å, He I 5876 Å, [N II] 6548 Å, [S II] 6716 Å and Fe II. He II 4686 Å and He I 5876 Å are frequently observed to have wider line width than the Balmer series. [N II] 6548 Å, [S II] 6716 Å and the [O III] lines are normally seen as narrow lines with width around 350 to 400 km sec^{-1}.

The emission lines come from two distinct regions: the Broad Line Regions (BLR) and the Narrow Line Regions (NLR). The need for two distinct regions arise from the fact the lines have two sets of line widths and that Type 2 have only Narrow Lines. Both regions consist of groups of clouds formed by photo-ionized gas. As the broadening of the lines is due to orbital motion of these clouds, the NLR must be farther away from the central engine than the BLR. The NLR exists outside the dusty torus, whereas the BLR is inside the torus. See Osterbrock & Ferland (2006) for a detailed description and discussion of the physics of each of these regions.

As with most spectral bands, the optical continuum varies. And as with other spectral bands the variability is non-periodic. In large scale variability, the optical variability is tied to that of the UV, as both vary nearly in phase with one another. For small scale variability of time scales less than a day, the optical is smoother than the UV. Finally, as the source brightens, the spectra became harder.

2.3.4. Ultraviolet

Like the optical, the ultraviolet continuum is mostly a series of blackbodies that are seen as a power law. But UV has one very dominant feature that is not tied to the emission lines. That is the "big blue bump." The ultraviolet continuum unfortunately has a gap in it where observations are essentially impossible due to the absorption by the neutral hydrogen of our own galaxy. This gap in the extreme ultraviolet (EUV) extends from 912 Å to 100 Å. More unfortunate, there are two features in this band that would be of great interest if they could be observed. First are the neutral hydrogen lines. The second is the big blue bump. A majority of the big blue bump can not be observed. What is known about it is inferred from its observable wings. Because the entire big blue bump can not be directly observed, the physics governing it can be difficult to understand. It is thought to be thermal in nature and is the dominant continuum feature in the whole UV band. This thermal nature tends to lead it to be linked to the accretion disk.

Like the optical band, the near and far UV show a large number of emission lines, both broad and narrow. The most prominent lines in a typical Seyfert are: [Ne III]

3869 Å, [O II] 3727 Å, [Ne V] 3426 Å, Mg II 2798 Å, C III] 1909 Å, C IV 1549 Å, H Ly α 1216 Å and H Ly β 1026 Å.

The UV variability is similar to that of the optical. No periodicity is seen, the spectra hardens as the source brightens and large scale variability of the two are tied to one another. However, on time scales of less than a day, variations are seen in the UV that are not tied to the optical. The cause of this is believed to be from the fact the the UV is likely generated closer to the central engine than the optical.

2.3.5. X-Ray

Most AGN are strong X-Ray sources. Generated in the region closest to the central engine, this proximity makes them an excellent tool for studying this central engine. Because this work will primarily be focused on X-Ray emissions, more time will be spent and greater detail used to describe the spectra, particularly those of the Seyfert 1.

Above 2.0 keV the X-Ray spectrum of a typical AGN is roughly fit by a power law. Between 2 and 10 keV the power law fits the spectra quite well. In radio quiet sources there is a high energy cut-off energy of 100 to 200 keV by thermal electrons (Zdziarski et al., 1995). Seyfert 1s have a flatter spectra than Seyfert 2s. And BLS1 have a flatter photon index, Γ, about 1.9, than NLS1, with Γ about 2.2. Nandra & Pounds (1994) demonstrated that a single power law is not an accurate description of the spectrum at higher energies. For energies higher than 10 keV there is usually a reprocessed component that must be taken into account to model the spectrum well.

The actual emission mechanism that gives rise to the power law is inverse Compton scattering. Soft seed photons from the disk scatter off hot electrons in a coronal region above the disk, see Haardt & Maraschi (1991) and Haardt et al. (1994). As the soft seed photons pass through the corona they scatter to higher energies. The energy source for the hot electrons has been elusive. The high energy cutoff of the power law model is tied to the energy of the thermal electrons and is known to be in the range of 100-200 keV (Zdziarski et al., 1995). That implies that the hot electrons are four orders of magnitude higher in temperature than the disk. Common mechanisms for heating the corona are magnetic reconnection and magnetohydrodynamic shocks. As the source of the seed photons is unobservable due to absorption by neutral hydrogen and high energy cutoff, which is in the 100-200 keV range and is difficult to observe, this continuum feature is described as a power law.

In the band from 2.0-10.0 keV the prominent emission feature is the 6.4 keV Fe Kα fluorescent line. The line can be very broad, particularly in the case of MGC-6-30-15 (Tanaka et al., 1995; Iwasawa et al., 1996b,a). A typical equivalent width for the Fe line is between 5 to 300 keV (Mushotzky et al., 1993). This is a very important feature because of how it is generated and its relationship to the central engine. It is generated according to the disk-corona model by hard coronal X-rays hitting the cool iron in the accretion disk, causing them to fluoresce.

The presence of the reprocessed component, in the form of the Fe line, indicates there is also a Compton reflection component. In the band above 2.0 keV the continuum photons are either Compton scattered off a cool, optically thick slab, or are absorbed by it (Guilbert & Rees, 1988; Lightman & White, 1988). Over short time scales this component is stable due to the fact that it averages itself out with the light-travel time involved. On longer time scales minor variations are seen.

Some models also require an additional component to explain the high energy tail. One such model is a partially covering cloud. This is a cloud of gas and dust that absorbs X-rays. It lies between the source of the X-rays and the observer. The cloud is large enough to cover part of the source but does not completely block the source from the observer. Such partial covering models have been used to successfully model several AGN, see Kunieda et al. 1992; Boller et al. 2002, 2003; Haba et al. 2003; Gallo et al. 2004; Haba et al. 2008.

Extending the power law model into the band below 2.0 keV can lead to what is called the "soft excess". A common feature of NLS1, soft excess is seen more often and at greater levels in NLS1 than in other types of AGN (Nandra et al., 1997a). Seen in energies less than 2 keV, the nature of this excess is not completely clear. Some believe it is the high energy end of the big blue bump and therefore is thermal in nature (Ross et al., 1992; Kawaguchi, 2003; Ohsuga et al., 2003). Another possible explanation is that thermal bremsstrahlung is the cause of the big blue bump and

hence the soft excess (Barvainis, 1993). There are non-thermal interpretations of the soft excess.

One non-thermal interpretation that has become very important in recent years is the blurred ionized relativistic reflection model (Ross & Fabian, 1993; Ross et al., 1999; Ross & Fabian, 2005). In this model an X-Ray source at some height above the disk illuminates the disk. This illumination photoionizes the material of the disk and produces emission lines. As this occurs close to the central black hole, rather than producing narrow, clearly defined lines, these are distorted and smeared together because of the strong general relativistic effects. The soft X-Ray band is where H and He like C,N,O and Ne and M shell Fe all produce lines within a few 100 eV of each other and easily blend into one another, even for moderate blurring, forming the correct shape for the soft excess. With a super solar abundance of Fe, the relativistically broadened Fe Kα line can be accounted for. And at higher energies, the hard X-Ray hump can also be accounted for.

Miniutti & Fabian (2004) showed that as the height of the illuminating source changes there are three regions based on the relationship the flux of the illuminating source and ionized reflection have. When the height of the illuminating source is small, the source is very close to the central black hole. As such much of the light is lost to the black hole, as is the reprocessed light of the ionized reflection. In this case there is a direct correlation between the two fluxes. As the height of the illuminating source increases it moves away from the black hole and fewer of the photons are lost

to it. But the ionized reflection's location relative to the black hole does not change. Therefore the flux of the ionized reflection appears to be constant, while the flux of the illuminating source appears to be independently increasing. If the height of the illuminating source continues to increase it reaches the point where it no longer illuminates the disk efficiently, resulting in a decrease in the ionized reflection flux. In this regime the two fluxes appear anti-correlated. The illuminating source is assumed to be the corona, hence the power law component. See Miniutti & Fabian (2004) for further details.

In addition to the soft excess, the soft X-Ray band is also host to a large number of emission and absorption lines. An important source of absorption lines is the "warm absorber," proposed originally to explain an unusual spectral feature seen in some quasars (Halpern, 1984). But shortly thereafter the same feature was seen in Seyferts (Ulrich, 1988). The warm absorber is now widely recognized as an important feature in many Seyfert galaxies (Nandra & Pounds, 1994; Reynolds, 1997). The warm absorber is characterized by the presence of O VII and O VIII absorption edges at 0.74 keV and 0.87 keV. Based on modeling of these sources it is believed that they originate from the BLR (Mathur et al., 1995).

However, newer observatories with higher resolution spectroscopes have revealed that there is a whole host of elements that make up the warm absorber. Also many of these sources, IRAS 13349+2438 (Sako et al., 2001), Mrk 766 (Sako et al., 2003 and Mason et al., 2003), NGC 4051 (Pounds et al., 2004), MGC -6-30-15 (Lee et al., 2001)

and NGC 3783 (Kaspi et al., 2002 and Netzer et al., 2003) lack the absorption edges that were characteristic of a warm absorber. Instead there is a large trench in these sources between 15 to 17 Å. Behar et al. (2001) showed that based on predictions from the photoionization code XSTAR (Kallman, 2010), Fe L shell should form such a trench, which they call an Unresolved Transition Array (UTA). These ionization phases of Fe happen to form absorption lines in this region very close to one another. And given the current limit of spectral resolution in the current observatories, these lines blend into one feature.

In addition to being a strong X-Ray source, AGN are also strongly variable in the X-rays (reviewed by McHardy, 1988). On time scales of days or longer, X-Ray variability appears synchronous with the UV/optical variability. However, variability on the orders of hours is frequently seen. NLS1 are a particularly variable source, exhibiting some of the largest non-blazar variability recorded (Boller et al., 1997). Unlike the UV/optical, the X-Ray's photon index steepens when the spectra becomes brighter.

2.3.6. Gamma rays

The gamma ray continuum of AGN shows a power law similar to that seen in X-Ray, but with a photon index that is steeper. This power law cut off comes somewhere in the 100 keV to 200 keV range. Much beyond a couple hundred keV most accretion powered AGN become lost in the gamma ray background and can no longer be observed.

2.4. Accretion Powered AGN

A full theoretical discussion of the accretion disk is beyond the scope of this work. A brief overview of the basic physics involved is within the scope. To begin with, it is assumed that accretion powered AGN, such as Seyferts and quasars, are powered by material falling into the black hole. The rate of gravitational potential energy released is given by $GM\dot{M}/r$ where M is the mass of the black hole, $\dot{M}$ is the mass accretion rate, G is the gravitational constant and r is the radial distance from the black hole. From the virial theorem half of this energy is radiated away and half is used to heat the gas. The energy radiated away must be equal to the energy radiated by a disk of temperature T and radius r

$$\frac{GM\dot{M}}{2r} = 2\pi r^2 \sigma T^4 \tag{2.1}$$

Or by solving for T,

$$T = \left(\frac{GM\dot{M}}{4\pi\sigma r^3}\right)^{1/4} \tag{2.2}$$

Equation 2.2 says that the temperature is greatest when r is smallest. But several factors have been left out. The most important is viscosity. Shakura & Sunyaev (1973) show that a more accurate derivation of the disk's temperature yields

$$T_{eff}(r) = \left(\frac{3GM\dot{M}}{8\pi\sigma r^3}\left(1 - \sqrt{\frac{R_{in}}{r}}\right)\right)^{1/4} \tag{2.3}$$

Where T_{eff} is the effective temperature and R_{in} is the inner boundary radius of the disk. If it is assumed that r >> R_{in}, Equation 2.3 can be rewritten as Equation 2.4 by expressing r in terms of the Schwarzschild radius,

$$T_{eff}(r) = \left(\frac{3GM\dot{M}}{8\pi\sigma R_s^3}\right)^{1/4} \left(\frac{r}{R_s}\right)^{-3/4} \tag{2.4}$$

Or

$$T_{eff}(r) = \left(\frac{3c^6 M^2 \dot{M}}{64\pi\sigma G^2}\right)^{1/4} \left(\frac{r}{R_s}\right)^{-3/4} \tag{2.5}$$

As this is assumed to be a blackbody, the Planck function for the spectral radiance, B_ν is .

$$B_\nu(r) = \frac{2h}{c} \frac{\nu^3}{exp\left(\frac{h\nu}{kT_{eff}(r)}\right) - 1} \tag{2.6}$$

Note that because the temperature depends on the radius, there is a different temperature for each radius. This result is called the multicolor disk model. Using Wien's law with a mass and mass accretion rate, a maximum frequency can be found. If a mass and Eddington accretion rate are used for a quasar, M=10^8 $M_\odot$ and $\dot{M} = 2$ $M_\odot$ per year and by assuming an inner-most radius of 6 R_S, a frequency of about 10^{16} Hz or 300 Å is found. This is peaked in the soft X-Ray or extreme UV.

2.5. Unified Model of AGN

How the various manifestations of AGN are related to each other is of fundamental physical importance. The understanding of how different AGN are related to each other is useful in better understanding individual AGN. The simplest place to start building a unified model for AGN is by connecting Seyferts and quasars. When first discovered, the two phenomena were thought to be quite different. As is often the case, the first objects discovered of a new class represent the extremes rather than the norm (Weedman, 1976). With the discovery of more of these object classes, more data has been gathered. It is now known that quasars and Seyferts share many of the same features and can sometimes be difficult to tell apart. The major difference between them is their luminosities: quasars are generally a couple of orders brighter than Seyferts. In the accretion powered AGN models the simplest way to create brighter objects is to have a higher accretion rate and larger mass. Therefore Seyferts are just "mini-quasars;" galaxies with smaller central engine masses and lower accretion rates.

As noted earlier, the difference between Type 1 and 2 Seyferts and core dominated Radio galaxies is the types of emission lines seen. Seyfert 1s have broad optical lines and Seyfert 2s do not. It is also worth noting that Seyfert 2s are slightly dimmer and greater in number than Seyfert 1s. Galaxies can be observed at any angle relative to the observer. Based on these criteria it is assumed that Seyferts Type 1 and 2 are really the same phenomenon, but viewed from different angles (Osterbrock, 1978). In order to prevent light from the BLR being seen, a dusty torus of material

that surrounds the central engine and BLR is assumed. This dust causes an optical attenuation of source and heavy reddening. Additionally, a scattering medium, which is above the black hole in the torus, is also needed. This scattering medium scatters and polarizes light from the central engine and BLR. The result is that when an observer looks through the torus they see a Seyfert 2 galaxy and when they do not, they see a Seyfert 1 (Osterbrock, 1978).

The idea is that all Seyfert 2s are really Seyfert 1s, but with hidden BLR. This view is supported by some observations, but it may ultimately be too simple to explain all Seyfert 2s. Observations of the Seyfert 2, NGC 1068, have led to detections of highly polarized broad line emissions (Antonucci & Miller, 1985). Other Seyfert 2s have also been found to have these polarized broad line emissions (Miller & Goodrich 1990 and Tran et al., 1992). These results would seem to support the theory that all Seyfert 2 have this dusty torus with a scattering medium. However, there is a growing body of evidence that this simple theory fails to explain. Many Seyfert 2s show more far infrared emission, UV reddening due to dust and molecular gas than can be explained with a dusty torus (Dahari & De Robertis, 1988b and Heckman et al., 1989).

Extending the idea that differences between Type 1 and Type 2 spectra are caused by different viewing angles can also be used to explain blazars. As was mentioned earlier, blazars are radio loud objects, highly variable and account for a small number of AGN. Based on the low population number it is assumed that there must be a

very small viewing angle in order to see blazar activity. Taking this small viewing angle and the variability of blazars into account, it is theorized that blazars are radio galaxies or QSR's that are viewed with the radio jet aligned or nearly aligned with the observer (Blandford & Rees, 1978).

The connection between radio loud and radio quiet AGN has been one of the more difficult problems to answer and is still an area of active research. In the work of Wilson & Colbert (1995), the case is considered where properties of the central engine can account for whether a source is radio loud or quiet. They focus on spin rate of the black hole. Their model is based on the merging of galaxies and their central black holes. The black hole spin rates are determined by the black hole's mass, not the accretion rate. The merger of two high mass black holes, 10^8 solar mass, yields a radio loud AGN. But the merger of a high mass and low mass black hole, 10^5 solar mass, or two low mass black holes yields a radio quiet AGN. Recent observations with the Hubble Space Telescope seem to lend credence to this theory. Observations of the Radio galaxies Cygnus A (Block & Sauvage, 2000; Canalizo et al., 2003) and NGC 6240 (Rafanelli et al., 1997) show evidence of two AGN merging.

Lobe dominated Radio Galaxies are viewed as 'dead' quasars. These are quasars that have slowed down or stopped their accretion due to the fact that they are emptying out the region of space they feed from. Without accreting matter to power these sources they become rotation powered. By extracting energy from the black

hole's rotation through the magnetic fields, the large jets and lobes are created and maintained (Blandford & Znajek, 1977).

XMM-NEWTON

The data presented in this work were gathered by X-Ray Multi Mirror Mission (XMM) Newton. The following is an overview of the observatory, its instruments, data products and how they were reduced.

3.1. Space craft

XMM-Newton is the European Space Agency's (ESA) current generation of X-Ray observatory. It is named in honor of Sir Isaac Newton for his contributions to the fields of mathematics and physics. Launched on December 10, 1999, XMM-Newton is the largest scientific satellite the ESA has launched to date.

The spacecraft is built such that it has two payload modules connected by a 10 m carbon fiber tube. The Service Module houses the X-Ray Mirror Modules, Optical Monitor, star trackers and most spacecraft subsystems. At the other end of the tube is the Focal Plane Assembly, see Figure 1. The observatory weights four metric tons (Jansen et al., 2001).

The orbit of XMM-Newton is a highly elliptical 48 hour orbit. This allows for long uninterrupted observations. Apogee is at 114,000 km and perigee is at 7,000 km. The inclination angle is approximately 40°. The orbit was chosen to allow the X-Ray instruments to operate at a temperature range of -85 ^{o}C to -100 ^{o}C without active cryogenic cooling (Jansen et al., 2001). Because the orbit of XMM-Newton

takes it through the Van Allen radiation belts, the observatory is limited to operating at altitudes of 60,000 km or greater.

Ground stations employed for XMM-Newton are in Perth, Australia and Kourou, French Guiana as the primary, with Villafranca, Spain and Santiago, Chile as secondaries. Mission Operations Centre (MOC) is at Darmstadt, Germany and Science Operations Centre (SOC) is at Villafranca. Data, which includes the science data, housekeeping files and telemetry, are downloaded from XMM-Newton at a maximum rate of 64 kbit/sec to the ground stations. From the ground stations the data is then transmitted to both MOC and SOC. MOC monitors the spacecraft for health of scientific instruments and provides commands of scientific operation. The SOC preprocesses the raw data into data files for the science community, Observation Data Files (ODF) (Jansen et al., 2001).

3.2. XRT

XMM-Newton is composed of three X-Ray telescopes (XRT). The XRT are a set of 58 nested Wolter-type 1 X-Ray mirrors (Aschenbach et al., 1987). The grazing incidence angles for the mirrors are 17 to 24 arcmin. The mirrors themselves are nickel coated with gold as a reflective material. The focal length is 7.5 m. All three XRT are aligned (Jansen et al., 2001). At the focus of each of the XRT is one of the three European Photon Imaging Cameras (EPIC). To prevent electrons focused by

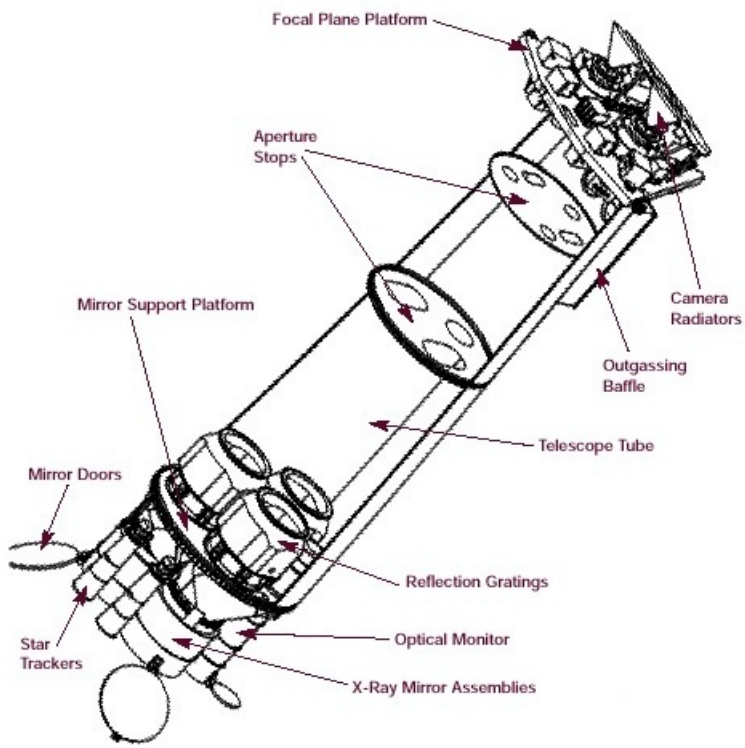

Figure 1: XMM-Newton spacecraft cut away. Shown the major spacecraft components including mirror assemblies, reflection gratings and instrument platform (Barré et al., 1999).

the mirror from reaching the detectors, a circumferential magnetic field is produced to act as an electron deflector, see Figure 2.

Although each of the XRT is essentially identical, there is a minor difference in them. Two of the XRT have grading placed in them. These gradings reduce the amount of light that reaches the instrument at its focus. About 44% of the incoming light reaches the instruments at the foci, 40% is diverted to the spectroscope and the rest is absorbed.

The configuration of XMM-Newton's XRTs allows for a very large effective area. For example, the effective areas of three different energies are: 1,600 cm^2 at 0.6 keV,

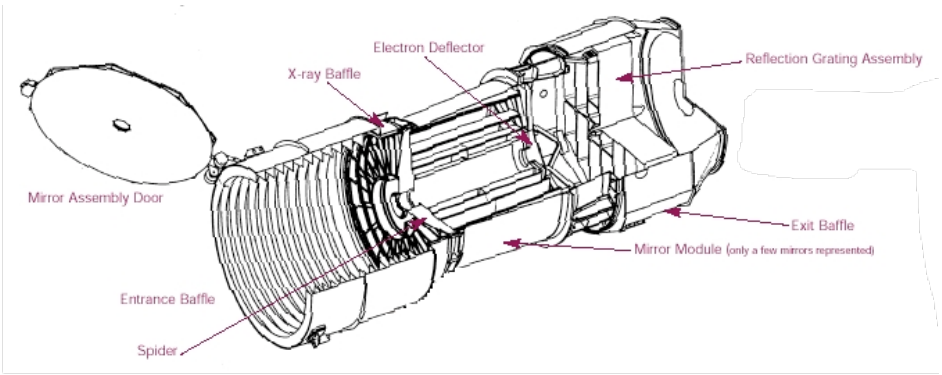

Figure 2: The X-Ray telescope mirror modules cut away. Illustration includes the mirror assembly and reflection gradings (de Chambure et al., 1999).

2,100 cm^2 at 1 keV and 950 cm2 at 8 keV (Jansen et al., 2001). To date this is the largest effective area for any X-Ray observatory. But this large effective area comes at the cost of angular resolution. The angular resolution is approximately 6" for full width at half maximum.

3.3. OM

A fourth optical telescope is included on XMM-Newton. It is a 30 cm optical / ultra-violet (UV) telescope called the Optical Monitor (OM). This is the first time such a feature has been included on an X-Ray observatory. Aligned with the three XRTs, OM allows for simultaneous observations in the X-Ray, UV and optical (Mason et al., 2001). It also aids in identifying X-Ray sources with their optical counterparts. No data from the OM will be used in this work and it is only mentioned here for completeness.

3.4. EPIC MOS

The two XRTs with the reflective gratings each have one of the Metal Oxide Semi-conductor (MOS) detectors as part of the EPIC camera. These are known as MOS 1 and MOS 2. Each is made of seven Charged Coupled Devices (CCDs). The chips are arranged in a circle pattern, with CCD 1 of both cameras at the center and the other six chips surrounding it, see Figure 3.

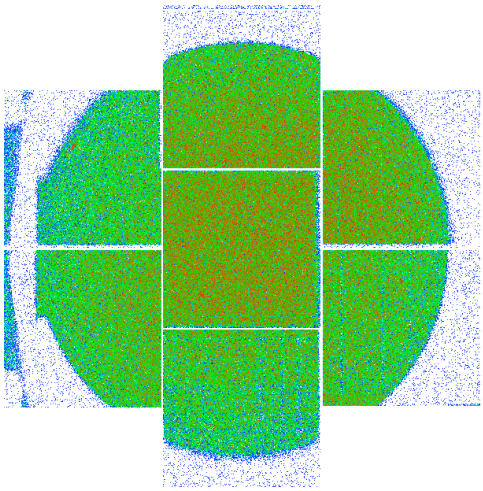

Figure 3: EPIC MOS CCD arrangement (Turner et al., 2001).

Each of the seven CCDs is a front illuminated chip with an imaging area approximately 2.5 cm by 2.5 cm. The CCDs have an imaging area of 600 by 600 pixels. To minimize chip gaps, the CCDs are overlapped. This results in a 300 micron gap between each chip. In order to have as complete coverage as possible, MOS 2 has been rotated 90° from MOS 1 (Turner et al., 2001). This means that all of the chip gaps, except for those around CCD 1, are covered by the other camera. The chip gaps around CCD 1 are covered by EPIC pn.

Each of the MOS cameras has a set of four filters that can be used during observations. There are two thin filters made from 1600 Å poly-imide film coated with 400 Å of aluminum. A medium filter is also made of 1600 Å poly-imide film but coated with 800 Å of aluminum. A thick filter is made from 3300 Å poly-imide film coated 1100 Å aluminum and 450 Å tin. In addition, there is an open position in the filter wheel and a closed position (Turner et al., 2001).

The MOS cameras have four operating modes: Full-frame mode, large window mode, small window mode and timing mode. These operating modes are used in conjunction with the filters to limit the effects of pile up. In full-frame mode the total area of the central chip is used, 600 x 600 pixels, and is read out every 2.6 sec. In large window mode only the 300 x 300 pixel region is used, but is read out in 0.9 sec. In small window mode a 100 x 100 pixel region is used and read off in 0.3 sec. For timing mode, used for high time resolution observations, a 100 x 1 image is recorded every 1.5 msec (Turner et al., 2001).

As of March 9th, 2005, CCD 6 of MOS 1 was damaged by what has been characterized as a micro-meteor event. The CCD exhibited a large spike in electric activity. The decision was made to turn off the CCD to prevent further damage to it and the adjacent CCDs. All observations made after March 9th, 2005 have CCD 6 of MOS 1 turned off (XMM web site). To date there is no further damage to MOS 1 and none to MOS 2 resulting in the loss of another CCD.

3.5. EPIC pn

The third XRT has the EPIC pn camera at its focus. EPIC pn is a different type of CCD detector and is radically different from EPIC MOS. It was developed by the Max-Planck-Institut für extraterrestrische Physik (MPE) specifically for XMM-Newton. The detector was designed to meet the performance requirements for XMM-Newton in terms of energy and angular resolutions, field of view and energy bandwidth. In

addition, it also was required to have low noise levels, an ultra-fast readout and has a high detection in the band above 2.0 keV (Strüder et al., 2001).

The pn camera is made of 12 back illuminated CCDs on a single silicon wafer. It is divided into four quadrants, each having three 200 x 64 pixel CCD subunits, see Figure 4a. The total imaging area is 6 x 6 cm^2. The pixel size on pn is 150 x 150 μm^2, representing 4.1 arcsec of sky. For the individual quadrants the chips are 194 μm. Between Quadrants 0 and 3 and Quadrants 1 and 2 the gap is 41 μm. Between Quadrants 0 and 1 and Quadrants 2 and 3 the gap is 214 μm (Strüder et al., 2001). EPIC pn is mounted such that it is rotated 45° with respect to EPIC MOS. The aim point is on CCD0 of Quadrant 1.

The pn camera operates in an energy range of 0.15 keV to 15 keV. Typically the expected energy range is 0.3 keV to 15 keV. Although current calculations of the system allow observations down to 0.2 keV, this is frequently not used. Low detection rates and poor statistics mean the usable upper energy limit is closer to 12 keV. The energy resolution is E/dE 20 to 50 over the detector's spectral range.

Like EPIC MOS, EPIC pn has a six position filter wheel. The first two positions are the open and closed windows. Like EPIC MOS there are two thin windows, a medium window and a thick window. However, the thicknesses of the filter windows are different. The thin windows have a 10.8 μm layer of aluminum and 22.4 μm of polyimide. The medium window has a thicker aluminum layer, 21.6 μm, but the same polyimide layer. The thick window has a 18 μm thick layer of tin and 27.5 μm layer of

polypropylene sandwiched between two layers of 28 μm of aluminum (Strüder et al., 2001).

EPIC pn has six operation modes: full frame, extended full frame, large window, small window, timing and burst mode. Figure 4b shows chip illuminations for all operation modes. In full frame and extended full frame all 12 chips are fully illuminated. The readout cycle is 74.3 msec for full frame and 199.2 msec for extended full frame. For the large window mode, only a 64 x 64 pixel region of the chip is illuminated, the rest is used for storage. Its readout cycle is 47.7 msec. A 64 x 64 pixel region of CCD0 from the first quadrant is used for small window mode. The readout cycle is 5.7 msec. Finally, in burst and timing mode only CCD0 from the first quadrant is used. They have time resolutions of 7 μsec and 30 μsec respectively (Strüder et al., 2001). Like EPIC MOS, these operation modes are used in combination with the filters to limit pile up.

As of this writing there is no damage to the pn camera.

3.6. RGS

For high resolution spectroscopy there is the Reflection Grating Spectrometer (RGS). Spectral resolution for RGS is E/dE 100 to 500 in a wavelength range of 5 to 38 Å. RGS consists of two parts: the Reflection Grating Assembly (RGA) and RGS Focal Camera (RFC). The two XRTs that are equipped with RGS units are the XRTs with the EPIC MOS detectors at its foci.

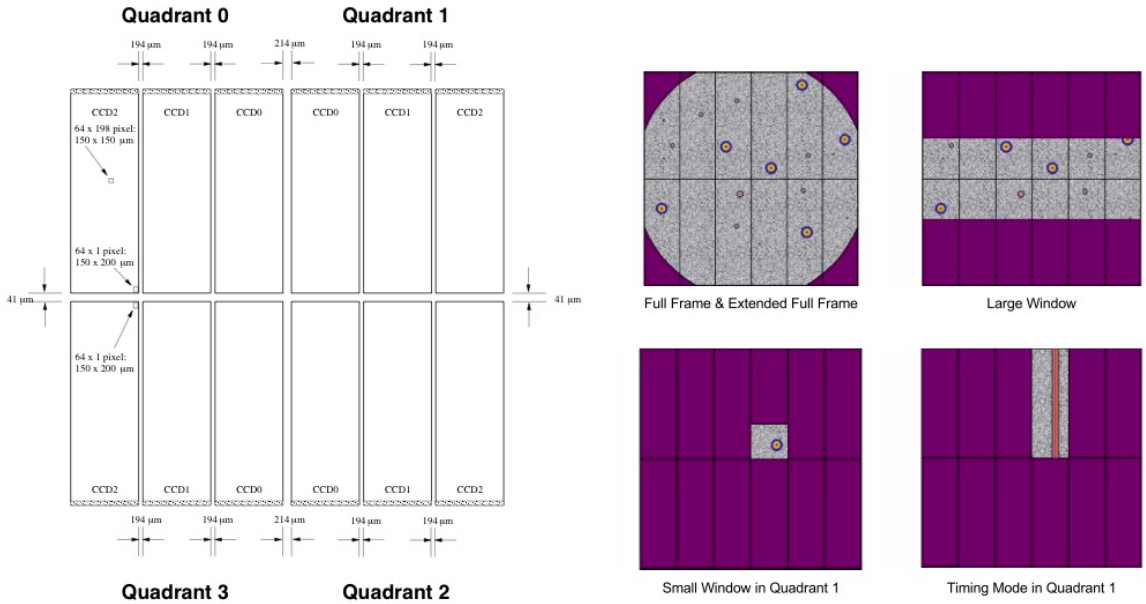

(a) (b)

Figure 4: Figure (a) shows the CCD geometry of EPIC pn. Figure (b) shows the operating modes of EPIC pn (Strüder et al., 2001).

The two RGAs are built from 182 and 181 gratings. Problems in the fabrication of the gratings prevented each from having 182. They are slightly trapezoidal in shape due to the fact that the incoming light is converging. The dimensions are 100.4 mm by 200 mm and 97.5 mm. Each is made from a 1 mm SiC substrate coated with 2000 Å thick layer of gold. The groove density is variable and ranges from 626 to 656 lines per mm (den Herder et al., 2001). (They are mounted such that the grating grooves are perpendicular to the grazing incidence.) Also, they lie on the Rowland circle that includes the foci of the telescope and spectroscope, see Figure 5b. This arrangement eliminates aberrations that would otherwise be introduced (Kahn, 1990). The Rowland circle is 6698.8 mm (den Herder et al., 2001).

The RFC each consists of nine MOS type CCDs. This array is mounted in a row that conforms to the Rowland circle. Each chip is 1024 x 768 pixels with a pixel size of 27 μm x 27 μm. These chips are used in frame transfer mode. So half the chip is exposed, 1024 x 384, to the source and then transferred to the other half for storage and readout. The transfer is done very quickly, in 20 msec, and the total time to readout all of the RFC is 5.7 sec. In order to maximize the soft energy response of these CCDs they are back illuminated (den Herder et al., 2001).

CCD 4 of RGS 2 failed shortly after launch due to an electronic component in its clock driver. No XMM-Newton observations made after the first week of operation have data from CCD 4 of RGS 2. In September 2000, CCD 7 of RGS 1 failed in a similar manner. All observations after September 2000 do not include data CCD 7 of RGS 1 (XMM web site). To date there is no further damage to either RGS detector that has resulted in the loss of another CCD.

3.7. SAS and HEAsoft

Analysis of XMM-Newton data is made possible with two software suites. The first is the Science Analysis Software (SAS). SAS is a suite of software tools developed specifically for XMM-Newton by the ESA. The second is HEAsoft. HEAsoft is a suite of software packages and tools developed by NASA for high energy astrophysics. Both are open source and updated regularly.

par	value	comment
$\lambda_{\rm blaze}$	15 Å	first order blaze wavelength
δ	0.6989°	blaze angle of facets
γ	2.2751°	graze angle on facets
α	1.5762°	angle of incidence
$\beta_{\rm blaze}$	2.9739°	diffraction angle for $\lambda_{\rm blaze}$
$1/d$	645.6 lines/mm	Central groove density
CCDs	9	back illuminated, $\sim$30 μm thick
pixels	27×27 μm^2	pixel size; standard
	3×3	on chip binned
CCD size	1024×384	image area, identical storage area
T	-80 – -120 °C	nominally -80 °C

(a)

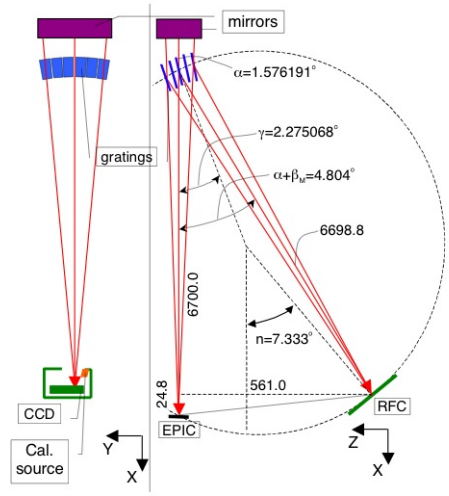

(b)

Figure 5: The table lists the parameters of RGS. Figure (b) illustrates the light path and Rowland circle for the EPIC and RGS cameras (den Herder et al., 2001).

All of SAS tools are specific to XMM-Newton. SAS is written by the XMM-Newton SOC and Survey Science Center. Tools for data reduction, creation of filters, extracts of spectra and issue of calibration are included.

HEAsoft is written for high energy astrophysics in general. It is divided into several sub-suites. XANADU is a suite for spectral, timing and image analysis using the programs XSPEC (spectral analysis) (last described by Arnaud, 1996), XRONONS (timing analysis) and XIMAGE (image analysis). FTOOLS is a suite of tools for creating, exporting and manipulating FITS files. And XSTAR (Kallman, 2010) is a photoionization code that calculates the physical conditions and emission spectra of photoionization gas in the X-Rays.

3.8. Introduction to Data Reduction and Analysis

Data for XMM-Newton is either received directly from the SOC or downloaded from the ESA archive if the data is no longer proprietary. The Observation Data Files (ODF) are downloaded and reduced.

To begin, a Calibration Index File (CIF) must be made. This is generated by the SAS command "cifbuild." Using the Current Calibration Files (CCF), this command generates an index file that points later SAS commands to the proper CCF for a given instrument. Next, a summary file of the ODFs is built with the command "odfingest." With these files made, now the event files can be made.

The event files are made with the commands "epchain" or "emchain" for EPIC pn and EPIC MOS respectively. First an attitude history is made, then for each of the CCDs, a raw event list and good time interval. This raw event list is then filtered through a list of bad pixels and corresponding events are flagged as BADPIX. Next the event list is filtered for artificial events produced by re-emission during readout, detection patterns are created and gain and change transfer inefficient corrections are performed. Finally, from the raw detector coordinates the physical camera coordinates and sky coordinates are calculated.

Once the events files are made they can be analyzed. But first a couple of items must be checked. Background flaring must be removed. Background flaring can be solar flares and wind, cosmic rays, gamma ray burst or stray electrons. To identify periods of high background, a histogram is made from the high energy background.

A time filter is then made from this histogram and new event files are made using this filter. The source must also be checked for pile-up. Pile-up is a phenomenon where two or more photons strike the detector during a read-out cycle. One higher energy photon is recorded rather than two lower energy photons. Pile-up in XMM-Newton is most likely the result of inappropriate window mode and filter. Checking for pile-up involves plotting the measured distributions of events and comparing it to predicted distributions. If there is good agreement between the two then pile-up is not an issue. None of the data presented in this work has significant pile-up.

Once pile-up is checked and high background removed, analysis can truly begin. Lightcurves for both the source and background are made. These can be made with several types of energy ranges: all 0.3 to 12 keV, soft 0.3 to 0.5 keV, mid 0.5 to 5 keV and hard 5 to 8 keV or a range that is specified. Background lightcurves are subtracted from the source lightcurves. They are then used with XRONONS to create actual lightcurves or other types of timing analysis such as hardness ratio plots or flux-flux plots.

Spectra are then extracted for both the source and background. Response matrices are then generated for these spectra. The Redistribution Matrix File (RMF) creates the map from the detector channel space to the energy space. As the EPIC CCDs are not perfect detectors, information about the effective area is included. This is done in the form of the Auxiliary Response File (ARF). The ARF takes the combined telescope, filter and detector areas to create the effective area of the observatory

and multiplies them by the quantum efficiency of the detector. This same process can be used to created spectra for different time regions through the use of a time filter.

RGS data is handled differently from EPIC data. After "odfingest" is run, a RGS specific script, "rgsproc," is run. This script involves five subscripts which do the following: creates an events file, calculates the angles for the incoming light and corrects them for changes in the spacecraft pointing, filters the events, extracts the first and second order spectra and finally, generates the response matrices. RGS data also can be checked for high background but not pile-up. High background flaring is more prominent at energies much higher than RGS operates in, but low energy flaring could still occur. Pile-up is not an issue for two reasons. First is the amount of the light being collected. At roughly 40% of the original incoming light there are simply fewer photons to pile-up. Second, the fact that RGS is a spectroscope means the light is being spread over the detectors by wavelength rather than being imaged.

Once the source spectrum, background spectrum and response matrices have been created they are loaded in "grppha" for binning. Binning of the spectra is highly dependent on the instrument. A minimum of 20 counts per bin is strived for. Depending on the length of the observation and count rate of the source, EPIC minimum binning may be much larger. The RGS data are binned such that each bin is 30 mÅ wide. After being binned, the spectra are loaded in XSPEC for analysis and spectral fitting.

The instruments do not measure the actual spectrum. They measure photon counts in a specific instrument channel, C(I). The actual spectrum, f(E), is related to the photon counts by Equation 3.1, where R(I,E) is the instrument response matrix.

$$C(I) = \int_0^\infty f(E)R(I,E)dE \tag{3.1}$$

In order to fit the spectrum, a model spectrum, M(E), with variable parameters is chosen and convolved with instrument response matrix to generate a model photon count, $C_M(I)$. This model photon count is then compared to the measured photon count via Equation 3.2. σ(I) is the error of C(I), normally defined as $\sqrt{C(I)} = \sigma(I)$.

$$\chi^2 = \sum_I \frac{(C(I) - C_M(I))^2}{\sigma(I)^2} \tag{3.2}$$

XSPEC varies the model parameters in order to minimize χ^2. Once a minimized χ^2 is reached this is the "best fit model" and "best fit parameters."

In order to judge if the fit is statistically acceptable, the "reduced χ^2" is calculated. Reduced χ^2 is defined as the χ^2 divided by the number of degrees of freedom (dof). The number of dof is the number of data channels minus the number of free model parameters. Reduced χ^2 should be approximately equal to one. Values larger than one mean the fit is inadequate and a poor one. Values smaller than one mean data's errors have been over estimated.

Once an acceptable fit has been established, the confidence interval of the model parameters is calculated. The given model parameter is changed until a critical $\Delta\chi^2$is

reached. In this work, unless stated otherwise, parameter errors are quoted at 90% confidence.

For further details of XSPEC's fit implementation see Arnaud et al. (2010).

3.9. Dynamical Spectral Method

The dynamical spectral method was used extensively in this work. The goal of dynamical spectral analysis is to gain an understanding of the source's dynamical behavior using the spectra. To do this the spectrum must be split into different regions. Typically when a spectrum is split into regions it is done with evenly sliced time or flux level segments regardless of the actual behavior the source is exhibiting. For dynamical spectral analysis, like behavior is kept together. While there are many ways of splitting the observation into groups of like behavior, in this work, like behavior includes regions of flaring, dimming, hardening, softening, or that are constant.

In order to split the spectrum into these different time regions, three lightcurves are generated. A full band 0.3-12.0 keV lightcurve, a soft band, low energy, lightcurve and a hard, high energy, lightcurve. The soft and hard band lightcurves are not chosen a priori. The choice depends on results from the time averaged spectrum and model independent tools such as the flux-flux plot and root mean square spectrum. Spectral components such as soft excess, warm absorbers, Fe Kα or other emission lines all influence the choice of energy bands.

Once the two energy bands are chosen they are plotted together along with the ratio of the hard band to the soft band. This ratio is known as a hardness ratio. The hardness ratio is then searched for spectral hardening, increase in the hard band and spectral softening, increase in the soft band. The full band lightcurve is then divided into flare, dim and constant regions. The regions are then modified by the behavior of the hardness ratio. Changes in the hardness ratio such as the softening of a constant region or the hardening of a flare result in a new time region being added. A minimum time region size of 2 ksec is imposed. While the number of counts is related to the count rate of a given observation, a 2 ksec minimum insures that the minimum number of counts in each data set are enough to use χ^2 fit statistics. Too few counts result in an over binning of the data set. With the time regions defined, time filters are made using the SAS command "gtibuild."

Source and background spectra are extracted the same way as described in Section 3.8, but with the addition of the time filter. As the instrument's response matrices change very little over the course of a single observation, the time average RMF and ARF file are used. The data is then binned and loaded in XSPEC for spectral fitting.

NGC 4051

4.1. Introduction

NGC 4051 is a narrow-line Seyfert 1 (NLS1) galaxy which resides at low red-shift (z=0.0023). The luminosity is relatively low, on the order of 10^{41} ergs/sec. However, the galaxy is well known for its variability in X-Rays. The variability takes place over long and short time scales. Order of magnitude changes over short time periods of less than six hours are a key feature of NGC 4051. It is also known for entering long periods of low activity (Lamer et al., 2003). These low flux periods are characterized by the spectrum above 2 keV becoming very flat, $\Gamma \approx 1$.

The X-Ray spectrum of NGC 4051 has several notable features. First is the power law slope. The simple power law of the spectrum above 2 keV shows a wide range of values, $\Gamma \approx 1 - 2$, with a steeper slope being required when the flux is higher. The soft band shows a substantial soft excess, which can be characterized by a simple blackbody temperature of 0.12 keV. The soft band also shows evidence of a warm absorber with the characteristic O VII and O VIII absorber edges at 0.74 and 0.87 keV. One of NGC 4051's most important features is the prominent narrow Fe Kα line at 6.4 keV.

NGC 4051 is a favorite target of X-Ray observers. It has been observed with nearly every X-Ray observatory. This includes 16 observations by ROSAT, two by ASCA, four by Chandra, a three year monitoring campaign by RXTE and 17 observations by

XMM-Newton. As such NGC 4051 is a well studied object, but poorly understood. The 2001 and 2002 XMM-Newton data have been studied a number of times and each group came to a different conclusion (Uttley et al., 2004, Pounds et al., 2004 and Ponti et al., 2006).

Uttley et al. (2004) demonstrated from the flux-flux plot that the low state data of the 2002 observation was explained by part of a continuous emission mechanism as seen in the normal flux states. They described the variability seen in the 2002 data as a pivoting power law attached to a Comptonized thermal component with constant thermal and reflection components absorbed by an ionized gas cloud. Pounds et al. (2004) analyzed the RGS data of both the 2001 and 2002 observations. They found a large number of narrow emission lines in the 2002 data and absorption lines in the 2001 data. They proposed a model with a fixed power law component and a variable absorption by a thick column of photonionized gas.

Ponti et al. (2006) concluded that the best explanation of the two data sets is a fixed constant component in the form of an ionized reflection and a variable power law component. They demonstrated that blackbody temperature did not show the proper relationship with the luminosity. Therefore blackbody radiation was not likely the source of the soft excess. (Pounds et al., 2004) used a model similar to that used in MGC-6-30-15 (Vaughan & Fabian, 2004), an ionized relativistic reflection. As described in Section 2.3.5, the flux of the ionized reflection has a direct correlation with the flux of the illuminating source when the height above the disk is small.

However when the height is larger the flux of the ionized reflection appears to be constant. while the flux of the illuminating source continues to vary (Miniutti & Fabian, 2004). This model also eliminates the need for spectral pivoting.

Part of this work reported here was published as Haba et al. (2008).

4.2. Data and Data Reduction

XMM-Newton observed NGC 4051 in May of 2001 and then again in November of 2002. In 2009 XMM-Newton observed NGC 4051 again in a series of 15 observations. Only the 2001 and 2002 data will be analyzed here.

The observations were made in the galaxy's "bright" and "dim" phases. The 2001 observation was made during the "bright phase." EPIC was used in small window mode and with a medium filter. EPIC pn and MOS2 were in spectral mode. 122 ksec worth of data was gathered. The 2002 observation was a Target of Opportunity observation that corresponded with the source in one of its periods of low activity. All three EPIC cameras were in spectral mode and large window mode. The medium filter was again used. 52 ksec of data was gathered from this observation.

The data were reduced in the manner described in section 3.9 of chapter 3. The version of SAS used was 7.2.0.

4.3. Lightcurve

To begin analyzing, lightcurves are produced after removal of background flares. The first lightcurves are made in the range of 0.3-12.0 keV, see Figure 6. The 2001 lightcurve has several large flares and flux changes of 1.5×10^{-11} ergs cm^{-2} sec^{-1} to one of 1.5×10^{-10} ergs cm^{-2} sec^{-1} in about 20 ksec, see Figure 6a. Using the hardness ratio and full band lightcurve, 16 time regions were created, see Figure 6. There are a number of flares, in Regions 2, 8, 9, and 10, and a couple of low flux Regions, 4 and 6. The rest are in between. The flares show a non-periodic behavior. This is very different from what is seen in the 2002 lightcurve. The 2002 lightcurve is notable for the periods of flaring followed by periods of low activity, called dim states, see Figure 6b. The lightcurve was then filtered into three bands: a soft band, 0.3-0.8 keV, a medium band, 1.0-3.0 keV, and a hard band, 4.0-10.0 keV. These bands were chosen for the emission mechanism and spectral features that would be dominant in each band. The soft excess and warm absorber will be most dominant in the chosen soft band. The power law will be the primary component of the medium band. And the hard band will be dominated by the components that will be discussed in Section 4.6. These filtered lightcurves are then plotted as a hardness ratio, see Figure 7. In the 2001 observation there is a dramatic hardening of the spectrum when the source is dim, as in Regions 4 and 6. But only Region 14 shows the hardening in the 2002 observation. Region 16 exhibits a softening.

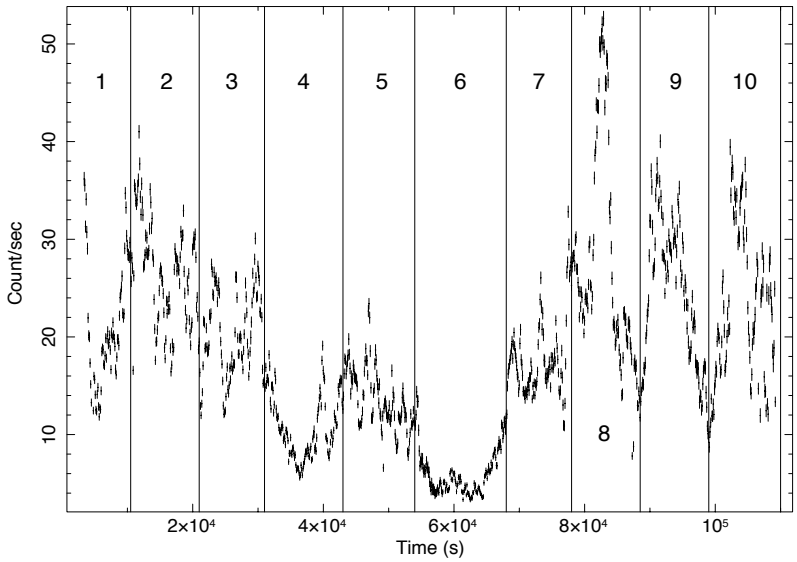

(a)

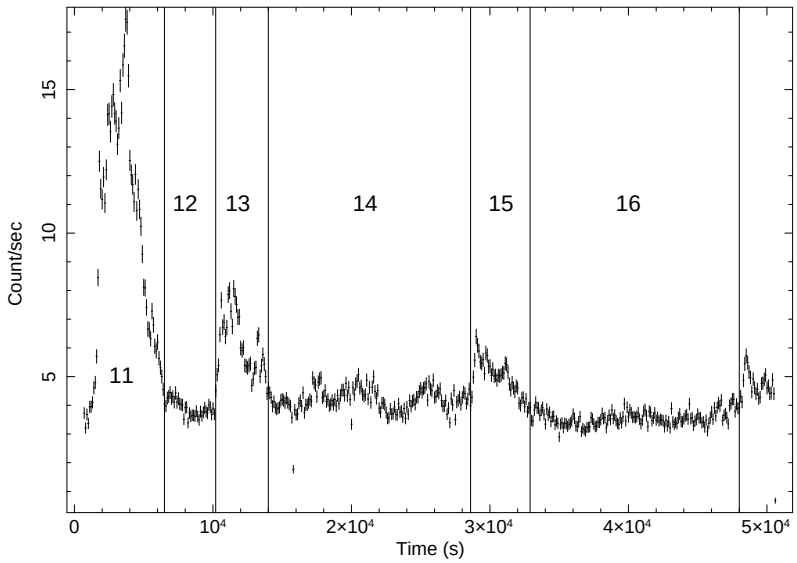

(b)

Figure 6: Lightcurves for NGC 4051. Top figure is 2001 observation, bottom is 2002 observation. The graphs are not on the same scale. Time bin is set at 100 sec. The lightcurves were divided into 16 time regions. These time regions were set by a combination of the lightcurves and hardness ratio plots, see Figure 7.

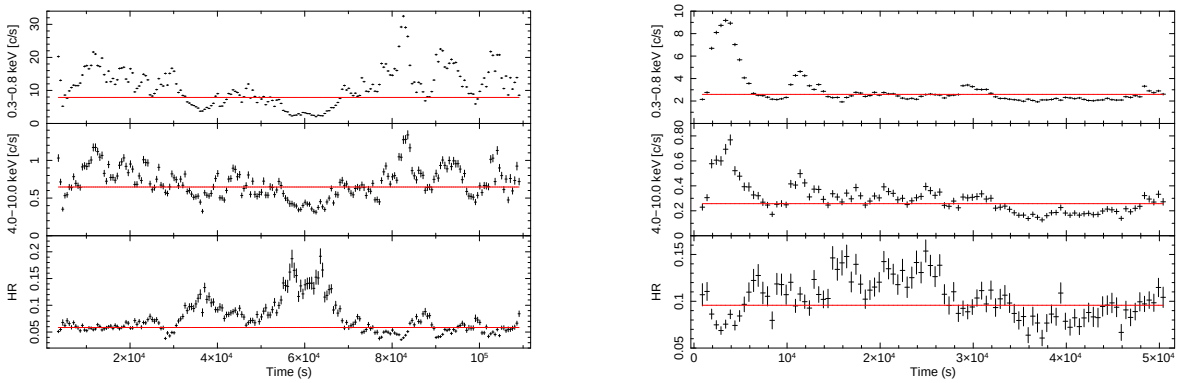

(a) (b)

Figure 7: Hardness ratio of filtered lightcurves 0.3-0.8 keV and 4-10 keV. Right figure is the 2001 observation and the left figure is the 2002 observation. Both are binned at 500 sec. The 2001 data exhibit a much greater degree of hardening as the source dims. Both observations soften as the source flares.

Time Region 16 should be noted. It is notably different from the other time regions in the 2002 observation and the 2001 observation. The variability is very low and nearly non-existent, in addition to the low count rate. This low count rate and low variability time region is unique in the XMM-Newton observations of NGC 4051. Time Region 16 will be labeled as "very dim," as opposed to "dim."

As part of a model independent way of studying the variability, flux-flux plots were made. Flux-flux plots are a plot of the count rate of one band versus the count rate of another. Such a plot is a model independent way of evaluating the relationship between model components. Next, using these same energy bands, flux-flux plots were made, see Figure 8. Using only the 2001 observation the flux-flux plot shows a more linear relationship. However once the 2002 observation is included, that linear

relationship is clearly no longer valid. The plot of the soft vs. hard bands show a "kink" as the source becomes dim. The soft vs med, however, does not show this "kink." Instead it continues to be a linear relationship. The dim phases of 2001 happen to overlap with the flare phases of 2002. Therefore it is reasonable to assume that the spectra of these two regions should be similar. The "kink" indicates the soft band's flux has essentially stopped changing as the hard and med bands continue to change to lower fluxes. In other words, the soft band has encountered a "floor" and can not continue to lower its flux as the hard does. Time Region 16 happens to be the main contributor to the "kink." This is further evidence that this region is very unusual. Based on the flux-flux plot, the majority of the variability will come from a component in this hard band.

4.4. Time Averaged Spectral Analysis

Analysis began with the time averaged spectrum. The 2001 observation was analyzed first, see Figures 9a and 9b. The band from 2.0-12.0 keV, excluding the region from 6.0-7.5, was first roughly fit with a power law model. For this fit, $\Gamma = 1.89 \pm 0.01$ was measured. A narrow, symmetric line exists in the region of 6.0-7.5 keV and appears centered at 6.4 keV, see Figure 9a. Given the narrow width and symmetric appearance, a Gaussian line was used to model this feature. A line energy of 6.36 $\pm$ 0.02 keV and width 98.3 $\pm$ 28.7 eV are measured. As the Fe $K\alpha$ line is an indicator of a reflection component, the model PEXRAV (Magdziarz & Zdziarski,

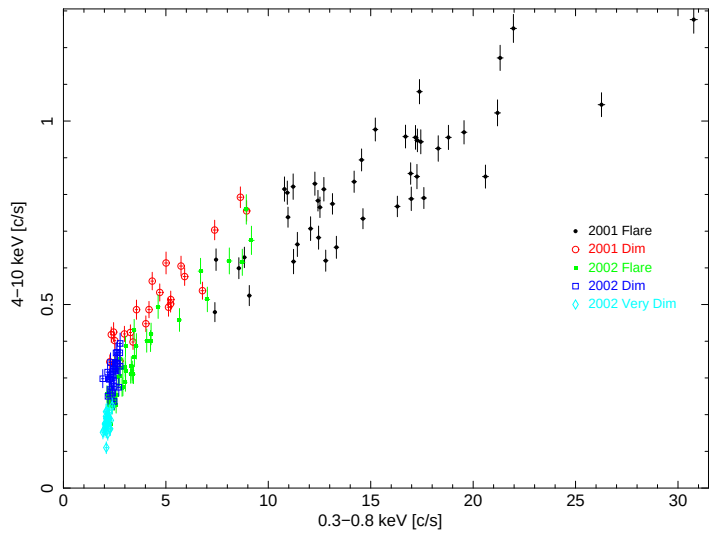

(a)

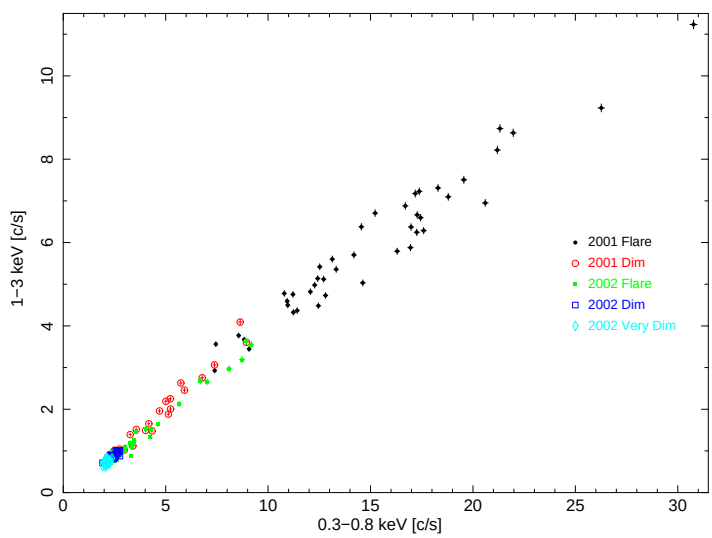

(b)

Figure 8: Flux-flux plots. The upper figure is the hard band vs. the soft band. Lower figure is medium vs. soft. The red and green data points have a strong overlap in both plots. The blue and cyan both fall away from the linear relationship the other groupings have in the upper figure. This is an indicator that the soft band has stopped changing in relation to the hard, which is still changing. The lower figure lacks this feature.

1995) is added. The model parameters adopted from Uttley et al. (2004) are assumed to be that of an isotropic source above the disk with solar abundances of metals at an inclination angle of 30°, typical of Seyfert 1s, a power law with $\Gamma = 2.1$ and cutoff energy at 100 keV.

With a reasonable fit to the data above 2.0 keV, the data below 2.0 keV was brought in, see Figure 9b. The soft excess for simplicity was modeled with a blackbody. Just by itself the blackbody does improve the fit, with kT=105.6 $\pm$ 0.2 eV and $\Gamma = 2.03 \pm 0.01$. Residuals are left in the form of an absorption edge and an emission line. The absorption edge has an energy consistent with O VII, 0.740 $\pm$ 0.008 keV. And the line is consistent with O VIII, 0.653 $\pm$ 0.013 keV. Finally, a partial covering model was used to fit the remaining residuals above 6.0 keV. A neutral cloud with a column density of 9.71$\pm$0.79 10^{22} cm^{-2} and a covering fraction of 27.6$\pm$1.6 % was found. The overall effect on the blackbody temperature and photon index is to lower the temperature, kT=102.4$\pm$0.3 keV, and raise the photon index, $\Gamma = 2.24 \pm 0.16$.

Next, the 2002 data were fit in a similar manner, see Figures 9c and 9d. In addition to being at a lower order of flux than the 2001 observation, it is also noticeably flatter. A rough fit of the data from 2.0-12.0, ignoring the region from 6.0-7.5 keV, yields $\Gamma = 1.39 \pm 0.09$. This is a very poor fit as the hard tail deviates significantly from this simple model. The region from 6.0-7.5 is then brought in. From these results an emission line is seen near 6.4 keV. The line appears broader than in the 2001 data, but is still symmetric in appearance, see Figure 9c. A Gaussian line was used to

model this emission line. The line energy is 6.41±0.10 keV and the width, which was allowed to be free, was 169.4±14.4 eV. There was no effect on Γ. Again the presence of the Fe Kα line indicates the need for a reflection component. The same PEXRAV model was used as in the 2001 data set with parameters from Uttley et al. (2004). With the addition of PEXRAV and a couple of absorption edges at 2.7 keV and 7.7 keV, an acceptable fit is obtained. However, the spectrum is still very flat with $\Gamma = 1.47 \pm 0.07$.

With the above 2 keV model set, the data below 2 keV was then included. In addition to the soft excess, a dip can be seen near 0.7 keV, indicating the presence of a warm absorber and there is a rise centered at 0.9 keV, see Figure 9b. More will be discussed about this 0.9 keV feature later, see Section 4.6. For simplicity, a blackbody is used to model the soft excess. By itself the blackbody has a temperature of 102.3±0.6 eV. But the clear edge near 0.74 keV requires the need for an absorption edge. The edge, however, does not resolve issues with rises near 0.56 keV and 0.9 keV. So Gaussian lines were used to model these features. A zero width line was used for the 0.56±0.01 keV line, which is constant with O VII and a 50 eV wide line was used for the wider feature at 0.90±0.01 keV. The change in the value of kT is minor and the value of $\Gamma = 2.16 \pm 0.10$.

As the final model used in Fukumura (2006) included partial covering, it is also added here. Leaving the covering fraction as a free parameter, the column density of the cloud was fixed at $n_H = 7.00 \pm 0.94 \times 10^{22}$ cm^{-2}. A covering faction of 50% resulted.

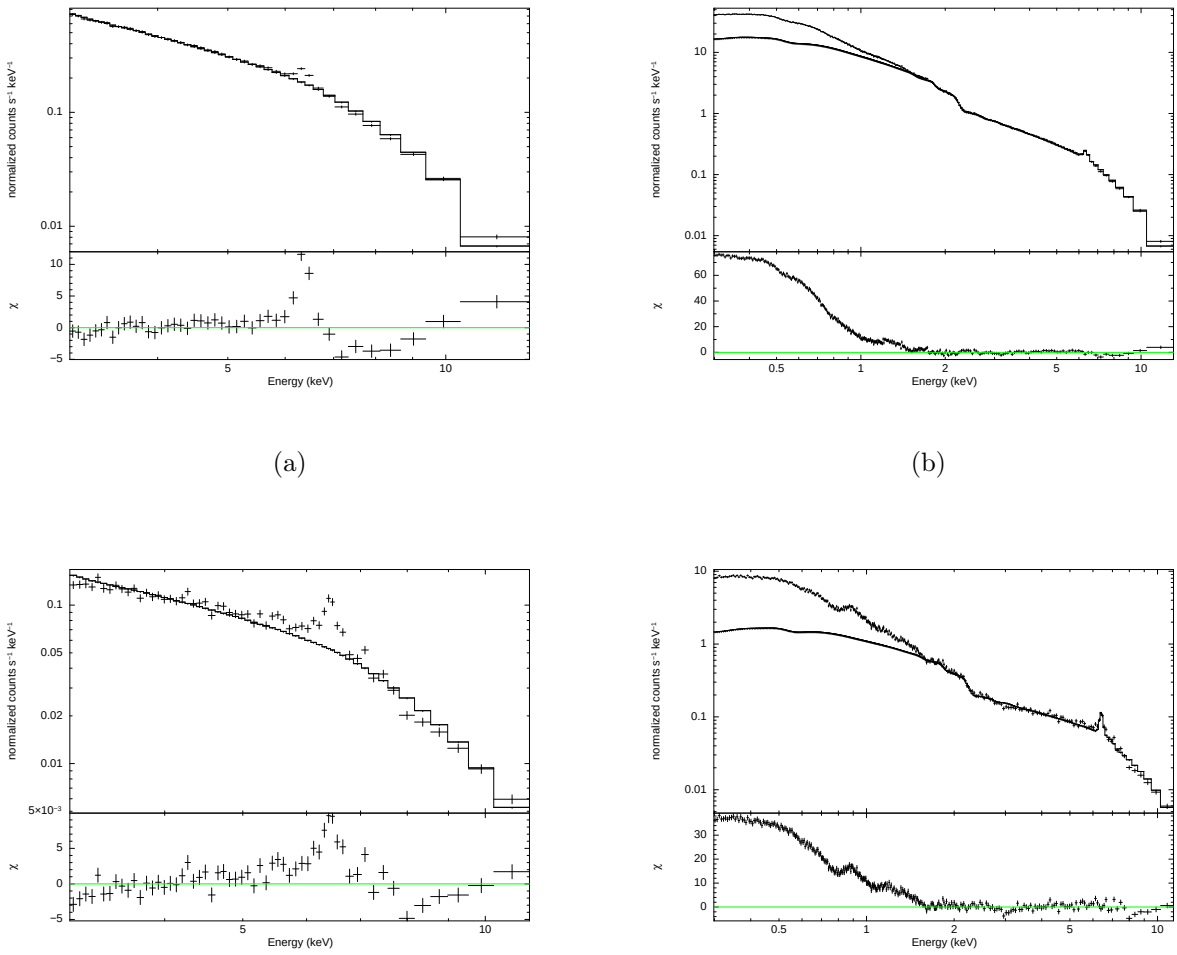

(a) (b)

(c) (d)

Figure 9: Power law only fittings. Figures (a) and (b) are for the 2001 data. Figures (c) and (d) are for the 2002 data. Residuals for the Fe Kα line and higher energy components are in Figures (a) and (c). In Figures (b) and (d) the soft excess residuals are shown. Note that in Figure (d) there is a strong presence of a warm absorber near 0.7 keV and an emission line near 0.9 keV.

The effect on the other fit parameters is minimal, except for Γ. In the case of Γ, it becomes much steeper, $\Gamma = 2.37 \pm 0.10$. Using a fixed value for $n_H = 17.51 \times 10^{22}$ cm^{-2}, see Section 4.6 for derivation, a much more acceptable value, $\Gamma = 2.18 \pm 0.07$ is obtained.

As this is an average spectrum it is expected that the features that are constant, such as the atomic features, should not change greatly in the time resolved spectra. Parameters from the variable are expected to change, but not greatly outside the error bars of a given parameter. For a description of the model parameters in Appendix A.

4.5. RGS Spectrum

Using the continuum parameters from the EPIC data, the RGS data were then fit. The power law was fixed at $\Gamma = 2.18$ and the blackbody temperature at 102.7 eV. The normalizations were allowed to be free parameters. The spectrum has a noticeable dip near 16 Å and several prominent emission lines. The emission lines near 19 Å and 22 Å are the largest. Beyond these features, the spectrum appears to be rather smooth, with only some minor other features.

The spectrum was fit by first fitting the emission lines. As in Pounds et al. (2004), eight such lines are identified, labeled in green on Figure 10. O VII triplets, O VII Lyα, Ne IX and Fe XVII are the most prominent and have the largest equivalent widths. The O VII clearly was present in the EPIC fits. Ne IX seems to be a likely candidate for the broad feature seen at around 0.9 keV in the EPIC data. However its equivalent

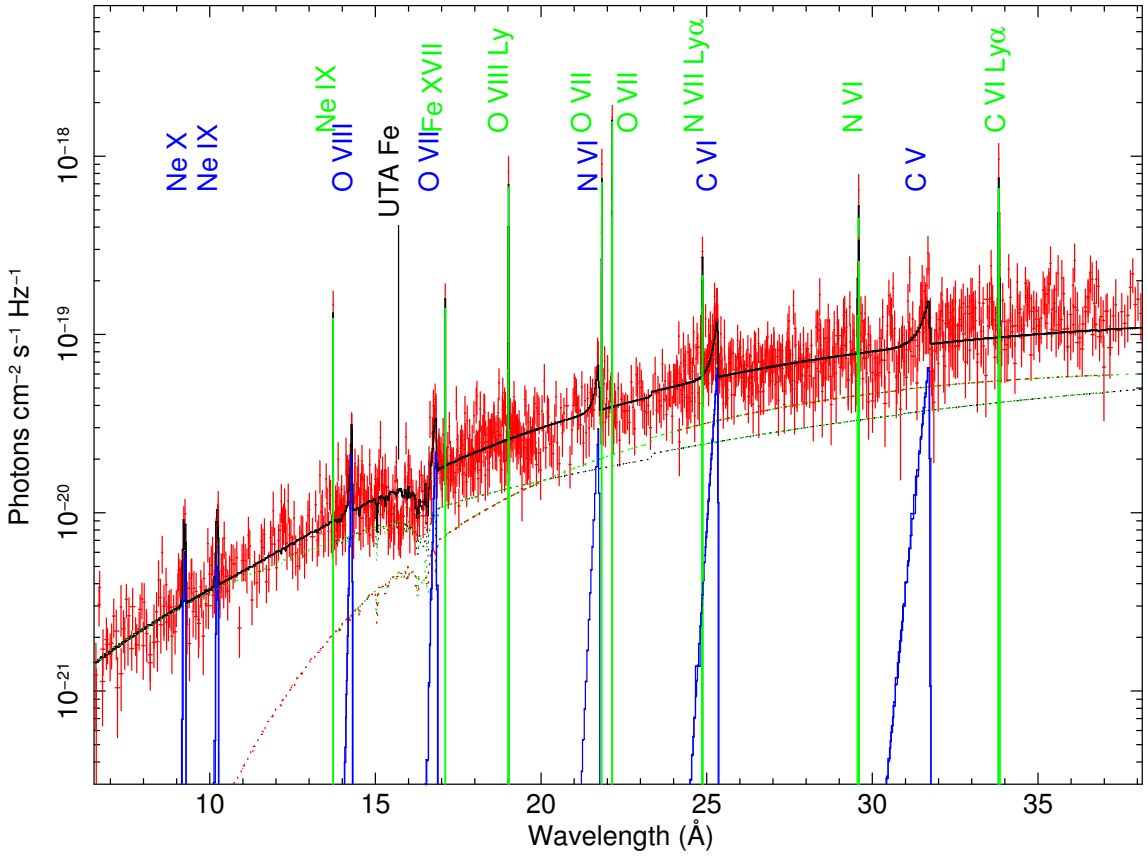

Figure 10: RGS spectrum. Narrow emission lines are labeled in green. RRC lines are labeled in blue. Absorption lines are labeled in black.

width is far too small to account for the total flux seen in EPIC. Additionally, there are three smaller and weaker lines N VI, C VI Lyα, and N VII Lyα,. These are very minor lines, each with about 2 eV equivalent widths. Aside from slightly higher flux levels, these results are consistent with Pounds et al.. See Table 2a for details.

As noted in Pounds et al. (2004), with the emission lines fit there are still some residuals left over. These are fit with a radiative recombination (RRC) model REDGE and identified. As in Pounds et al., a temperature of 3 eV is assumed for each of these

Table 1: Table (a), list of emission line features seen in NGC 4051. Table (b) list of radiative recombination (RRC) lines seen in NGC 4051.

Line	λ^{a}	Flux^{b}	EW^{c}
C VI Lyα	$33.74^{+0.88}_{-0.01}$	$6.8^{+1.6}_{-2.1}$	$2.3^{+1.3}_{-1.3}$
N VI	$29.51^{+0.20}_{-0.18}$	$4.4^{+1.5}_{-1.5}$	$2.0^{+2.0}_{-1.5}$
N VII Lyα	$24.82^{+0.23}_{-0.14}$	$2.6^{+1.0}_{-1.0}$	$1.6^{+1.8}_{-2.4}$
O VII	$22.09^{+0.02}_{-0.02}$	$17.0^{+1.8}_{-2.6}$	$13.8^{+4.3}_{-3.0}$
O VII	$21.78^{+0.03}_{-0.02}$	$8.7^{+1.2}_{-2.3}$	$6.7^{+2.5}_{-2.7y}$
O VIII Lyα	$18.98^{+0.00}_{-0.01}$	$7.2^{+1.0}_{-1.0}$	$10.4^{+2.5}_{-2.9}$
Fe XVII	$17.06^{+0.02}_{-0.02}$	$3.2^{+1.0}_{-1.0}$	$6.2^{+3.9}_{-3.8}$
Ne IX	$13.69^{+0.01}_{-0.02}$	$3.6^{+0.9}_{-0.9}$	$14.0^{+6.2}_{-6.9}$

(a)

Line	λ^{a}	Flux^{b}	EW^{c}
C V	$31.65^{+0.05}_{-0.05}$	$6.3^{+2.8}_{-2.8}$	$2.5^{+2.0}_{-1.9}$
C VI	$25.28^{+0.04}_{-0.04}$	$5.7^{+1.5}_{-1.4}$	$3.5^{+1.5}_{-2.0}$
N VI	$21.70^{+0.17}_{-0.06}$	$2.9^{+1.9}_{-1.9}$	$2.0^{+2.7}_{-2.0}$
O VII	$16.81^{+0.03}_{-0.03}$	$2.5^{+0.9}_{-0.8}$	$4.9^{+2.9}_{-2.9}$
O VIII	$14.26^{+0.03}_{-0.04}$	$2.1^{+0.7}_{-0.7}$	$6.8^{+3.8}_{-3.6}$
Ne IX	$10.22^{+0.03}_{-0.05}$	$1.1^{+0.4}_{-0.9}$	$10.5^{+12.8}_{-9.3}$
Ne X	$9.23^{+0.03}_{-0.11}$	$1.5^{+0.6}_{-0.6}$	$18.4^{+12.9}_{-12.7}$

(b)

Notes. [a] Wavelength, with units of Å. [b] Line flux in units of photon cm^{-2} sec^{-1}. [c] Equivalent width of line in units of eV.

lines. These are labeled in blue in Figure 10. Again the results are consistent with Pounds et al. (2004). See Table 2b for the list of RRC lines.

There is a large dip in the region 15.5-16.5 Å. As this feature has more of a bowl shape rather than an edge and goes beyond 16.78 Å, it is due to an Unresolved Transition Array (UTA) of M-Shell Fe. An O VII edge should be a single sharp feature, not a large dip with many smaller features, lacking sharp edges. Furthermore, there is no feature at 14.3 Å where the O VIII edge should be. Therefore, it is assumed that the warm absorber feature seen in the EPIC is due to the UTA Fe rather than

the O VII edge. There appear to be two regions. The first near 15.66 Å is larger and deeper. The wavelength is consistent with Fe XIV. The second smaller dip is near 16.16 Å and seems likely to be associated with Fe XI. It does not appear that Fe XII or Fe XIII are present, given the two distinct regions, which might hint at a two ionization phase gas. As Fe lines in this region are notoriously difficult to identify, the best that can be said is that this UTA feature is due to Fe XI - Fe XIV.

Beyond the region of the UTA Fe there are only very minor absorption features. All but one are too weak to be fit. There is a small absorption feature near 8.2 Å, which is also seen in the EPIC data. Currently the fit is too poor due to lack of statistics in the region to positively identify this feature. It is, however, consistent with the similar feature seen in the EPIC data sets. Pounds et al. (2004) note that the 2001 observation has a number of narrow absorption lines, some of which are hinted at in the 2002 data. Due to the overall dim nature of the 2002 observation and shorter observation time, the absorption features are simply lost in the noise.

4.6. Time Resolved Spectra

4.6.1. Model

Using a combination of the lightcurves and hardness ratio plots, the observation was split into 16 regions as seen in Figures 6 a and b. Ten regions were defined for the 2001 observation and six for the 2002. When several characteristic spectra are plotted on the graph, as in Figure 29, several features can be noted. First, Region 8,

the brightest flare, is much steeper and smoother than other regions. Aside from the Fe $K\alpha$ line, Region 8 would appear to be devoid of features. Region 16, the dimmest region, is the flattest spectrum above 2.0 keV and clearly shows some atomic features coming through below 2.0 keV in the form of the warm absorber and emission lines. Region 6, the lowest flux level of 2001, and Region 11, the highest flux level of 2002, are similar to one another. The fact that these regions diverge from one another below 2.0 keV illustrates the effect of the different partial covering models.

The same model and fitting procedure was used for both 2001 and 2002 observations. Minor differences were allowed in the free parameters. But there are two differences in the 2002 observation. First, the observation shows a greater number of emission lines in the EPIC cameras not seen the 2001 data. And second is the assumption that the cloud has changed.

The fitting of each of the spectra started by fitting 2.0-12.0 keV with a power law, ignoring 6.0-7.5 keV. The region 6.0-7.5 keV was then included and a Gaussian line was used to fit the narrow Fe Kα line. The width of the line is left as a free parameter. Then a neutral, distant reflector is added in the form of the XSPEC model PEXRAV. The model parameters for PEXRAV are the same as for the time averaged analysis and frozen. Next, the region 0.3-2.0 keV is brought in. The soft excess is modeled with a blackbody for simplicity. The residuals of the warm absorber are then modeled with an absorption edge at 0.73 keV. The residuals at 0.5 keV and 0.9 keV are then fitted with Gaussian lines. And finally, partial covering is added.

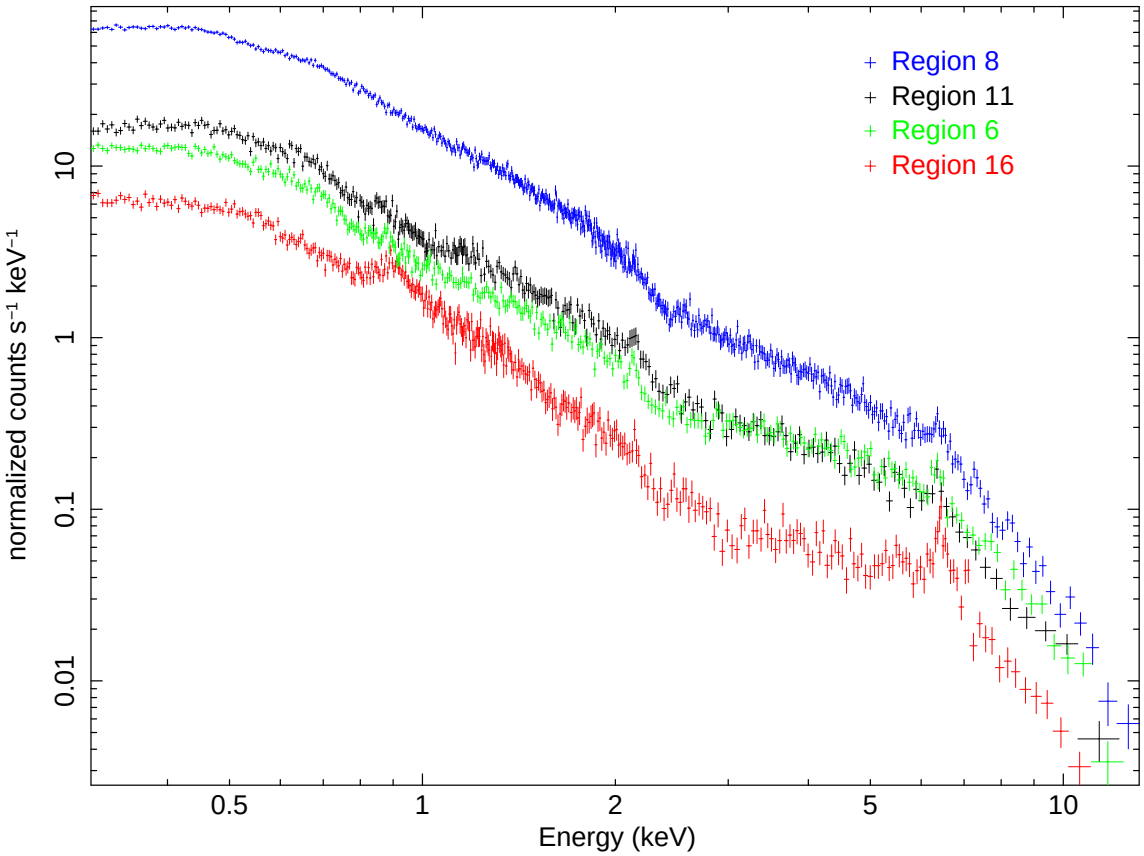

Figure 11: Four characteristic spectra of NGC 4051. Region 8 is in the blue and is the brightest flare of 2001. In addition to being very bright, it is very smooth and nearly featureless. Region 11, in black, and Region 6, in green, are from similar flux levels. Both show similar spectral features. Finally, Region 16, in red, is the lowest flux spectrum. This region exhibits several spectra features including a large effect of the warm absorber, the emergence of an emission line, and spectral flattening.

As noted in Fukumura (2006), the cloud density varies in an unusual manner. The density becomes greater when the source is brighter and under a smaller covering fraction than when it is left as a free parameter. In order to solve the problem of the cloud density, it is assumed that the cloud itself is fixed and the source changes (Fukumura, 2006). Therefore the average column density for the cloud is taken for each observation. In the case of the 2001 data set, an average n_H of 7.02×10^{22} cm^{-2} is used. With this value, again the covering fraction follows the expected behavior, see Table 2. The overall effect on the other parameters is minor. The power law and blackbody still follows the same behavior as before. As such, this is an acceptable model.

The emission lines are an important feature. The 2002 observation has different residuals in the region from 0.3-2.0 keV. In the lower flux states there are two line-like features that arise. The first is a narrow feature near 0.5 keV and the second is a broader feature near 0.9 keV. The feature near 0.5 keV was fitted with a narrow Gaussian and seems to be consistent with the O VII seen in the RGS data, see Section 4.5. The broader feature at 0.93 keV seems to have a line energy consistent with Ne IX, but is far too broad to be the feature identified by Pounds et al. (2004). Therefore, the data is refit using a thermal-emission model, MEKAL (Mewe et al., 1986; Liedahl et al., 1995) in XSPEC.

The cloud density in both observations is assumed to be constant and the source is what is changing. The source decreases in size and hence more of the bright

primary source is covered. As the observations were made more than a year apart, it is assumed that the cloud could have changed in that time period. The column density of each of the regions of the 2002 data was found to be larger than those of the 2001 observation, with the average value being close to double the 2001 average value 13.6x10^{22} cm^{-2}. However, this average column density value is not the value of 2002. Instead, the value deviated in Section 4.6.2, 17.5x10^{22} cm^{-2}, was used. No partial covering was used in Region 16.

4.6.2. Region 16: Ultra Low State

Region 16 exhibits several unusual features not seen in other time regions. In addition to being the lowest flux state, it shows very little variability, exhibits spectral hardening, has nearly stopped varying in the 0.3-0.8 band and has an extremely flat spectrum. Every other region of low flux has some minor variability in it. Region 16 is nearly flat and the change that is seen is barely above the noise level, see Figure 6. As noted in Section 4.3, this time region exhibits spectral hardening where the other low flux states soften, see Figure 7b. The flux-flux plots in Figure 8a show that Region 16 has nearly stopped changing in the 0.3-0.8 keV band, while it continues to decrease in the 4.0-10.0 keV band. This is suggests that the soft excess has reached a minimum flux level and can not go any lower. Finally, there is a flatter spectrum, see Figure 29. While the other time regions do tend to flatten out as the source becomes dimmer, Region 16 is quite extreme.

Early attempts in modeling this region focused on the flattened spectrum. The partial covering is a component capable of explaining the flattening. However, the model doesn't seem to flatten in this region as it requires either a very thick cloud, $n_H \approx 50x10^{22}$ cm^{-2}, or a very steep $\Gamma \approx 2.7$. The model is rejected based on the non-physical parameters. It also fails to take into account other points that make Region 16 unique.

In order to explore this uniqueness further, a differential spectrum was made from Region 14 and Region 16, see Figure 12b. The basic idea of the differential spectrum is that the spectra are made of constant and variable components. By subtracting one from the other, the constant components drop out and the variable components are left. When this is done one can clearly see a hump peaked at around 5 keV. This is the type of spectrum that is expected for a partially covered source. What is concluded is that Region 14 has partial covering and Region 16 has either very little or no partial covering. More will be discussed on what this means in Section 4.7.1.

To fit this differential spectrum, a simple partial covering model was first used. Γ is a little too big for this; $\Gamma = 2.57$ is much larger than is expected or acceptable. There are some residuals in the soft spectrum. So a blackbody is added. While the temperature is very close to what is seen in the actual spectra, kT = 107 eV, Γ is still much flatter, 1.54. The direct power law is then assumed to be covered by an additional absorber. This model results in a $\Gamma = 2.08$ and is within the error bars of the measured value and close to the minimum value seen in the early fitting. The

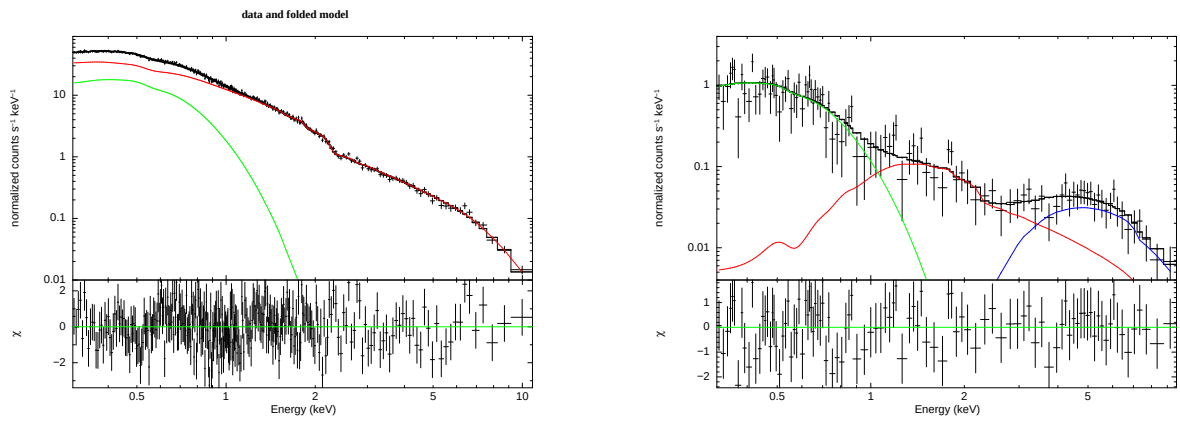

(a) (b)

Figure 12: Differential spectrum. Left figure was made by subtracting Region 6 from Region 8. The only variable pieces in this model were blackbody and power law. Right figure was Region 16 subtracted from Region 14. In this case there is clearly another component, in the form of a partial covered component.

column density, n_H=17.5x10^{22} cm^{-2}, while slightly greater than the average column density from the early fitting, is physically acceptable and was used in the refitting of Regions 11-15.

4.6.3. Feature at 0.9 keV

The line at 0.9 keV as previously fit was a Gaussian. A best fit parameter of 0.93 keV was used for the line energy, a line width of 50 eV and flux of 1.2x10^{-4} photons cm^{-2} s^{-1}. The line energy is consistent with Ne IX triplet seen in the RGS data as reported in Pounds et al. (2004). However, the line width, intensity and equivalent width are problematic as they are an order of magnitude larger in the EPIC than in the RGS data. If there is an optically thin thermal plasma in the system, Fe L lines are

expected to form a broad feature peaked near 0.9 keV (Haba et al., 2008). Therefore, the data is refit using a thermal-emission model, MEKAL (Mewe et al., 1986 and Liedahl et al., 1995) in XSPEC. The plasma temperature was found to be 0.70 keV. This is similar to that of Seyfert 2 galaxies with starburst activity (Levenson et al., 2001). While this temperature is slightly lower than the mean temperature reported in Levenson et al. (2001), it is well within the range. Mrk 1239 is noted by Grupe et al. (2004) as having similar features and a partially absorbed power law.

The line feature at 0.9 keV along with the 0.56 keV line is only seen in Regions 12,14,15, and 16 of the EPIC data. These features are believed to be constant. The line fluxes bear this assumption out. There is only a minor change in the line fluxes for each region. Therefore it is reasonable to assume these features are present in the higher flux states also, but overpowered by the brighter continuum components. As such, the MEKAL model is only used in Regions 12,14,15, and 16 where the feature is seen.

4.6.4. Model summary

A summary of the final model is: The continuum components are a power law with a Γ that is allowed to pivot between 2.0 to 2.3 and a free normalization, blackbody with a free temperature and normalization, a fixed cold distant reflector, and for Regions 1-15, a neutral dense cloud that partially covers the direct power law source. Atomic features include a narrow Fe $K\alpha$ line at 6.4 keV modeled by a Gaussian line. An absorption edge near 0.74 keV is used to simulate the warm absorber's primary

Table 2: Covering fraction and luminosities. As the covering fraction increases the luminosity decreases.

	CF %	Soft Lum[a]	Hard Lum[b]	χ^2 (d.o.f.)
1	$21.9^{+2.2}_{-2.2}$	$53.87^{+0.40}_{-0.45}$	$30.49^{+0.37}_{-0.44}$	1.08 (319)
2	$24.6^{+1.5}_{-1.6}$	$61.38^{+0.34}_{-0.25}$	$35.43^{+0.41}_{-0.39}$	1.09 (319)
3	$25.9^{+1.8}_{-1.8}$	$48.43^{+0.33}_{-0.24}$	$28.98^{+0.44}_{-0.33}$	1.07 (313)
4	$41.1^{+1.5}_{-1.7}$	$24.33^{+0.21}_{-0.21}$	$21.12^{+0.38}_{-0.28}$	1.00 (338)
5	$27.5^{+1.9}_{-2.0}$	$32.41^{+0.26}_{-0.24}$	$24.90^{+0.33}_{-0.37}$	1.06 (338)
6	$59.3^{+1.2}_{-1.2}$	$12.66^{+0.14}_{-0.15}$	$14.79^{+0.27}_{-0.32}$	1.11 (340)
7	$17.7^{+2.3}_{-2.4}$	$40.15^{+0.37}_{-0.30}$	$24.04^{+0.35}_{-0.43}$	1.05 (323)
8	$26.1^{+1.6}_{-1.7}$	$68.16^{+0.38}_{-0.30}$	$35.78^{+0.41}_{-0.45}$	1.12 (307)
9	$23.8^{+1.8}_{-1.8}$	$58.18^{+0.30}_{-0.42}$	$30.86^{+0.39}_{-0.39}$	1.25 (312)
10	$24.5^{+2.0}_{-2.2}$	$60.51^{+0.33}_{-0.37}$	$32.21^{+0.41}_{-0.50}$	1.05 (319)
	CF %	Soft Lum[a]	Hard Lum[b]	χ^2 (d.o.f.)
11	$13.8^{+3.5}_{-6.6}$	$17.63^{+0.27}_{-1.80}$	$13.97^{+0.72}_{-2.26}$	1.11 (323)
12	$69.0^{+3.9}_{-4.6}$	$7.08^{+0.49}_{-2.01}$	$6.61^{+0.55}_{-1.66}$	1.12 (268)
13	$35.1^{+3.4}_{-4.0}$	$9.12^{+0.21}_{-0.72}$	$8.80^{+0.50}_{-1.46}$	1.13 (315)
14	$65.4^{+6.7}_{-4.4}$	$7.33^{+0.54}_{-0.82}$	$7.53^{+0.44}_{-0.78}$	1.02 (320)
15	$23.0^{+8.0}_{-9.4}$	$8.34^{+0.39}_{-2.35}$	$7.21^{+0.57}_{-2.41}$	1.04 (317)
16	-	$6.35^{+0.25}_{-0.23}$	$4.45^{+0.24}_{-0.07}$	1.09 (295)

Notes. [a] 0.3-2.0 keV luminosity, with unit of 10^{40} ergs sec^{-1}. [b] 2.0-10.0 keV keV luminosity, with unit of 10^{40} ergs sec^{-1}.

feature of UTA Fe. The 2001 observation has a Gaussian line near 0.63 keV to model an O VIII emission line and in the 2002 observation a Gaussian is used at 0.56 keV to model an O VII emission line. And finally, for the lowest flux states a thermal plasma model MEKAL was used to model thermal emission from L shell Fe. Results for each region can be seen in Table 8 of Appendix B for the continuum components and Table 9 of Appendix B for the atomic features. Figure 13 shows model components in four characteristic cases: Region 6, the lowest flux states of 2001, Region 8 the highest flux state, Region 14 the lowest active flux state and Region 16 the inactive flux state.

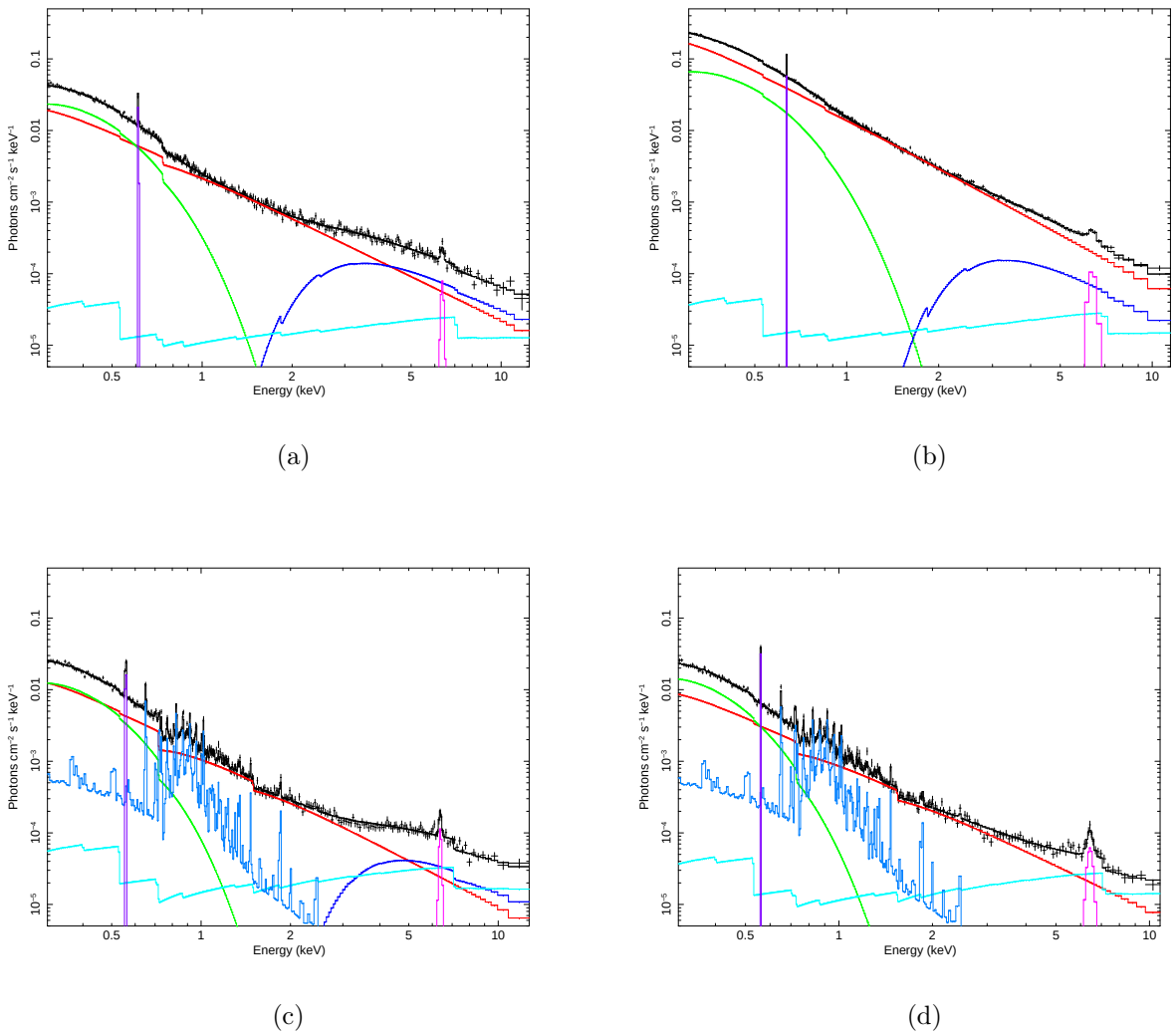

Figure 13: Unfolded spectra of final model for Regions 6, 8, 14 and 16. The components are colored as follows: Power law is red, Blackbody is green, Partial Covering is dark blue, Reflection is cyan, Mekal is medium blue, O VII or VIII is purple and Fe Kα is magenta. (a) Region 6 has the large partial covering and fewer features. (b) The power law is very much the dominant component in Region 8. (c) Region 14 has a thicker cloud and large partial covering as well a major contribution from the atomic features. (d) Region 16 has no partial covering, but a great contribution by the reflection and the atomic features.

4.7. Discussion

4.7.1. Interpretation of Region 16

Region 16 is a very important region for understanding what is going on in NGC 4051. As stated in Section 4.6.2 Region 16 is the lowest flux state, shows very little variability, exhibits spectral hardening, has nearly stopped varying in the 0.3-0.8 band and has the flattest spectrum. The differential spectrum between Regions 14 and 16 indicates there is a component in Region 14 that appears to be a partial covering by a thick cloud, but somehow is not present in Region 16. What is concluded from the differential spectrum is that the partially covered component is absent in Region 16. How can the partially covered component have no relevance in Region 16 when it was asserted that a higher percentage of partial covering accounts for lower flux levels in the other regions?

In order to understand the answer, it is worth reviewing what the partial covering is. The version of the partial covering used here assumes that a cloud made of neutral hydrogen partially covers the direct source. The cloud is of fixed density on short time scales, but can vary on longer time scales. What is seen is a combination of the primary source and the reprocessed source after it passed through the cloud, as illustrated in the cartoon of Figure 14a. When the source is bright the emission region enlarges. As the cloud is fixed the covering fraction must become smaller. When the source dims, the emission region shrinks and the cloud's covering fraction becomes larger. However in the case of Region 16, the emission region has become

so small that the primary source becomes negligible. In other words, the source has entered an "off" phase. As the primary source is negligible so is the partially covered component. What is left is the temporally stable component, in this case the cold distant reflection.

The assumption that the cloud is fixed and that the source is varying is made in the analysis of the 2001 data set and works very well. This idea is born out when the differential spectrum is made for the 2001 data, see Figure 12a. This differential spectrum clearly lacks the hump seen in the 2002 differential spectrum. It has only power law and soft excess components, modeled here as a blackbody. A similar assumption was made for Regions 11-15. A constant cloud results in a stable Γ of around 2.1, a blackbody temperature that increases with the flux and a covering fraction that decreases as the flux increases. If, however, it is assumed that there is no partial covering in Region 16, the desired continuum features are achieved. Now the differential spectrum's shape and the flux-flux plot can be understood to represent a "turn off" of the emission region. As the source enters into the temporally stable phase, the emission region, the corona, becomes smaller. At some point the region is simply too small to be partially covered and is considered to be "off," as illustrated in cartoon of Figure 14b.

The other remaining question is what causes the spectrum to flatten out if not caused by the partial covering? The flattening in the 2.0-10.0 keV band is caused by a combination of the low flux level and stable components, which is a reflection

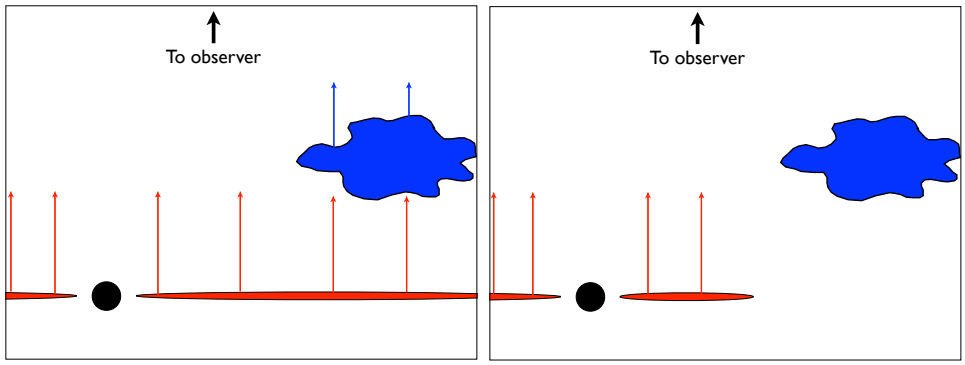

(a) (b)

Figure 14: Cartoons illustrating the partial covering scenario, items not drawn to scale. The primary emission region is in red and the reprocessed light from the cloud is in blue. Figure (a) shows the cloud partially covering the primary emission region. As the primary emission region grow and shrinks, the cloud stays fixed. Figure (b) shows the smaller emission region of Region 16. The emission region is now too small to be covered by the cloud.

component in this band. The reflection component is assumed to be fixed as it represents a Compton scattering off cold distant material tied to the Fe line. In bright regions like Regions 8, 9 and 10 this reflection component contributes very little to the over all flux. When the flux levels drop down to levels seen in Region 16, what was a minor component is now a major component. The reflection component represents a "floor" in the hard spectrum. As the high variable components drop and enter this "off" phase, the constant "floor" components shine through and alter the shape of the spectrum.

4.7.2. Connection to Starburst Galaxies

As mentioned earlier, the line at 0.9 keV is a common feature seen in Seyfert 2 galaxies with starburst activity (Levenson et al., 2001). As described in Haba et al.

(2008), NGC 4051 could be showing the early signs of starburst activity. Ranalli et al. (2003) showed that in starburst galaxies there is a well known, clear and tight relationship between the X-Ray luminosity and far infrared luminosity for the thermal emissions. Ranalli et al. (2003) assume slightly different cosmological parameters than what have been used here. For consistency in comparing with Ranalli et al. (2003), a Hubble constant, $H_0 = 50$, and a deceleration parameter, $q_0 = 0.1$, will be used. With an estimated far infrared flux (FIR) of 6.56×10^{-10} ergs cm^{-2} sec^{-1}, a $L_{FIR}$was calculated to be 1.9×10^{43} ergs sec^{-1}. At the new soft X-Ray band of 0.5 -2.0 keV, luminosity was calculated from the time averaged spectrum using the new cosmological parameters, 1.08×10^{41} ergs sec^{-1}. When plotted on the Ranalli et al. (2003) graph, NGC 4051 nicely fits in the lower luminosity end of the graph, implying that NGC 4051 has yet another characteristic of a starburst galaxy. Rodriguez-Ardila & Viegas (2003) found evidence of 3.3 μm polycyclic aromatic hydrocarbon (PAH), a very strong indicator of starburst activity. As Haba et al. (2008) note, starburst galaxies are capable of producing a torus type structure around the central engine that is inhomogeneous and turbulent. The partial covering model discussed here could be related to starburst activity.

4.7.3. Soft Excess

Ponti et al. (2006) very successfully modeled the same data with a relativistic ionized reflection model. The case they made for the relativistic ionized reflection model is a strong one and not easily dismissed. So the question arises, why was a

simple blackbody used when Ponti et al. (2006) have shown how well the relativistic ionized reflection model works? First and foremost, the blackbody was used for its simplicity. A blackbody is a very simple model. The blackbody used here has two parameters. The ionization reflection model, REFLION (Ross & Fabian, 2005) with relativistic blurring is much more complicated. When REFLION is used with KDBLUR there are eight total parameters with four free. Second, explaining the soft excess was not the goal of this work. The goal was to explain the overall variability of the system, and while the soft excess is an important part, it is hardly the most dominant. The third was lack of strong need. The strong evidence to force the need to use a relativistic ionized reflection model was not there. The Fe Kα line in NGC 4051, while broad, has a line width under 180 eV wide, making the parameters for a relativistic line profile difficult to fit. Nandra et al. (2007) suggests the line is formed within 50 gravitational radii from the central engine. The RGS data show a generally smooth spectrum with an emission line significantly narrower than the Fe Kα. As such, the two areas of the spectrum most useful for pinning the fit parameters of the model yield no relevant information.

While simple, the blackbody is far from perfect. The model used here is problematic for two reasons. First, the temperature is too constant, as it does not follow the correct T^4 relationship. Ponti et al. (2006) clearly shows this in their Figure 10. Second, the temperature is too high for the standard alpha disk model. Both of these

problems are well known characteristics of the NLS1 galaxies and can be partially solved by using a more sophisticated slim disk model (see Mineshige et al., 2000).

These results are not necessarily incompatible with the relativistic ionization model (Haba et al., 2008). Meaning that the variability seen in NGC 4051 could be caused by both a partial covering and a relativistic ionized reflection model.

4.8. Conclusion

The 2001 and 2002 XMM-Newton data set of NGC 4051 were analyzed with an emphasis on temporal flux and spectral variability. These were done in tandem, but with the emphasis of the 2002 data set.

In the flare and early dim phases of the 2002 data the partial covering model proposed for the 2001 data set works well. The model has to be modified slightly in order to explain the final dim state of 2002. The model is then summarized as such: in the bright phases, the emission region is larger than the covering cloud. When the flux level of the unabsorbed power law changes due to a change in the size of the emission region, the absorbed power law remains relatively unchanged. As the emission region shrinks and becomes smaller than the cloud, the absorbed power law decreases in response to the smaller emission region. In the case of Region 16, the emission region has become so small that the absorbed power law no longer contributes and other temporally stable components, such as the distant, thin thermal plasma, become much more dominant.

These temporally stable states have demonstrated features similar to that observed in Seyfert 2 galaxies with starburst activity. The work in the infrared and radio also points to the possibility of starburst activity in NGC 4051. The starburst-like activity that is strongly hinted at would be useful for future radio and infrared observations as well as X-Rays. NGC 4051 could serve as an important link in the understanding of the evolution of galaxies. With 15 additional XMM-Newton observations made in 2009, follow up analysis of this source is possible to further test this model.

IRAS F12397+3333

5.1. Introduction

IRAS F12397+3333 (Was61, 1RXS J124211.3+331703) is a low redshift (z = 0.0437) Narrow-Line Seyfert 1 (NLS1) galaxy. This NLS1 is notable because of the optical polarization observed in the source. Grupe et al. (1998) found the average optical polarization of IRAS F12397+3333 to be 3.77±0.20%, the second highest of their sample set of 43 galaxies. They also showed the optical polarization to be wavelength dependent, increasing at shorter wavelengths, see Grupe et al. (1998) Figure 4. Prior to this observation with XMM-Newton, IRAS F12397+3333 had been observed with ROSAT as part of the ROSAT All Sky Survey and with ASCA. From the ROSAT observation the presence of a warm absorber was established and from the ASCA observation the presence of a Fe Kα line (Wills et al., 2007).

5.2. Data Reduction

XMM-Newton observed IRAS F12397+3333 once in 2005. EPIC pn was operated in full frame window mode and EPIC MOS 1 and 2 were operated in large window mode.

The data was reduced in the manner described in Section 3.9 of Chapter 3. SAS version 7.2.0 was used. After the data was reduced, background flares were checked for and removed. A total of 81 ksec was deemed usable. The source and background

regions were taken from a circle 50 arcsec in radius. The backgrounds were from empty regions of the same chip.

5.3. Lightcurve

The lightcurve for 0.3 to 12 keV band of the XMM-Newton observation is really flat and shows limited variability, see Figure 15. Overall the lightcurve shows a trend towards a slightly higher count rate as the observation goes on. The early half shows a little more variability than the latter half. There are two periods of higher count rates that slowly decay away before jumping back to the lower count rate. In between these two periods there is a minor flare. The latter half of the observation shows a fairly stable lightcurve with some minor flaring towards the end.

A soft, 0.3-2.0 keV, and a hard, 2.0-12.0 keV, filtered lightcurve was made next and their hardness ratio was plotted, see Figure 16a. Some areas worth noting are the hardening near the beginning of the observation and minor flaring near the end. Between about 20 to 30 ksec the lightcurve is noticeable harder. This corresponds to the period of greatest variability. A pair of minor flares near the end of the 0.3-2.0 keV filtered lightcurve that do not appear in the 2.0-12.0 keV filtered lightcurve, resulting in a slight softening.

A RMS spectrum (Edelson et al., 2002 and Ponti et al., 2004) for this observation was generated using a time bin size of 2 ksec. The spectrum is very flat and has a low average RMS value. This indicates that in this observation of IRAS F12397+3333

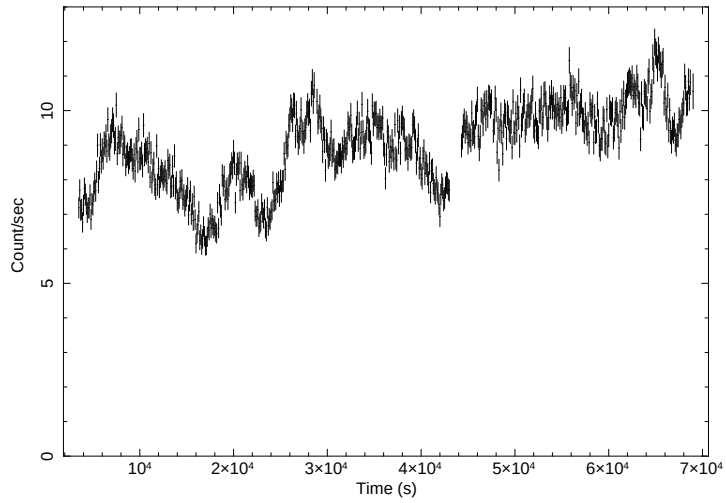

Figure 15: EPIC lightcurve. Lightcurve has been background subtracted and is binned at 100 sec. Notice the higher level of flaring in the first half of the lightcurve compared to the second half.

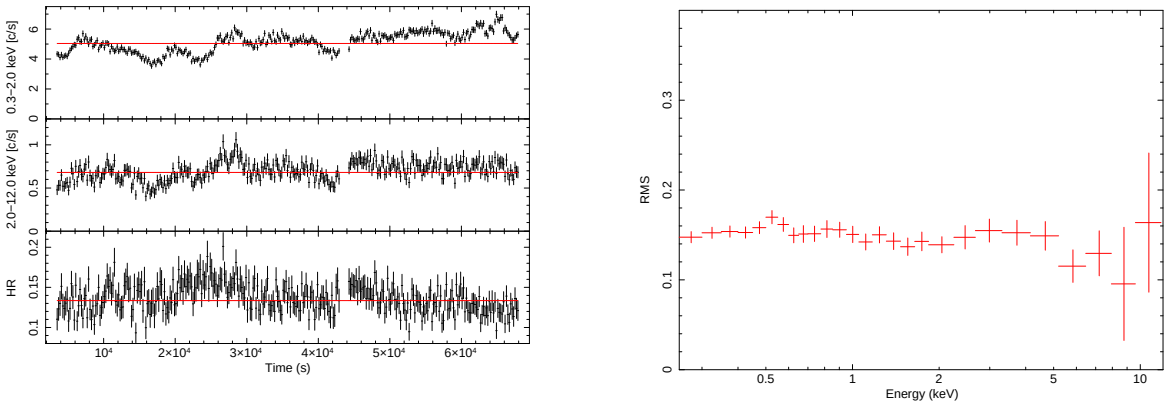

(a) (b)

Figure 16: (a) Hardness ratio. Top plot is the 0.3-2.0 keV lightcurve. Middle is the 4.0-10.0 keV lightcurve. The bottom plot is the hardness ratio of the two. There is a slight hardening of the spectrum near 20 ksec. Also of interest is a pair of flares near 60 ksec in the 0.3-2.0 keV lightcurve that seem to have no counter parts in the 4.0-10.0 keV lightcurve. (b) RMS spectrum. The flat RMS spectrum indicates that the variability is caused by a component that varies across the whole band.

the variability is evenly spread across the whole XMM band. The difference between the high and the low flux states is caused by a change in a component with a broad spectral range, mostly a change of the flux level of the power law component.

5.4. EPIC Analysis

Spectral analysis of the EPIC data began by first looking at the hard spectrum. EPIC pn, MOS 1 and MOS 2 were fitted simultaneously. The time averaged spectrum from 3.0 keV to 12 keV, excluding 6.0 keV to 7.5 keV in case of iron emissions and absorptions, was fit with a power law model. The neutral hydrogen column density is frozen at the galactic value, 1.34 x 10^{20} cm^{-2} (Dickey & Lockman, 1990). As three sets are being fit simultaneously, the value of the power law photon index, Γ, were linked together, but the normalizations are left as independent parameters. A statistically acceptable fit is achieved with a $\Gamma = 2.09 \pm 0.04$.

Next, the region of 6.0 keV to 7.5 keV is added back in. The same simple power law model is used. Again a statistically acceptable fit is achieved, but with a slightly flatter $\Gamma = 2.06 \pm 0.03$. Although this fit is statistically acceptable, there is deviation from the model. At around 7.5 keV there is an edge, see Figure 17a. An absorption edge is added to the model. The addition of the edge greatly improves the fit of the model and flattens Γ farther. Γ is now 1.97 $\pm$ 0.04 and the value of the absorption edge is 7.67 $\pm$ 0.10 keV. Second, there is a small hump around 6.4 keV, see Figure 17a. The addition of a Gaussian centered near 6.4 keV again improves the fit. The

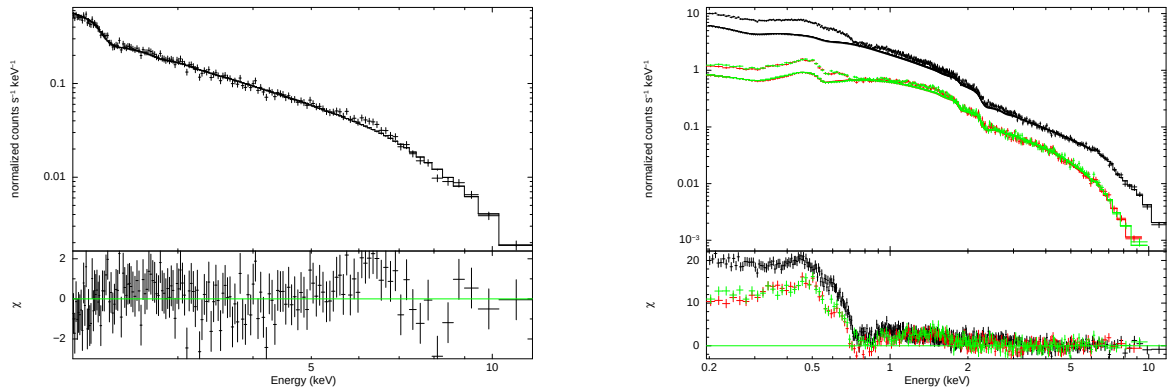

(a) (b)

Figure 17: Figure (a) hard spectrum with only a power law model. Only EPIC pn data shown for clarity. Notice the slight rise near 6.4 keV and the drop near 8.0 keV. These are consistent with an Fe Kα line and Fe absorption edge. Figure (b), show the soft excess. The black data points are EPIC pn data, the red and green are EPIC MOS. Data below 1.0 keV exceeds the model. The effect of a warm absorber can be seen near 0.6 keV

line energy is 6.55 $\pm$ 0.09 keV with a line width of 0.14 $\pm$ 0.11 keV. The line has a very low flux, 2.97 $\pm$ 4.22 x 10^{-6} photons cm^{-2} sec^{-1} and equivalent width of 74.5 eV. The effect on Γ is to steepen it slightly, $\Gamma = 2.00 \pm 0.04$. Although the presence of a Fe Kα line is an indicator of a reflection component, no reflection model is used here. Neither the fitting statistics nor data residuals indicate that a reflection model is needed. Given how low the line flux is it is likely that the reflection component is a very minor component in the EPIC band.

With the hard spectrum fit done, the focus shifts to the soft. Channels corresponding to energies 0.2 keV to 3.0 keV are now included. The first thing to note is that the current power law model, with $\Gamma = 2.0$, is a reasonable fit to the data down

to 2.0 keV, and can be a reasonable fit down to 1.0 keV, with $\Gamma = 2.09$. The soft excess deviates from the model starting at values of 1.0 keV, see Figure 17b. There is a significant dip between 0.7 and 0.9 keV. This has previously been identified as the warm absorber with O VII and O VIII absorption edges at 0.74 keV and 0.87 keV respectively. More will be discussed about this later. Three types of models for the soft continuum will be considered here: a blackbody, blurred ionized-reflection and a broken power law.

When the blackbody model is added there are a couple of deviations from the model, particularly around 0.7 keV. These were then fitted with absorption edges. While acceptable from a purely statistical point, from a physical point of view the model is unacceptable. The blackbody temperature is far too high. At 154.6 ± 3.2 eV this is simply too high to be reasonably accepted. In case of a Shakura Sunyaev disk an accretion rate greater than six orders of magnitude larger than the Eddington rate would be needed to sustain a this high a temperature in the inner disk region (Shakura & Sunyaev, 1973). For an advection dominated disk, such as slim disk model, again requiters a very large super Eddington accretion to support this high a disk temperature (Mineshige et al., 2000). Therefore the simple blackbody model is rejected as the model of the soft excess.

Next a blurred ionized reflection model, REFLON (Ross & Fabian, 2005), was tried. This model was convolved with a relativistic blurring model using a Laor line profile (Laor, 1991), KDBLUR. Several assumptions have to be made when using

this model. First, as the Fe Kα line is only moderately broaden and likely originates further away than the inner disk region. So the relativistically broaden Fe Kα line is a weak feature, which mean a super solar abundance of Fe is not needed. Second, IRAS F12937+3333 is a typical Seyfert 1 and typical inclination angles are 30° to 40°. An inclination of 40° will be used. Finally, as the RGS spectrum is "smooth" and lacking the saw tooth look of sources that have relativistic emission lines, it can be assumed that a smaller inner radius should be used. In this case an inner radius of 1.3 r_g was used. With the addition of absorption edges at 0.72 keV and 0.18 keV, this model yielded a reasonable fit. The emissivity index, q, and ionization parameter, ξ, were left free, along with the normalization. The best fit parameters for each were q=3.87 $\pm$ 0.12 and $\xi = 36.2 \pm 2.8$ ergs cm s^{-1}.

The broken power law, in addition to the hard spectrum model, results in a terrible fit. From a statistical perspective the fit is unacceptable. The model deviates from the data too much, most notably at around 0.74 keV. The addition of an absorption edge greatly improves the fit. The edge energy is 0.727 $\pm$ 0.003 keV. The addition of two more absorption edges, at 0.837 $\pm$ 0.020 keV and 0.236 $\pm$ 0.008 keV, brings the model into a reasonable fit. The EPIC MOS data indicates that there is another absorption feature near 0.28 keV. EPIC pn does not show such a deviation from the model. When fitted with a Gaussian absorption model, the feature has a line energy of 0.298 keV and is therefore very likely a C V absorption.

A differential spectrum was created by subtracting the lower flux state from the higher flux state. This differential spectrum was smooth with very few features. It was well fit by a power law. The one noticeable feature was a small dip near 0.7 keV. An absorption edge was used to model this feature and that improved the overall fit. The fact that the differential spectrum is well modeled by a power law is consistent with the fact that the RMS spectrum was very flat and had a low average RMS value, expected for a source that shows very little variability.

The low and high flux spectra were then fit. The same models were used on both. There was no significant difference between the two sets of fit parameters, other than the power law's normalization, which is an indicator of flux state. In the higher flux state it has a larger value and slightly higher photon index.

5.5. RGS Analysis

With the continuum model set from the EPIC data, analysis of the RGS data can begin. The broken power law model will be used here. The blackbody is not physically plausible given the high temperature required and the blurred ionized-reflection model is a very complicated model that lacks overwhelming evidence. As the brake in the power law takes place outside the RGS range, a simple power law model will be used as the continuum model. The photon index and normalization values are frozen at those derived from the EPIC fitting. The absorption edge for C at 43.65 Å was also added to the model. The feature is outside the RGS range and

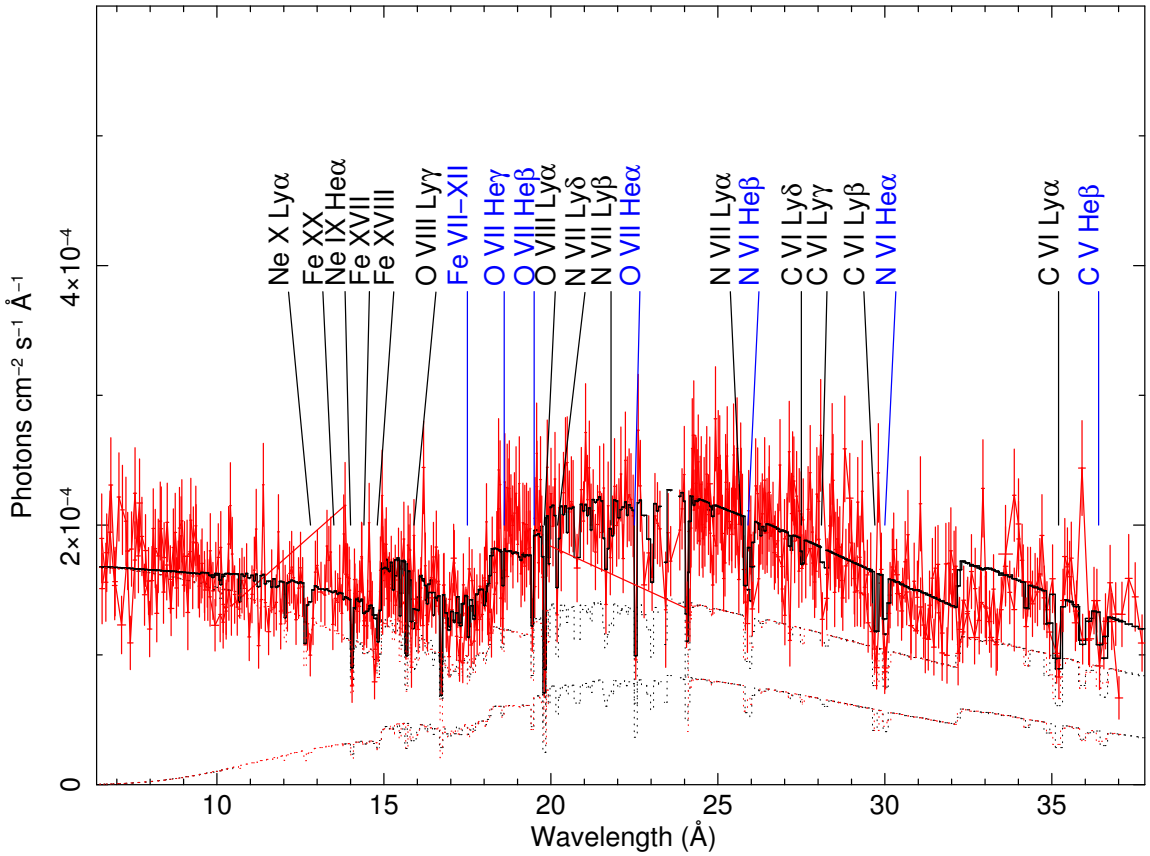

Figure 18: RGS Spectrum. Lines labeled in blue are from the high ionization phase gas. Those labeled in black are the low ionization phase.

is based on a feature seen in the MOS spectra, see Section 5.4. With the continuum set, emission lines are searched for. There are no major emission features for these data in the soft spectrum of IRAS F12397+3333.

Next, absorption features are searched for. There is a notable broad absorption trough between 15.5 Å and 17 Å. The red edge of this trove has a redshift corrected value of 17.66 Å (0.70 keV). This feature is consistent with the Unresolved Transition Array (UTA) of Fe VII-XII, as in IRAS 13349+2438 (Sako et al., 2001) and Mrk 766 (Sako et al., 2003) and described by Behar et al. (2001). As noted by Sako et al. 2001

in their analysis of IRAS 13349+2438, this red edge is inconsistent with the O VII edge at 16.78 Å. However, there is also an edge at 14.21 Å, which is the O VIII edge.

IRAS F12397+3333 exhibits a large number of absorption lines, see Figure 18. Most of these are due to H and He like C, N, O and Ne with some L-shell Fe XVII-XX and M-shell Fe VII-XII contributing. In order to simulate dust, neutral absorption edges for C, N, O and Fe LII were added. Initially the absorption lines are fit as Gaussian absorption lines. All the lines will have the same line width, as the statistical quality of the RGS data is unable to constrain each individual line. This is done with the knowledge that each ion could have a different turbulent velocity. Once the individual lines are known, their energy values are linked together. Using the knowledge of cross sections from Verner et al. (1996), the optical depth for each of the lines was calculated and linked to each ion. The model was then fit to each ion. Once a statistically acceptable fit was obtained, each ion energy and optical depth error were measured. A list of ion column densities can be found in Table 3. The best fit value of the FWHM turbulent velocity is 519 $\pm$ 109 km s^{-1}. A bulk flow velocity shift of -178 km s^{-1} was noted.

As noted by Sako et al. (2001) for IRAS 13349+2438, there is detection of Fe VII-XII and Fe VIII-XX, indicative of two distinct absorber regions. The data set is then refit with this assumption. The C V, N VI, O VII and Fe VII-XII are treated as one group, consisting of a low ionization phase (LIP), whereas C VI, N VII, O VIII, Ne IX, Ne X and Fe XVII-XX are treated as the other group, forming a high

Table 3: List of ions, column densities, changes to χ^2 and type of gas phase.

Ion	$N_i(cm^{-2})$	$\Delta\chi^2$	Component
C V	$(2.1^{+2.9}_{-1.3})\ 10^{15}$	19.0	low
C VI	$(1.6^{+1.7}_{-1.0})\ 10^{15}$	32.3	high
N VI	$(2.8^{+2.3}_{-1.1})\ 10^{15}$	37.7	low
N VII	$(5.8^{+5.1}_{-2.8})\ 10^{15}$	1.35	high
O VII	$(7.5^{+5.0}_{-2.8})\ 10^{15}$	1.5	low
O VIII	$(1.2^{+2.0}_{-0.6})\ 10^{16}$	7.3	high
Ne IX	$(1.9^{+4.2}_{-1.2})\ 10^{16}$	26.8	high
Ne X	$(1.0^{+1.8}_{-0.6})\ 10^{17}$	18.7	high
Fe XVII	$(7.1^{+11}_{-5.0})\ 10^{15}$	11.3	high
Fe XVIII	$(6.6^{+11}_{-4.2})\ 10^{15}$	18.75	high
Fe XX	$(5.4^{+5.4}_{-5.4})\ 10^{18}$	6.0	high
Fe VII	$(1.0^{+1.6}_{-0.7})\ 10^{16}$	23.5	low
Fe VIII	$(8.5^{+15}_{-6.2})\ 10^{15}$	18.32	low
Fe IX	$(3.6^{+7.2}_{-2.7})\ 10^{16}$	32.0	low
Fe XI	$(1.4^{+1.9}_{-1.1})\ 10^{16}$	17.3	low
Fe XII	$(3.0^{+4.7}_{-2.1})\ 10^{16}$	25.6	low

ionization phase (HIP). The data were refit under the assumption that the HIP and LIP might have two discrete velocities. The turbulent velocities of each group are not statistically different from the previous fit and are both about 500 km s^{-1}. The bulk flow velocities are 37 km s^{-1} for the LIP and -393 km s^{-1} for the HIP.

There are several notable differences between the warm absorber spectrum of IRAS F12397+3333 and that of IRAS 13349+2438. First, in the former the O VIII line at 18.96 Å is much more prominent than that of the N VII at 24.78 Å and is the most prominent. A couple of the absorptions that Sako et al. (2001) notes in IRAS 13349+2438 are absent in IRAS F12397+3333. These are C VI at 26.36 Å, N VII at 20.91 Å and 19.83 Å and Fe XVII at 15.10 Å. The C VI at 26.36 Å is one of the weakest features seen in IRAS 13349+2438, so a minor difference in column densities,

ionization parameter, abundances, etc. could render this feature void. The absence of N VII at 19.83 Å is due to a chip gap in RGS 1 and the loss of CCD 4 in RGS 2. RGS 1 exhibits a chip gap precisely at energies that would correspond to where a redshifted N VII at 19.83 Å would be. The loss of the RGS 2 unit for these same energies means the data are lost. The Fe XVII line at 15.10 Å is also a weak feature and could be lost for the same reasons as the C VI line. However, it is also very close to the UTA of M-shell Fe, so it could additionally be lost there. Finally, there is N VII at 20.91 Å. The absence of this line is very mysterious and difficult to explain. This shall be elaborated on more.

In addition to the absorption lines that are absent, there are a few lines not seen in IRAS 13349+2438. These are O VII at 18.63 Å and N VII at 19.36 Å. N VII at 19.36 Å is very odd, given that there is no N VII at 20.91 Å seen. One would predict that if there is substantial absorption from N VII at 19.36 Å, there should be a deeper line at 20.91 Å. Next, there is an O VII line at 18.63 Å. As the O VII line at 21.60 Å is much deeper than reported by Sako et al. (2001), this is not surprising.

A few more minor differences are that Sako et al. (2001) notes a discrepancy at 29.3 Å between their model and the data, which they attribute to an absorption edge of N V. No such discrepancy is seen in IRAS F12397+3333. Also, there are also additional features at 29.1 Å and 29.5 Å. The second is likely due to N V at 29.46 Å. The first remains unidentified.

The photoionization code XSTAR, as last described by Kallman (2010), was then used to calculate the ionization parameter and equivalent hydrogen column densities. For the ionization parameter of $\xi = \frac{L}{nr^2}$, Tarter et al. (1969) is used here. Based on the Behar et al. (2001) work on the UTA Fe, an ionization parameter of $\log \xi < 1$ and equivalent hydrogen column density at around 10^{21} cm^{-2} are used to calculate the LIP cloud. The range of parameters are $\log \xi = -0.84 \pm 0.10$ and $\log n_{\rm H} = 21.38 \pm 0.04$. As in Sako et al. (2001) non-solar abundances of C, N, O, and Ne were needed relative to Fe. For the LIP gas a factor of three lower O abundance needed. And for the HIP gas a factor of 2 lower C and N abundances were needed and 25 percent higher abundance of O and Ne. The LIP gas contributes not only to the UTA Fe, but is also the dominant source of the He-like C, N and O. Based on the soft X-Ray luminosity, L = 3.05 x 10^{43} erg s^{-1}, the radial location of the LIP gas can be constrained with an upper limit. The equivalent hydrogen column density can be expressed as $n_{\rm H} = n\Delta r$, where n is the density of the cloud and Δr is its radial thickness. Assuming that radial thickness is less than r, $\Delta r/r < 1$, r can be shown to be less than 5.88 x 10^{21} cm or 1.91 kpc.

The HIP gas is the dominant source of the H-like C, N, O and Ne, He-like Ne and L-shell Fe. The ranges of parameters are $\log \xi = 1.88 \pm 0.03$ and $\log n_{\rm H} = 21.08 \pm 0.11$. Again using the soft X-Ray luminosity and assumption that $\Delta r/r < 1$, an upper limit on the radial location of the HIP gas can be calculated. This time it is a value of less

than 4.53 x 10^{20} cm or 147 pc. This value is consistent with that of the narrow-line region and that of the turbulent velocities.

5.6. Discussion

IRAS F12397+3333's warm absorber spectrum shares many characteristics with other dusty warm absorbers, such as IRAS 13349+2438 (Sako et al., 2001) and Mrk 766 (Sako et al., 2003). Although IRAS F12397+3333 has a few minor differences from IRAS 13349+2438, the two sources share most of their major characteristics.

All calculations using XSTAR indicate that there should be a substantial C V absorption line at 40.27 Å. Although 40.27 Å is outside RGS's range, it is within the range of the lower spectral range of EPIC. Given how large an optical depth XSTAR predicts for C V, this line should be observable by EPIC if present. At IRAS F12397+3333's redshift, this line should be at 0.295 keV. No compelling evidence of such an absorption can be found in either EPIC pn or EPIC MOS. This leads to the conclusion that either the prediction of C V at 40.27 Å is wrong or EPIC is unable to see it. As C V at 34.97 has already been observed in the RGS spectrum, it is unlikely that the C V line at 40.27 Å is truly absent. Poor calibration of EPIC for energies below 0.3 keV may prevent the detection of the feature with EPIC. Another possible reason is that the poorer spectral resolution combined with a smaller optical depth that is predicted also will prevent such a detection.

Future observations of IRAS F12397+3333 might look to target the source when it is in a brighter phase to see how the warm absorber material is affected by source illumination. As there is only one XMM-Newton observation of IRAS F12397+3333, discussion of variability of the warm absorber is inappropriate at this time. A second observation could be useful in determining if or how the warm absorber changes over time. An observation made during another phase might also be useful to determine the type of variability with a flux-flux plot. A Chandra observation with the Low Energy Transmission Grating could likely determine the presence of the C V at 40.27 Å absorption line.

Also of interest is the slight softness seen in the hard ratio plot in Figure 16a. A similar set of features were found in Mrk 766. The flares appear to be an independent spectral component. They are hypothesised to be the result of a hot spot on the accretion disk. See Chapter 6 for the full discussion on this topic. If a similar scenario applies to IRAS F12397+3333, it is purely speculative at this point. The flare is too short and too small for full analysis it. It should be noted as a candidate soft flare and possibly looked for in future observations.

5.7. Conclusion

The spectrum of IRAS F12397+3333 was fit with a power law, a soft excess component, a low flux Fe Kα and Fe edge. All of this was covered by a two phase warm absorber. The soft excess was found to be most likely a blurred ionized reflection with

a low ionization parameter and moderate blurring. The variability was shown to be caused by a change in the power law flux. A large number of narrow absorption lines were found in the RGS spectrum, which supports the two phase gas cloud. Assuming a small Δr, radial thickness, the upper limit of the location of the high ionization phase was shown to be consistent with the location of the narrow-line region. Over all this source shows a great deal of similarity to IRAS 13349+2438.

MARKARIAN 766

6.1. Introduction

Mrk 766 is a low redshift (z=0.012929) narrow-line Seyfert 1 (NLS1) galaxy. The luminosity is typical for that of a NLS1, on the order of 10^{43} ergs/sec. Mrk 766 is a bright AGN in the 0.5-2.0 keV X-Ray band, with flux $\sim 10^{-11}$ ergs s^{-1} cm^{-2} (Leighly et al., 1996), and observed through a low Galactic column density, $\sim 1.8 \times 10^{20}$ cm^{-2} (Murphy et al., 1996), which makes this a commonly studied object.

Mrk 766 is a commonly observed NLS1 in all bands. In the X-Ray band Mrk 766 is a typical NLS1, exhibiting a strong soft excess below 2.0 keV and Fe Kα line. There is also the presence of a warm absorber since there is a significant absorption feature near 0.74 keV. However, the short term variability is much more rapid than galaxies of this class, changing by a factor of two in brightness in approximately 10 ksec.

To date XMM-Newton has observed Mrk 766 eight times since its launch in December of 1999. Once in 2000 in Rev 82 for 58 ksec, once in 2001 in Rev 265 for 136 ksec and six times in 2005 during Rev 999-1004. Page et al. (2001) initially described Rev 82. They looked at the spectrum between 2.0-12.0 keV and described it as a power law plus broad Fe line. The variability was characterised as a change of flux in a power law superimposed atop of a less variable low energy emission mechanism. For Rev 265 Pounds et al. (2003) focused on the Fe line . They noted the shape of the observed line was likely due to a broadened highly ionized line, but

not relativistically broadened, and a narrow neutral line. They also linked variation of the line strength to X-Ray flares. Vaughan & Fabian (2003) and Vaughan et al. (2003a) analyzed the timing characteristics of Rev 265. In their power spectrum analysis of Rev 265, Vaughan & Fabian (2003) note a high frequency break in the power spectrum and low coherence between different energy bands. A break in the power spectrum is a well known feature of the galactic black hole candidate Cygnus X-1. From this similarity Mrk 766 is inferred to be possibly radiating above the Eddington limit. And the low coherence could be interpreted as rapid variability in the corona. Vaughan et al. (2003a) discovered a linear relationship between the fractional variability and flux of Rev 265. Miller et al. (2006), using Rev 82, 265 and 999-1004, have shown the ionized Fe line to be highly variable and likely originating from an ionized reflection and occurring within a few AU of the central black hole. Miller et al. (2007) and Turner et al. (2007), again using Rev 82, 265 and 999-1004, proposed two models: a partial covering model and a scattering model to explain the high variability. Markowitz et al. (2007) calculated an RMS spectrum and power spectra for Rev 265 and Rev 999-1004 and found an energy dependency on the high frequency break. They claim to have found a time lag between the soft and hard bands.

The RGS has been studied by Branduardi-Raymont et al. (2001) and Sako et al. (2003) for Rev 82 and Mason et al. (2003) for Rev 265. Branduardi-Raymont et al.

(2001) presented evidence that the shape of the spectrum was caused by relativistically broadened emission lines. Sako et al. (2003) reevaluated Rev 82 and Mason et al. (2003) used Rev 265 to test a proposed dusty warm absorber model and the relativistically broadened emission line model. They both found the relativistically broadened emission line model to be the superior explanation.

In this work the dynamical spectral analysis is used to explore the dynamical behavior of Mrk 766. Several important and previously unrecognized properties were found. These included the phenomenon of 'soft flaring' and a distinct two branches in the flux-flux plots. These previously unrecognized features are key to understanding the dynamics of the whole X-Ray spectrum. Data from the EPIC and RGS instruments were used in these findings.

6.2. Data Reduction

The operation modes of EPIC during the eight observations were as follows. All observations were made with EPIC pn in small window mode with medium filter and EPIC MOS1 and MOS2 in large window mode with medium filter. The observation from Rev 265 was made with MOS2 in small window mode and MOS1 in flare monitor mode. RGS was in use for all observations.

The data were reduced in the manner described in Section 3.9 of Chapter 3. The version of SAS used was 9.0.0. After data reduction, analysis began by checking for and removal of background flares. From a total observation time of 688 ksec, 590

ksec was deemed usable. While many of the observations had significant background flaring near the end of the observation, Rev 1003 and 1004 suffered the most and have the most dramatic cuts due to background flaring.

The source region corresponds to a circle 45 arcsec in radius and the background is of the same size, from an empty region of the same chip. The MOS2 background from Rev 265 was taken from an annulus of the other MOS2 chip and not the central chip because of the small window operation mode.

6.3. Lightcurve

Lightcurves were extracted for the energy band of 0.3-12.0 keV. These were then all plotted on the same scale in Figure 19 to give a global view of the total variability and then individually in Figure 20 to understand each individual observation. It should be noted that Rev 999-1004 are one continuous observation with gaps to allow XMM-Newton to orbit the Earth and return to a safe viewable location. Rev 265 clearly has the highest flux level and is the most violently variable of the eight observations. It shows changes of 50% in count rate on the order of 10 ksec. Rev 999 is the quietest, showing only minor changes over the duration of the 90 ksec observation, but a similar increase of 50% from its lowest to highest count rate in 10 ksec. Rev 1000 starts out by being quite like Rev 999 but shows a rapid change and goes on to being quite variable. Rev 1001-1003 continued in this same pattern as set by Rev 1000. They vary at a slightly higher flux level than Rev 1000, but less than

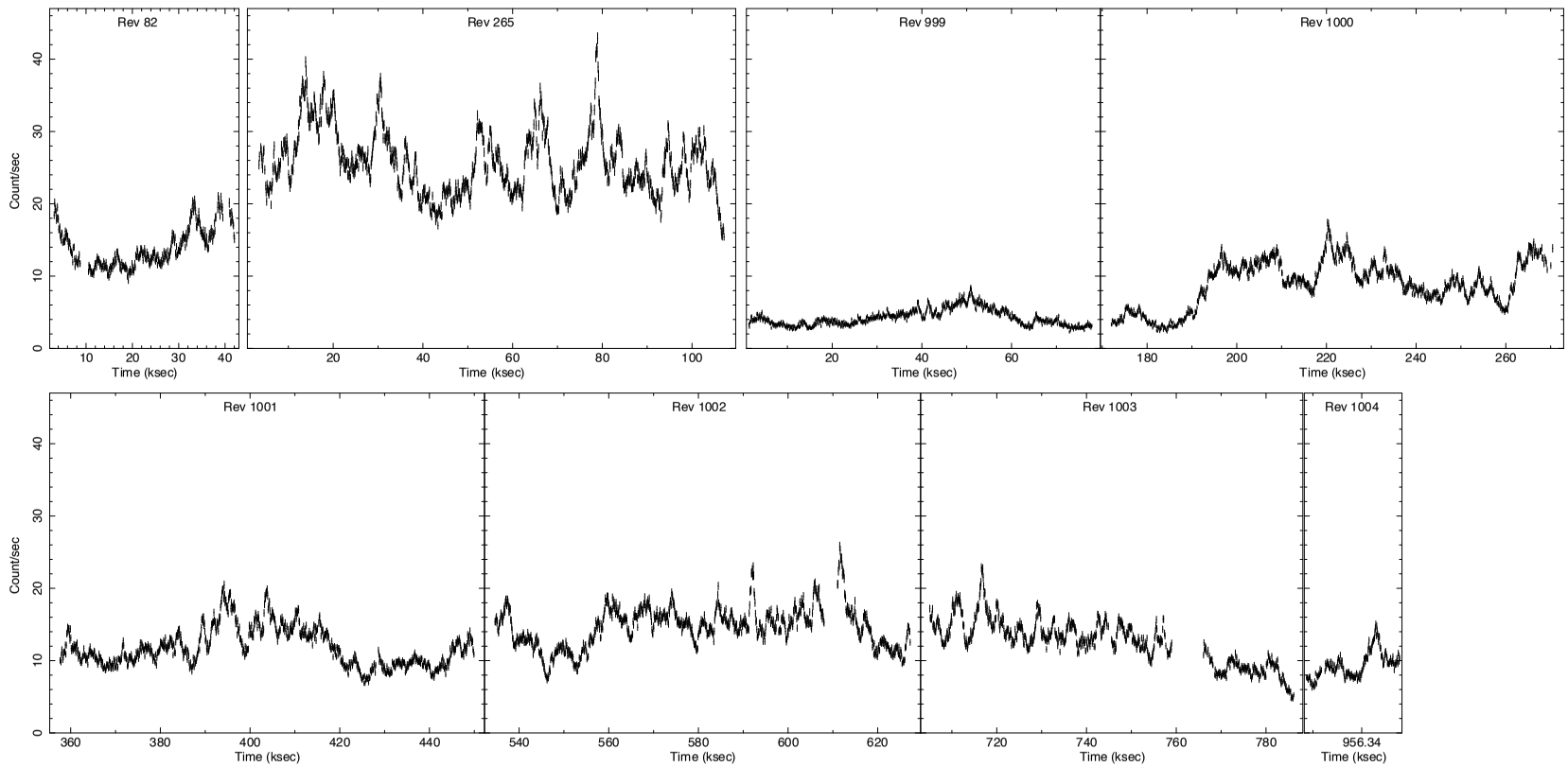

Figure 19: EPIC pn lightcurves. All lightcurves are binned at 100 ksec and are scaled to the same size. Rev 999-1004 basically form one continuous observation. Rev 265 is the brightest of eight, with its lowest phases being the same as the high phases from the other observations, except for Rev 999. Rev 999 is the lowest flux state and shows little temporal variability. The early part of Rev 1000 shows behavior similar to Rev 999 before transitioning back to the average as seen in Rev 82 and Rev 1001-1004.

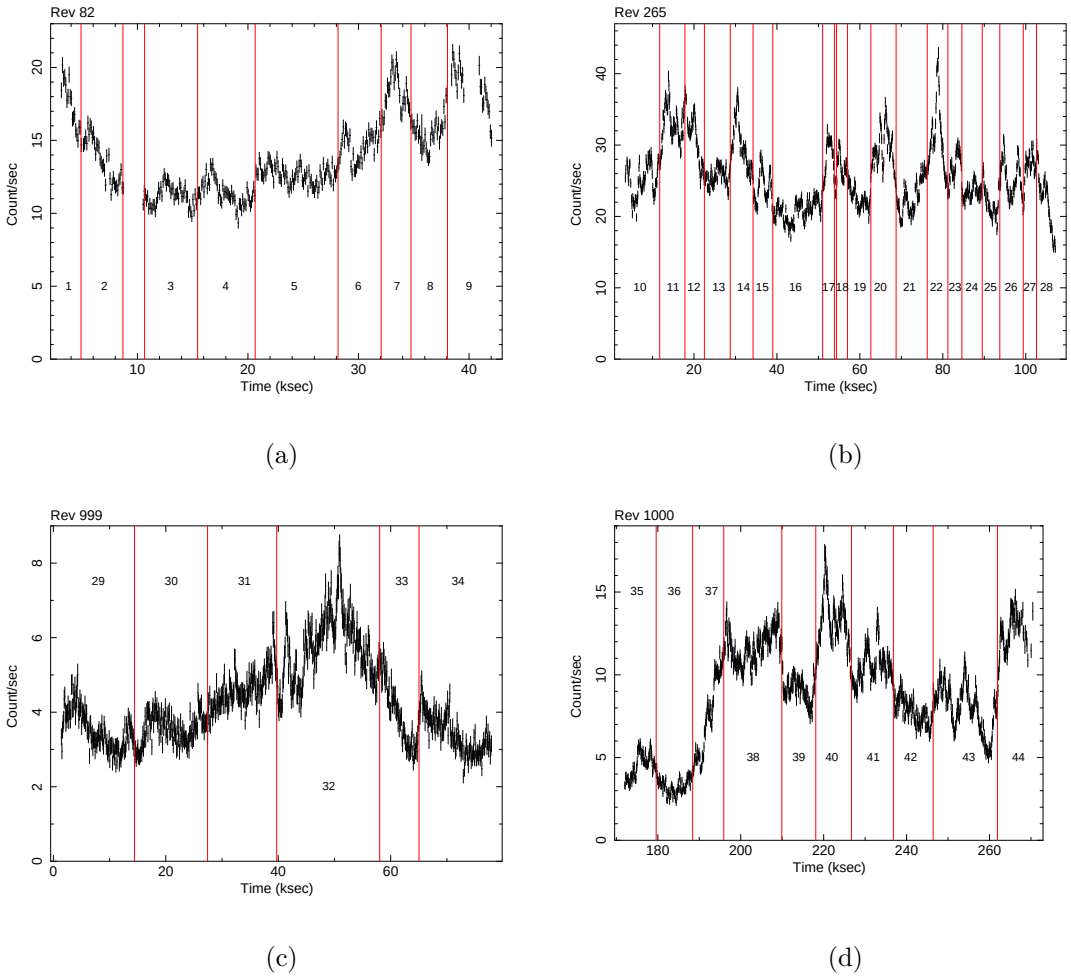

Figure 20: Each lightcurve was cut into regions. The regions are based on the lightcurves and hardness plots. Each region is then numbered so it each has a unique identity. The regions are not of uniform size, but a minimum of 2 ksec. Plots are not on the same scale.

Figure 20 – Continued

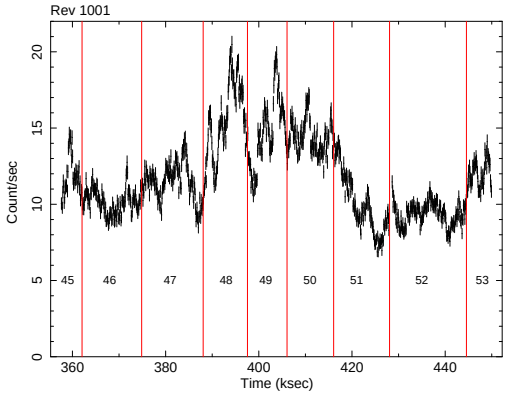

(e)

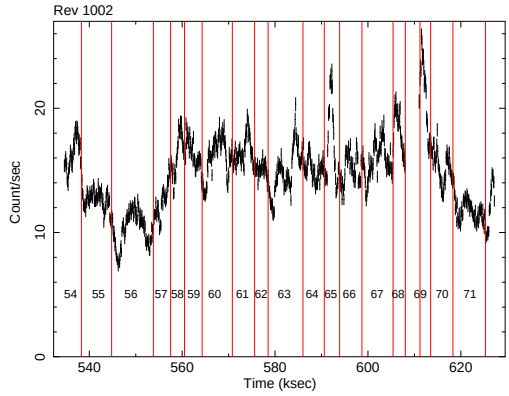

(f)

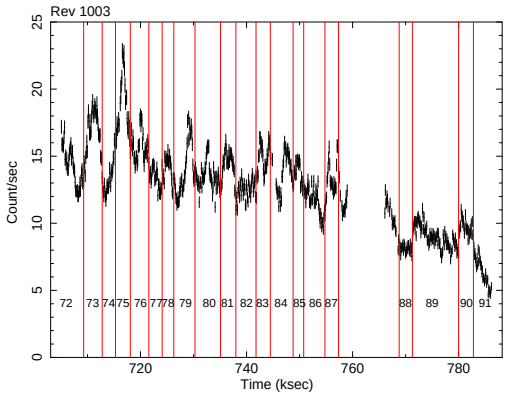

(g)

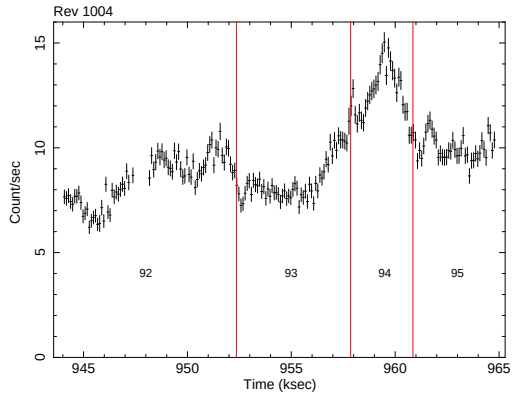

(h)

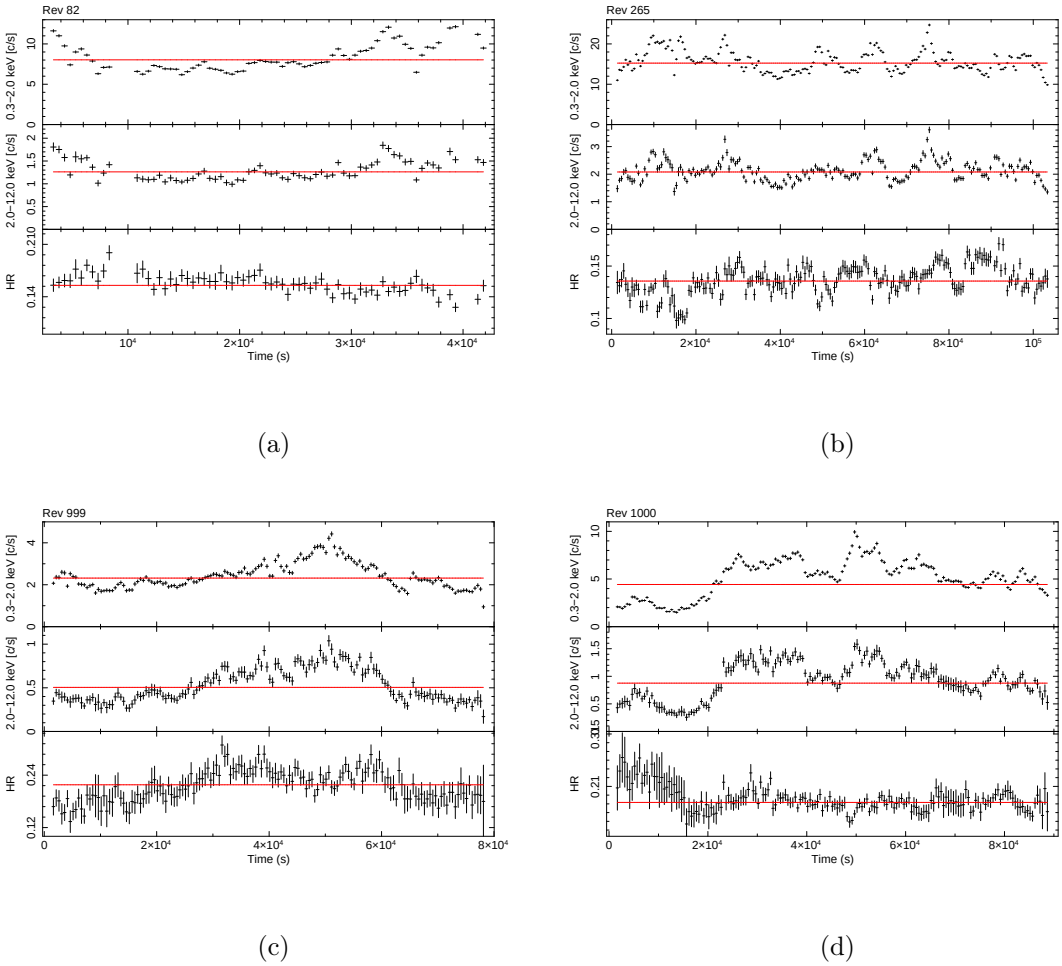

Figure 21: Hardness ratio plots. Lightcurves for all eight observations are filtered in a soft band, 0.3-2.0 keV, and a hard band, 2.0-12.0 keV, and the ratio of the hard band to the soft band. Note the larger hardness ratio of Rev 999 and the early part of Rev 1000. Also the dips in the hardness ratio of Rev 265 are notable.

Figure 21 – Continued

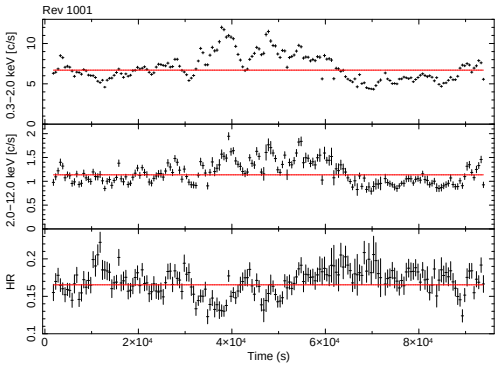

(e)

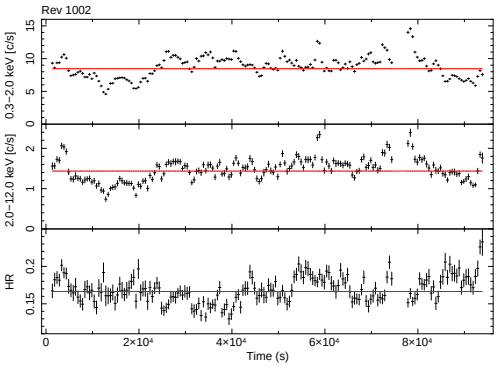

(f)

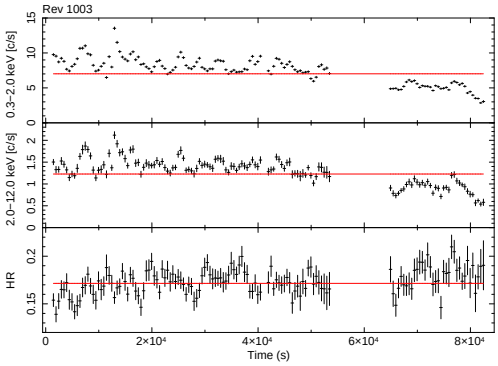

(g)

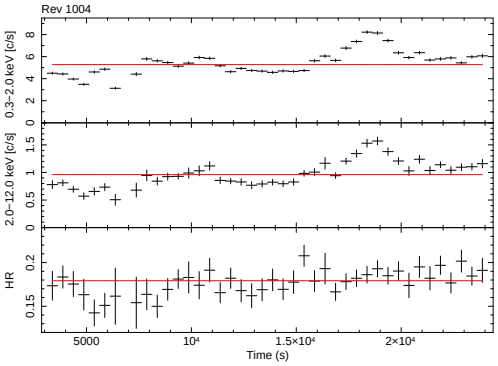

(h)

Rev 265. The time scale of variation is about the same, 10 ksec. Rev 1004 shows a decrease in flux, but not a return to the quiet nature of Rev 999.

Various energy filtered lightcurves were made and compared to each other in hardness plots. Figure 21 shows a single selection of energy bands, 0.3-2.0 keV for the soft X-Ray band and 2.0-12.0 keV for the hard X-Ray band. The hardness ratio is a ratio of a higher energy band, a hard X-Ray band, to a lower energy band, a soft X-Ray band. When this ratio is greater than the average the source is hardening and when the ratio is less than the average, it is softening. The bands shown here were selected to emphasize a particular set of features.

The emphasized feature seen here in the hardness ratio occurs in Rev 265, Figure 21b. This observation has a couple of periods of large softening. There is a large softening at around 1.8 x 10^4 sec and again near 5 x 10^4 sec. The softening near 5 x 10^4 sec is particularly interesting since in the 2.0-12.0 keV filtered lightcurve absolutely no flaring can be seen. But in the 0.3-2.0 keV filtered lightcurve there is clearly a pair of flares. Careful examination of the feature near 1.8 x 10^4 sec also reveals a flare only in the soft band and none in the hard. For this reason, the flares shall be referred to as "soft flares." The other flares, those that have both hard and soft components, shall be referred to as "normal flares." Other observations have periods of softening, but none as clear or obvious as Rev 265. These are candidate soft flares.

The other feature of major importance is the hardness ratio of Rev 999 and Rev 1000. Rev 999 clearly has a larger hardness ratio than any of the other observations. There is also a dramatic change of hardness ratios in Rev 1000, Figure 21d. As noted previously, the early part of Rev 1000 is similar to Rev 999. The start of Rev 1000 has a hardness ratio of 0.22, similar to the hardness ratio of Rev 999. As Rev 1000 transitions into the more average behavior, the hardness ratio drops to 0.14-0.16, a value typical of the other observations. As none of the other observations exhibit this feature, Rev 999 and the beginning of Rev 1000 clearly represents a unique behavior.

Using a combination of the full band lightcurve and hardness ratio plots, the lightcurves were split into regions, see Figure 20. While no upper limit for a time bin was set, a lower limit of 2 ksec was used. The goal of creating so many regions was to group like-behavior together. Variations in different dynamical behavior, such as flaring, dim, constant, hardening or softening, were all taken into consideration. While there are certainly many wrong ways of creating such time regions, there is no one unique right way. There is always a selection bias involved when one chooses. These regions shall be referred back to and will be used for spectral fitting in Section 6.9.

6.4. Flux-flux Plots

In order to explore the variable nature of Mrk 766, several model independent tools will be used, the first of which is the flux-flux plot. Several energy bands were

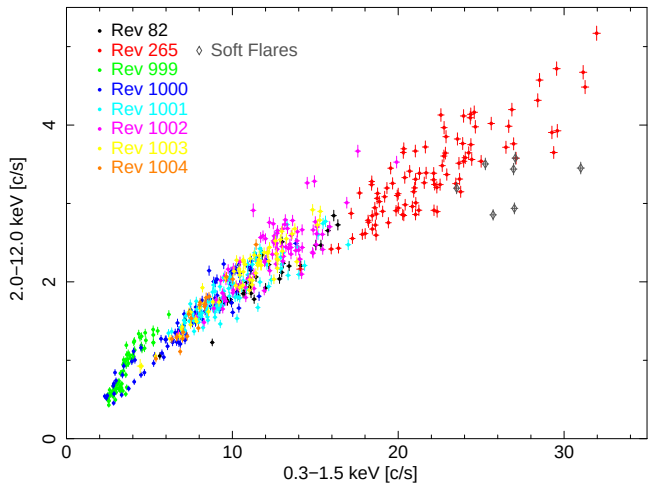

(a)

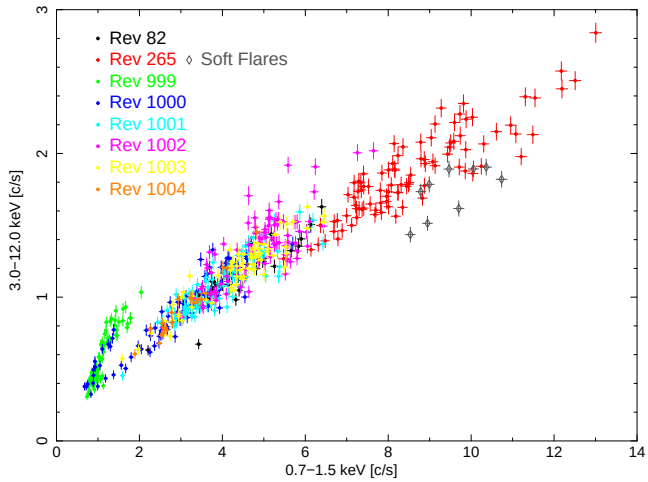

(b)

Figure 22: Flux-flux plots of different energy bands. Figure (a), 0.3-1.5 keV vs. 2.0-12.0 keV shows a wide scatter of Rev 265 (red) points. The soft flares for Rev 265 (gray diamonds) are responsible for much of the scatter. Figure (b), 0.7-1.5 keV vs. 3.0-12.0 keV, exhibits the branching of Rev 999 and part of Rev 1000. Figure (c), 0.3-0.7 keV vs. 0.7-1.5 keV has little scatter and no branching. As this combination forms a linear relationship without a vertical offset the emission mechanism is assumed to be the same for both. Figure (d), 2.0-4.0 vs. 4.0-12.0 keV, is like Figure (c) but now has a vertical offset. This is assumed to be caused by a constant component in the range of 4.0-12.0 keV.

Figure 22 – Continued

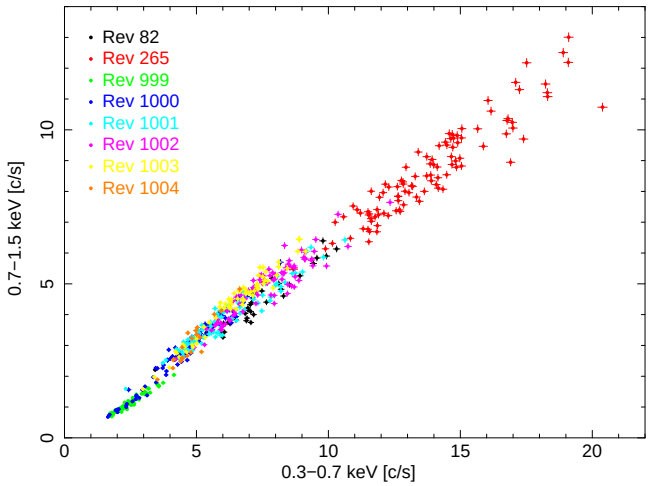

(c)

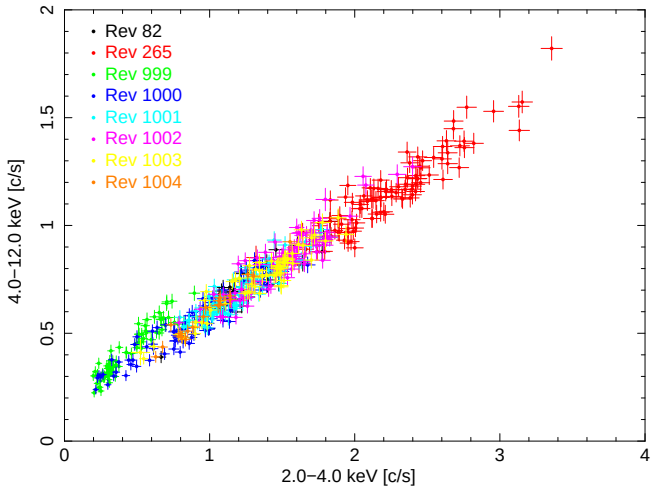

(d)

chosen in making these flux-flux plots. They were chosen to either amplify a given feature or to explore the expected emission mechanism in the spectra. Four flux-flux plots are shown in Figure 22.

The first major feature is the wide scatter of Rev 265. In Figure 22a, Rev 265 has a much wider scatter than other observations. One might be tempted to conclude that the hard and soft bands are uncorrelated for such a scatter to occur. However, such a conclusion is inconsistent with what is generally seen in the lightcurves. As a general rule of thumb, when the soft band increases or decreases the hard band does as well, but not in every case. The three flares, the soft flares, do not follow this trend. They move along the plot only in the horizontal direction. These soft flares have been marked with the dark grey diamonds in Figure 22a. A large amount of scatter comes from those gray diamonds, but not all. There is some softening in the hardness ratio that is not as clearly tied to a soft flare event. The rest of the scatter should be tied to those points. Interestingly these flares form a trend that moves horizontally across the plot rather than diagonally.

The second notable feature of the flux-flux plots is that Rev 999 and part of Rev 1000 seem to form their own distinct region in Figure 22b. There is the side branch of Rev 999 and part of Rev 1000 and the main branch made up of the rest. It should be noted that from the lightcurves and hardness ratio plots of Rev 999 and the early phase of Rev 1000 both were of much lower flux levels and larger hardness ratio than the rest of the observations. The energy band 0.7-1.5 keV vs 3.0-12.0 keV was chosen

to show the greatest visual difference between these branches. The two branches appear to be linear, and when lines are fit to each branch the slopes are different but have the same constant. This is highly suggestive that the two branches have the same constant emission mechanism in the hard band and different soft variable emission mechanism. There is a discontinuity between the side branch and main branch of the flux-flux plot. Rev 1000 evidently has a hook shape to it. When the points in the flux-flux plot are connected in their time series, the early parts of Rev 1000 follow the Rev 999 branch. Rev 1000 later follows the main branch. The crossover between the two branches occurs once near the minimum and hence it is the pivot point. As the slope is flatter in the main, the spectrum should be steeper and softer whereas Rev 999 and the early part of Rev 1000 should be flatter and harder.

6.5. RMS Spectra

The next model independent tool is the Root Mean Square (RMS) spectrum, see Figure 23. The RMS spectrum calculates and measures the amount of relative variability as a function of energy. See Edelson et al. (2002) and Ponti et al. (2004) for details. A RMS spectrum for Rev 1004 was not calculated because of the relative shortness of the observation. For Rev 82, 265 and 1000-1003, a time bin size of 2 ksec was used. The flares vary on a time scale of about 5 ksec. By choosing a time bin size of approximately half, the risk of averaging out variability is decreased. Due to the fact that Rev 999 has a much lower count rate and the fact that it lacks any

large short term variability, it was binned at 4 ksec in order to increase the spectral resolution.

Looking at the seven RMS spectra for the XMM-Newton observations of Mrk 766, what is most notable is how flat most of the RMS spectra are. Rev 82, 265 and 1001-1003 have flat RMS spectra. In an ideal case the RMS spectrum shows which spectral components have the strongest variability. A relatively flat RMS spectrum means that the variability component is dominant over a broad energy range. Such a component is likely the power law component. Not only does the power law contribute across the whole XMM band, it is expected to be highly variable. The low energy and high energy ends of the RMS spectra are slightly lower than the middles, suggesting a constant component is exhibiting a slightly stronger presence in the low and high energy bands than in the middle energy band. This is reminiscent of the case for MGC-6-30-15 (Vaughan & Fabian, 2004).

Rev 999 and 1000 are not flat nor do they have small RMS values. Rev 999, Figure 23c, has a two peak structure with a small peak at 0.63 keV and a larger one at 2.65 keV. Rev 1000, Figure 23d, has a single peak, but also has a higher RMS value. When the early part of Rev 1000 is excluded and the RMS spectrum is recalculated, it clearly flattens out and is at a much lower level, being more comparable to other observations. Therefore the spectral component that causes this shape is clearly only a factor in Rev 999 and the early part of Rev 1000, the lowest flux states.

From the flux-flux plots it is a reasonable assumption to make that the relationship between the soft band and hard band is linear. If the flux of the two bands is assumed to consist of a constant part and variable part a simple relationship between two bands can be derived, see Taylor et al. (2003). The large peaks in the RMS spectra of Rev 999 and 1000 are caused by the variable component being the most dominant spectral component in this energy band, the constant component is weak. In Rev 999 the local minimum near 0.9 keV is caused by a constant component suppressing the variation. As the suppression takes place over roughly the same energy as the maximum branching of the flux-flux plots, 0.7-1.5 keV, these represent the same phenomenon.

6.6. Power Spectrum

Power spectra were calculated for Rev 82, 265 and 999-1003. Rev 1004, like in the case of the RMS spectra, was simply too short to yield a useful result. The power spectra were calculated in the same manner as Vaughan & Fabian (2003) and Markowitz et al. (2007). The lightcurves were first binned in 100 sec bins and the mean flux was subtracted to remove zero-frequency power. Then a standard Discrete Fourier Transform (DFT) was applied to them and binned by the method of Papadakis & Lawrence (1993). This was then normalized to '(rms/mean)^2 Hz^{-1}' units as defined by van der Klis (1997). The results are consistent with that of Vaughan & Fabian (2003) and Markowitz et al. (2007).

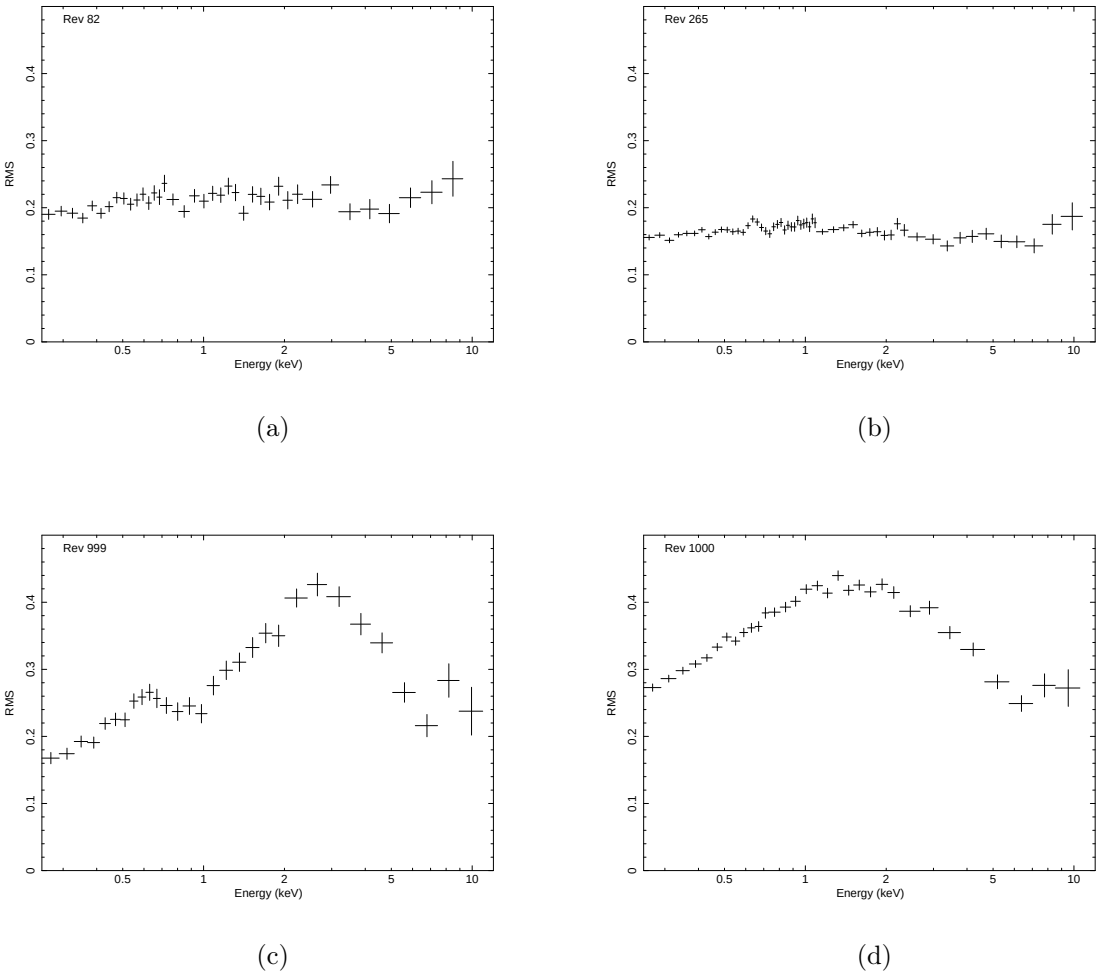

Figure 23: RMS spectra. All but Rev 999 Figure (c), use a 2 ksec time bin to avoid averaging out the rapid variability of these lightcurves. Rev 999 used a 4 ksec to improve the spectral resolution of this low variability observation.

Figure 23 – Continued

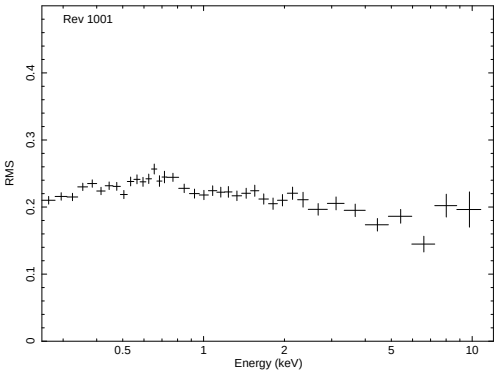

(e)

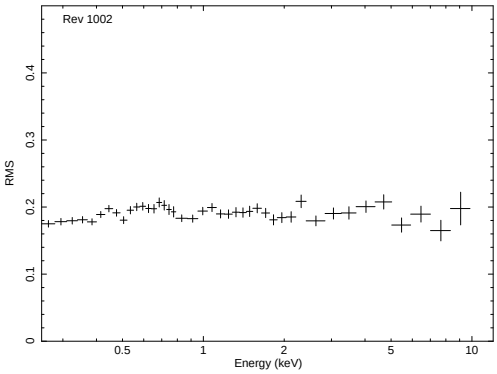

(f)

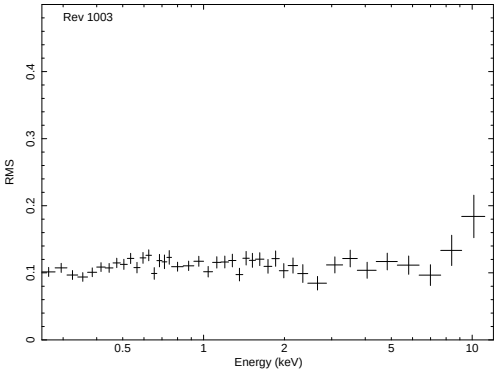

(g)

However based on the flux-flux plots a different set of energy bands were used from those in Vaughan & Fabian (2003) and Markowitz et al. (2007). The four bands used here are: 0.3-12.0 keV (full band), 0.3-0.7 (soft band), 0.7-1.5 keV (medium band) and 3.0-12.0 keV (hard band). Plots of the soft, medium and hard bands are shown in Figure 24. The band choice of Markowitz et al. (2007) is based entirely on statistical reasons and has very little physical justification.

The power spectra were fitted using a Monte Carlo procedure based on what was described in Vaughan et al. (2003b) using the algorithm of Timmer & Koenig (1995) to simulate the synthetic lightcurves. All the power spectra were found to have the shape of a broken power law. The general trend is that the slope is steeper at higher frequencies and flattens out in the low frequencies. As in Vaughan & Fabian (2004) there is an energy dependence of the high-frequency slope, with the soft energy band having a steeper slope and the flatter slope in the hard energy band. Rev 1000 and 1001 show very flat high-frequency slopes, $\alpha_{\rm hi} = 1.9\pm0.4$ and $\alpha_{\rm hi} = 2.0\pm0.5$. Rev 999 exhibits a flatter overall power spectrum, $\alpha_{\rm hi} = 1.60\pm0.5$ and higher frequency break, at $8.8\pm5.0 \times 10^{-4}$ Hz. Energy dependence in the break frequencies was searched for, but the error bars were too large to accurately determine this.

The coherence function of the individual observations was calculated. The results are consistent with Vaughan & Fabian (2003) for Rev 265, where the coherence is quite low. As such searching for time lags between the different energy bands with any legitimate meaning is not feasible.

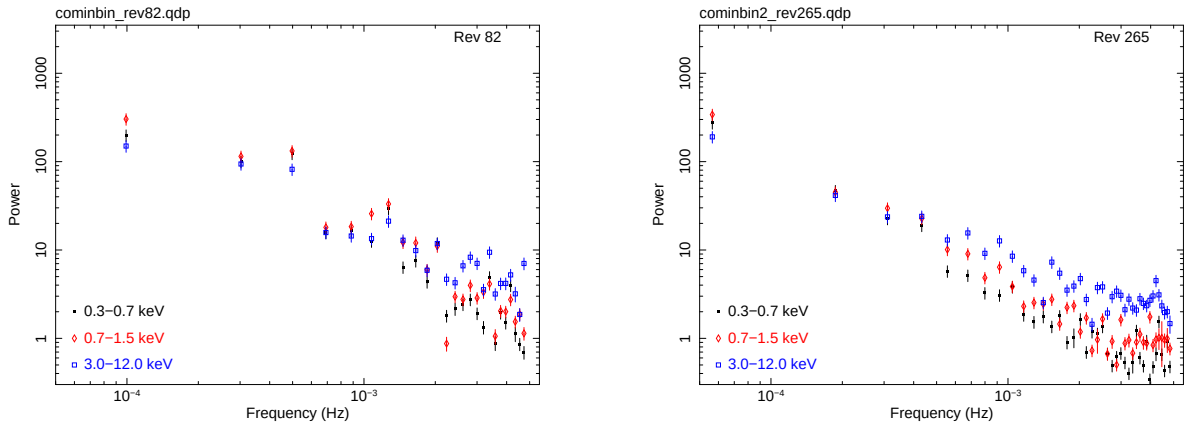

(a)

(b)

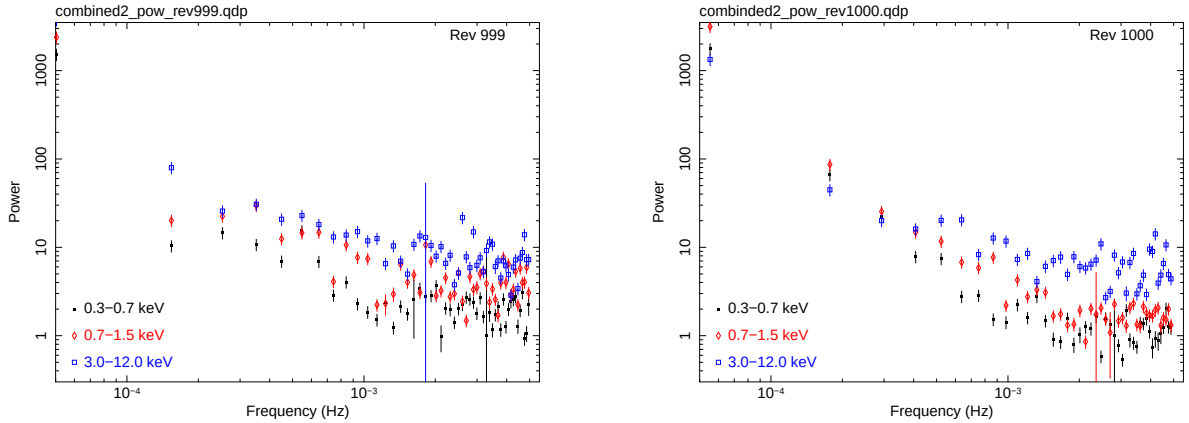

(c) (d)

Figure 24: Power spectra of Rev 82, 265 and 999-1003. Three energy bands are shown: 0.3-0.7 keV in black with closed squares, 0.7-1.5 keV in red with diamonds and 3.0-12.0 keV in blue with open squares.

Figure 24 – Continued

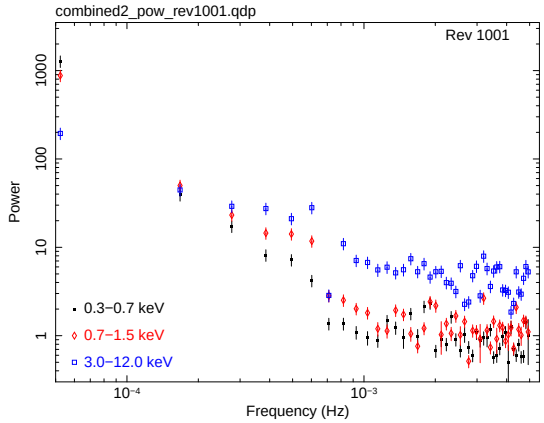

(e)

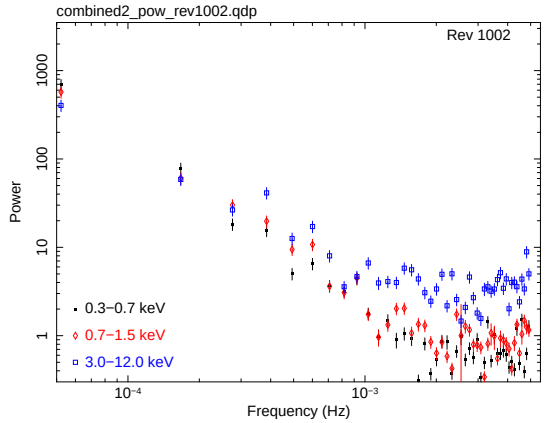

(f)

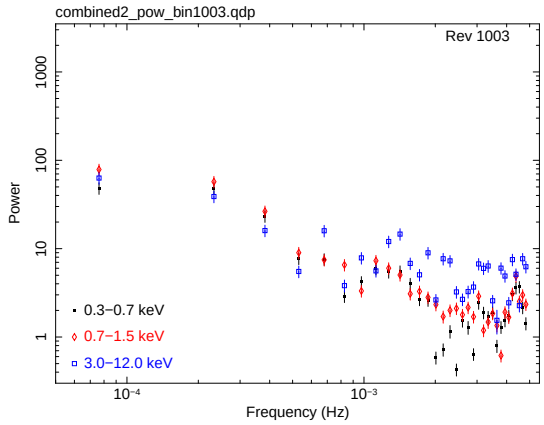

(g)

6.7. Time Averaged Spectrum

6.7.1. Continuum model

The spectral analysis began with the mean spectrum of all eight observations. As the EPIC MOS 1 camera was operated in monitoring mode for Rev 265, only the data from EPIC pn and RGS will be used in this section. The mean spectrum from EPIC pn was created by co-adding the counts of each observation with the FTOOLS program MATHPHA. For the RGS mean spectrum, the SAS task, RGSCOMBINE was used. The response matrix files and auxiliary matrix files were merged with the FTOOLS program ADDRMF and ADDARF. They were weighted based on the usable data generated by each instrument. For a description of the model parameters see Appendix A.

The fitting began with the hard spectrum, 2.0 keV and higher, of the EPIC pn camera. The spectrum between 6.0-7.5 keV is ignored because of its atomic features. A power law and cold absorption are used as the beginning model. The XSPEC model PHABS is used for the cold absorption with a column density of 1.78 x 10^{20} cm^{-2} (Murphy et al., 1996). The power law fit is quite adequate with a photon index of 1.9 and a χ^2 of 147 for 86 degrees of freedom (dof). Next, the region of 6.0-7.5 keV is added back in. It consists of a prominent emission line near 6.4 keV and an absorption edge near 7.1 keV. An edge model was added and the value was found to be 7.17 keV. A single Gaussian line was added and resulted in a value of 6.53 keV. This model is a poor fit. There remains a narrow residual near 6.4 keV. When a second

Gaussian line is added the two line values are 6.4 keV and 6.7 keV. The narrower line at 6.4 keV is the Kα line for neutral or very low ionized Fe and the broader line at 6.7 keV is the Kα line for He like Fe. As the Fe Kα is present, a neutral reflection model is added as well. PEXRAV (Magdziarz & Zdziarski, 1995) in XSPEC is used for this model. Lastly, there are two absorption features at 6.9 keV and 7.14 keV that are modeled with Gaussian absorptions and an additional edge at 8.8 keV.

Given how wide the broader Fe line is, the ionization reflection model, REFLION (Ross & Fabian, 2005) blurred with KDBLUR (Laor, 1991), were used to model both the broad Fe line and soft excess. A super-solar abundance of Fe is needed to produce an Fe line of appropriate strength. The illuminating photon index is tied to the power law's photon index. The ionization parameter and normalization were left as free parameters. For the blurring the disk was fixed at an inclination angle of 35° and an inner and outer radius of 1.24 gravitational radii (r_g) and 400 r_g respectively. The emission index, q, was set to an average value, see Section 6.8.

There are notable absorption features seen near 0.7 keV and 0.54 keV. These were modeled with absorption edges and are due to the effect of the warm absorber. Finally, narrow emission lines were added to the spectrum below 2.0 keV.

6.7.2. Fe Line

Mrk 766 has very unusual Fe Kα lines. It has both a broad line and a narrow line. The narrow line is centered at 6.4 keV and has an unresolved width. The broad line is centered closer to 6.6 keV and has a width of 200 eV. Page et al. (2001) analyzed the

Rev 265 data and concluded that the narrow line is neutral and low ionization phase Fe Kα, and the broad line was highly ionized Fe, mostly He like Fe with a value of 6.7 keV. They also state that the Laor profile does not work to model this line (Page et al., 2001).

All eight XMM-Newton observations were fit from 2.0-12.0 keV with a single power law, excluding the region between 5.5-7.5 keV. This region is where Fe features, including fluorescence lines and absorption edges, occur. Once fitted, the excluded region was brought back in and the ratio of the data to the model was plotted, see Figure 25. One can clearly see the change of shape and energy of line profile with time.

Ross & Fabian (2005) explicitly assume that blurring of the Fe Kα line is tied to the blurring of the soft excess. Under this assumption the emissivity index and other parameters used in the RGS data fit were fit to the broad Fe line with a Laor profile. Leaving the energy and normalization as the free parameters, a Laor profile was fit to each of the eight observations, see Table 4. The results are a line energy that starts out as near neutral when the source is in low flux state and moves to a more ionized value as the source flux increases. In Rev 999 the broad Fe line is nearly neutral or low ionized Fe. As the source brightens in Rev 1000 this Fe begins to be ionized more and the line energy shifts to reflect this change. Once the source levels off in Rev 1001 the ionization reaches a saturation point and the energy is consistent with the earlier observations.

Table 4: Fe lines table. Line energies, flux in the line and equivalent widths are give for each observation

Rev	Energy (Narrow line)[a]	Flux[b]	EW[c]
82	$6.44^{+0.03}_{-0.03}$	$0.94^{+0.34}_{-0.30}$	< 69
265	$6.43^{+0.05}_{-0.04}$	$0.81^{+0.20}_{-0.20}$	26^{+17}_{-19}
999	$6.45^{+0.03}_{-0.03}$	$0.53^{+0.15}_{-0.16}$	< 52
1000	$6.41^{+0.03}_{-0.02}$	$0.67^{+0.15}_{-0.15}$	33^{+28}_{-28}
1001	$6.43^{+0.04}_{-0.03}$	$0.46^{+0.17}_{-0.17}$	< 41
1002	$6.41^{+0.03}_{-0.03}$	$0.55^{+0.18}_{-0.17}$	< 38
1003	$6.44^{+0.06}_{-0.07}$	$0.42^{+0.19}_{-0.18}$	< 43
1004	$6.50^{+0.08}_{-0.08}$	$0.55^{+0.36}_{-0.34}$	< 95
Rev	Energy (Board line)[a]	Flux[b]	EW[c]
82	$6.66^{+0.27}_{-0.21}$	$4.70^{+1.66}_{-1.59}$	454^{+251}_{-445}
265	$6.62^{+0.36}_{-0.13}$	$5.52^{+1.03}_{-1.14}$	292^{+110}_{-123}
999	$6.42^{+0.17}_{-0.17}$	$2.30^{+0.97}_{-0.96}$	1130^{+274}_{-324}
1000	$6.40^{+0.21}_{-0.17}$	$3.28^{+0.93}_{-0.92}$	455^{+182}_{-159}
1001	$6.68^{+0.53}_{-0.51}$	$1.80^{+0.81}_{-0.96}$	296^{+181}_{-182}
1002	$6.63^{+0.12}_{-0.10}$	$4.62^{+0.88}_{-0.88}$	331^{+170}_{-164}
1003	$6.54^{+0.28}_{-0.21}$	$1.69^{+0.99}_{-0.10}$	198^{+136}_{-132}
1004	$6.50^{+0.73}_{-0.25}$	$4.72^{+1.80}_{-1.85}$	< 677

Notes. [a] Line energy in units of keV. [b] Flux in line, with units of photons cm^{-2} sec^{-1}. [c] Equivalent width in units of eV.

The narrow Fe line stays fairly constant. The line energies, while never exactly 6.4 keV for most of the observations, are within the error limit. Only Rev 1004 is slightly outside. But given the poor statistics of Rev 1004 in general and the fact that it is within the error bars of the other observations, a value of 6.5±0.8 keV is acceptable. The line flux is higher in the earlier two observations but nearly constant in the 2005 observations. Since this line is presumed to have been generated farther out than the broad line, minor long term changes are expected, but should not be seen in shorter time scales.

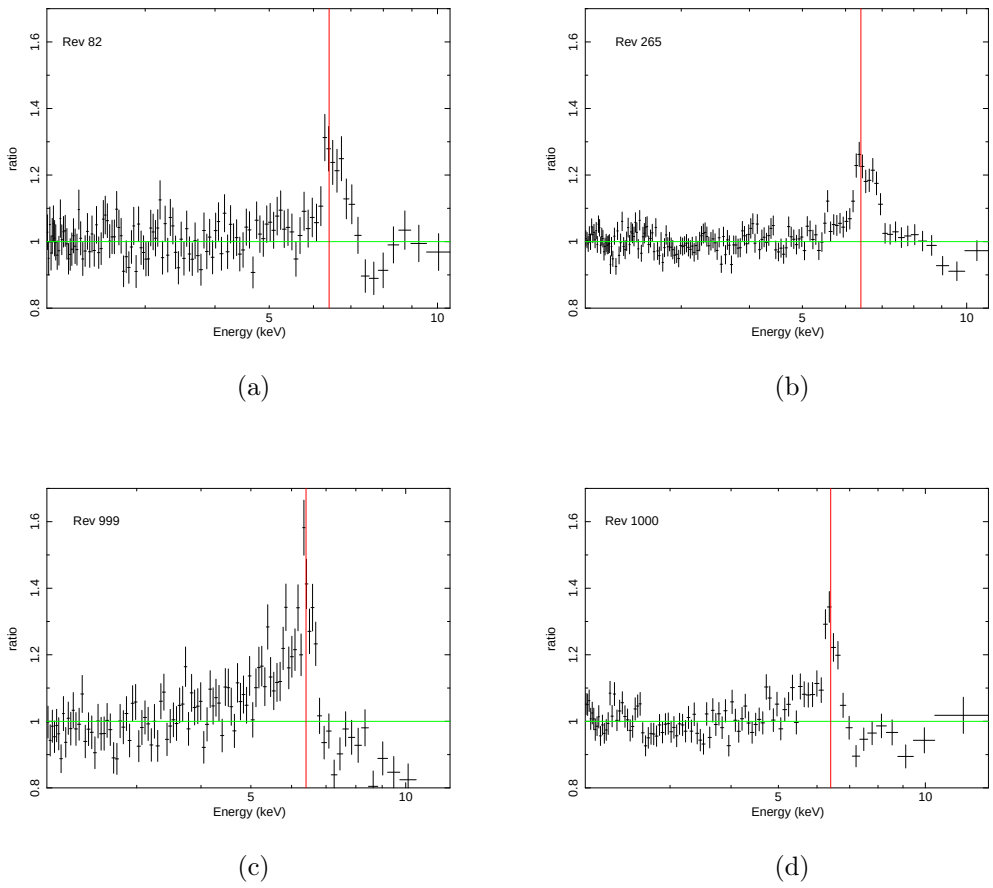

Figure 25: Data/model ratios for Fe line profiles. A power law continuum with galactic absorption was fit from 2.0-12.0 keV, excluding the region between 5.5-7.5 keV. The red vertical line represents the rest-frame energy of 6.4 keV, the Kα fluorescence line for neutral Fe.

Figure 25 – Continued

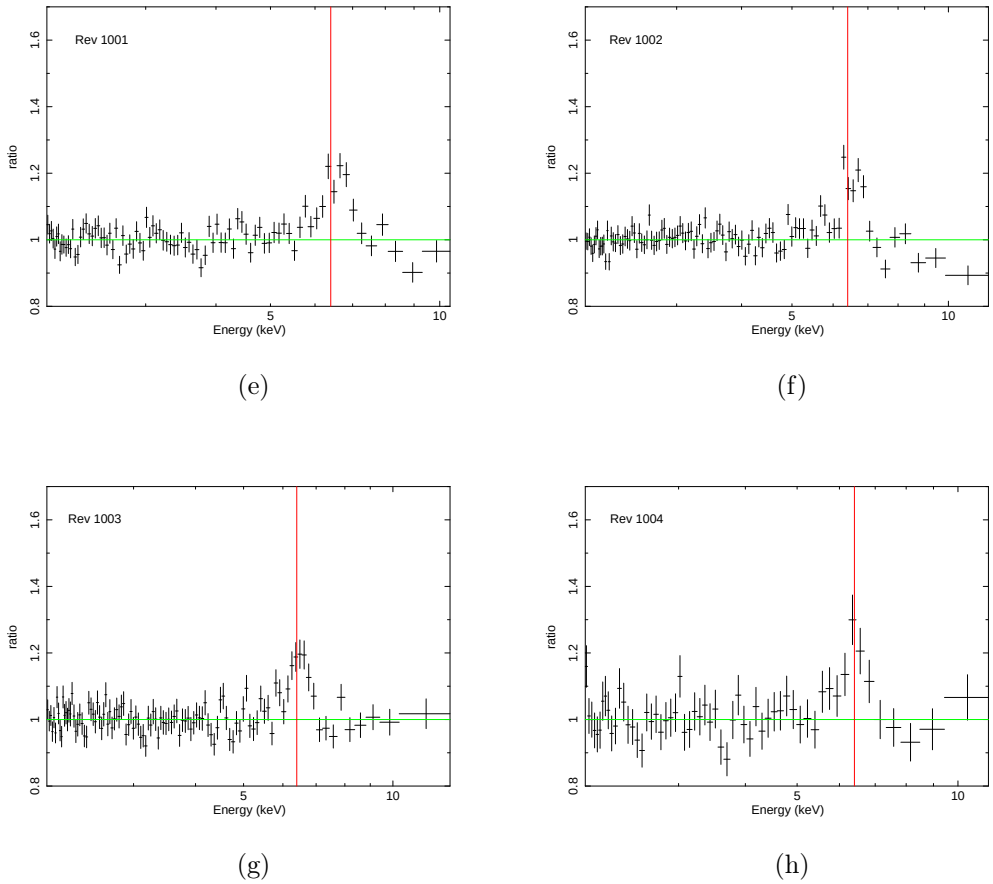

6.8. RGS Data

The RGS shows a pronounced shape. Described by many authors as saw toothed, it consists of three peaks near 18.5 Å, 22.5 Å and 36.5 Å, see Figure 26. Branduardi-Raymont et al. (2001) first proposed that this shape was caused by relativistically broadened emission lines. Lee et al. (2001), using Chandra data for MGC-6-30-15, claimed a dusty warm absorber was the cause. Sako et al. (2003) reanalyzed the Rev 82 data and Mason et al. (2003) analyzed the Rev 265 data testing the two models.

Both concluded the relativistically broadened emission line model was the better fit and a physically superior model. For the dusty warm absorber model such a large optical depth was needed to achieve the correct shape that it was deemed unphysical by both Sako et al. (2003) and Mason et al. (2003). Given that the ionized reflector model of Ross & Fabian (2005) has gained much traction in recent years, the view of Sako et al. (2003) and Mason et al. (2003) will be adopted here.

RGS data for Rev 82, 265 and 999-1003 were analyzed here. The seven observations were merged into a single data set. The narrow features are shown in Figure 27. Rev 1004 does not have enough usable data to analyze the RGS. The observation is too short and with too low a count rate. Rev 999 is marginally usable. The low count rate of this observation makes the analysis difficult. The other observations are free of this type of problem.

To begin with, a basic model is a power law with Γ frozen at 2.18, as derived from the EPIC pn fitting. Three Laor profiles (Laor, 1991) were then added. They are frozen at 18.97 Å, 24.78 Å, and 33.74 Å to represent O VIII, N VII and C VI respectively. The outer edge of the disk and inclination angle are frozen at 400 r_g and 35°. The inner edge was left as 1.24 r_g. The three emissivity indexes, q, were linked. The emissivity index and the normalizations were left as free parameters. See Table 11 of Appendix C for results of Laor line profile fit.

Once the broad lines were fit, the RGS data set shows a few additional narrow emission lines. The narrow emission lines are modeled first using Gaussian. The most

prominent of these lines was the O VII forbidden line. This line was seen in all seven data sets. See Table 12 of Appendix C for results of O VII line. Rev 999 also has a intercombination O VII. As noted by Mason et al. (2003), the other observations likely have some infilling occurring, resulting in the loss of this line. A Ne IX line is seen in some of the observations, but only upper limits could be measured for this line. C V is also seen in some. The lines are all very narrow and the widths can not be resolved, meaning that they must be less than 200 km/sec. See Table 13 of Appendix C for a full list of narrow emission lines seen in the seven Mrk 766 observations.

Next the absorption lines were modeled. Absorption components were added as ions and included the following: H and He like C, N, O, and Ne and L-Shell Fe XVII-XXIV. M-Shell Fe was also needed to model the trough that runs from 15.8 to 16.8 Å. This trough is Unresolved Transition Array (UTA) Fe. Again, not every observation has every line. This model yielded a reasonably good fit to the data. A list of ions and densities can be found in Table 14 of Appendix C .

The RGS data set clearly shows a Fe UTA . Rev 999's trough seems to be made of Fe XII - Fe XV, whereas Rev 1002 is made of Fe IX-Fe XIII. As to how real a change this is, it is difficult to say as not every line was measurable in every observation. Given the clear change in the shape of the trough between all data, it does appear to be real. If it is real that would imply some change to the gas that produced them.

In order to more accurately model the absorption lines, an XSTAR model was used. A two phase model was employed to model all the observed features as the

L-Shell and M-Shell Fe lines can not be accounted for by a single phase gas. They shall be designated as the High Ionization Phase (HIP) and Low Ionization Phase (LIP). The model parameters are a column density, n_H, and ionization parameter, ξ, see Tarter et al. (1969). They were first fit assuming solar abundances and altered to non-solar values. A list of the parameter values can be found in Table 5 and are plotted in Figure 28.

The LIP gas shows a small range of cloud column densities, but a wider range of ξ's. Rev 1001-1002 show a fairly tight clustering of parameters. The HIP gas shows a small range of ξ, but a wider range of column densities. Again Rev 1001-1002 shows a tight clustering of parameters. It can be assumed that sources in these three observations are being covered by the same cloud.

Rev 999's HIP phase cloud is very different from the rest. The HIP parameters are $\log \xi = 2.56 \pm 0.07$ and $\log n_H = 0.72 \pm 0.20$ (10^{22} cm^{-2}). Clearly these represent a different gas cloud and not just a gas in a different ionization phase. Given that this denser, higher ionization phase cloud only appears in Rev 999, it might be tied to the partial covering seen in Rev 999 and then vanishes in Rev 1000. This would also explain why Rev 1000 does not cluster with Rev 1001-1003. A change in cloud density and ionization would also explain the shift seen in the UTA Fe. There is a noticeable shift in the parameters from Rev 999 to Rev 1002 and to Rev 265.

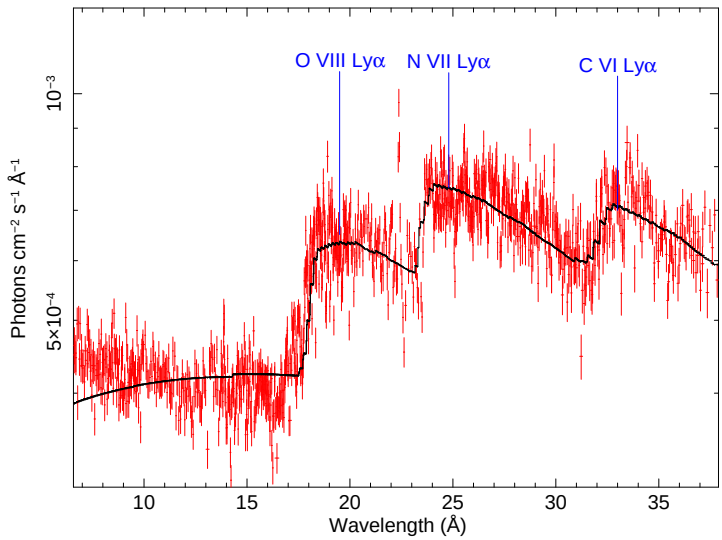

Figure 26: Broad emission features of RGS data. Time averaged of Rev 82, 265 and 999-1003.

Table 5: XSTAR model parameters

Rev	log n_H 10^{22} cm^{-2}	low log ξ	log n_H 10^{22} cm^{-2}	high log ξ	χ^2
82	$-1.68^{+0.20}_{-0.28}$	$1.30^{+0.18}_{-0.21}$	$1.03^{+0.68}_{-0.30}$	$2.22^{+0.02}_{-0.12}$	1803.93 (1703)
265	$-1.59^{+0.08}_{-0.09}$	$1.45^{+0.02}_{-0.07}$	$-1.20^{+0.13}_{-0.16}$	$2.12^{+0.07}_{-0.11}$	2297.31 (1704)
999	$-0.83^{+0.15}_{-0.18}$	$1.76^{+0.04}_{-0.14}$	$0.72^{+0.19}_{-0.23}$	$2.56^{+0.07}_{-0.08}$	1999.84 (1876)
1000	$-0.98^{+0.10}_{-0.12}$	$1.67^{+0.05}_{-0.08}$	$-0.36^{+0.15}_{-0.19}$	$2.23^{+0.04}_{-0.01}$	1971.39 (1767)
1001	$-1.16^{+0.09}_{-0.11}$	$1.55^{+0.01}_{-0.03}$	$-0.69^{+0.11}_{-0.13}$	$2.14^{+0.04}_{-0.08}$	2053.19 (1763)
1002	$-1.21^{+0.09}_{-0.10}$	$1.55^{+0.01}_{-0.04}$	$-0.60^{+0.09}_{-0.10}$	$2.10^{+0.01}_{-0.09}$	1959.74 (1736)
1003	$-1.09^{+0.07}_{-0.09}$	$1.49^{+0.02}_{-0.07}$	$-0.80^{+0.14}_{-0.18}$	$2.09^{+0.05}_{-0.08}$	2031.63 (1767)

The results of Rev 82 and 265 are consistent with Sako et al. (2003) and Mason et al. (2003). Therefore the results for Rev 999-1003 were found to be consistent with the Sako et al. (2003) and Mason et al. (2003) interpretation also.

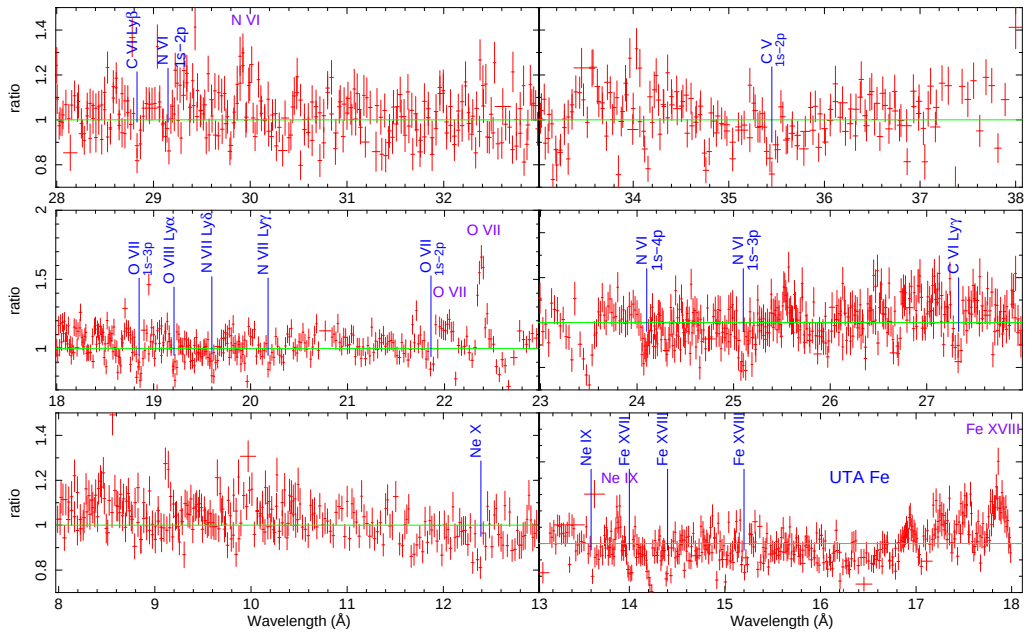

Figure 27: Ratio of data to continuum model to show narrow features. Narrow emission lines are labeled in purple and absorption lines are labeled in blue.Time averaged of Rev 82, 265 and 999-1003.

6.9. Time Resolved Data

Mrk 766 shows a wide range of spectral variability. Figure 29 shows five characteristic spectra for Mrk 766. The five spectra are the high flux states of Rev 265, 1002, 1000 and 999 in black, blue, green and cyan respectively and the low flux state of Rev 999 in red. Above 2.0 keV Rev 265, 1002 and 1000 all appear to have the same power law slope. Rev 1002 and 1000 also appear to have the same spectral shape below 2.0 keV. In other words, they have the same basic emission mechanisms but at different flux levels. Rev 265 clearly shows more soft excess, which is expected since this spectrum includes Regions 12, 17 and 18 from Figure 20, the soft flares. Rev 999

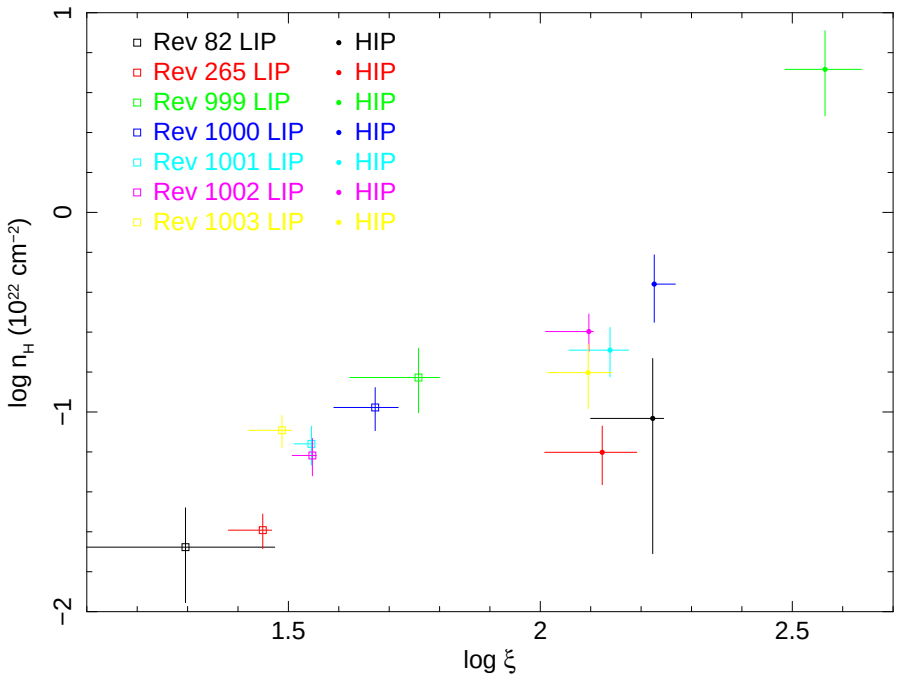

Figure 28: XSTAR model parameters

is clearly a different case. The red and cyan curves exhibit a much flatter slope above 2.0 keV.

6.9.1. Differential Spectra

In order to explore the differences seen in Figure 29, subtracted spectra were created for each of the eight observations. Subtracted spectra are where the high and low flux states of a given observation have been subtracted from one another. In other words, the low flux state is now being used for the background. Ideally this allows for the components that are constant to be subtracted out and leaves only the components that are variable. These variable components can not simply

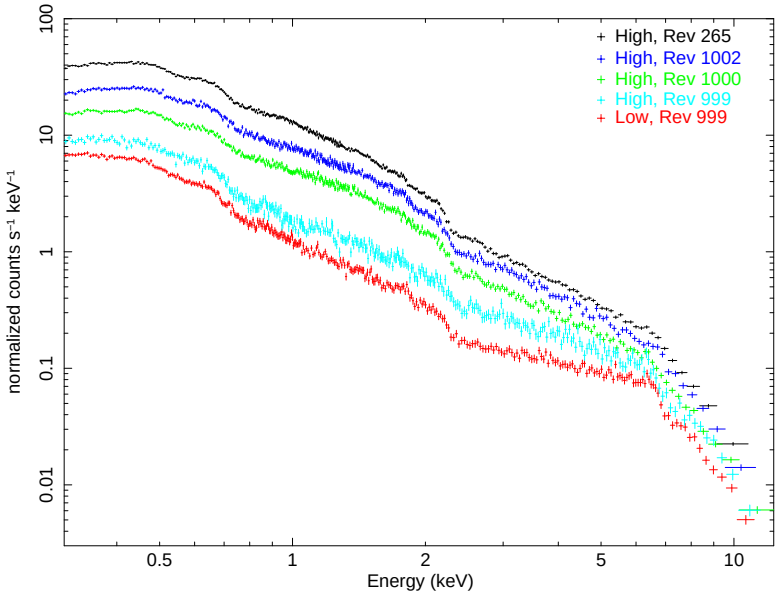

Figure 29: Five characteristic spectra of Mrk 766. High flux states of Rev 265, 999, 1000 and 1002 and low flux state of Rev 999. Note the flattening of the Rev 999 spectra above 2.0 keV. Also of interest is the increase of flux in Rev 265 below 2.0 keV.

be plugged into the models of the time resolved spectra; they are the components of the subtracted spectra. But they provide valuable information about which model components are variable. The usefulness of the subtracted spectra is limited, however. For instance, it is not possible to subtract the lowest flux spectrum from Rev 999 from the highest flux spectrum of Rev 265 because of minor instrumental differences between this and the other seven observations.

Three characteristic differential spectra are plotted in Figure 30a. The spectra are fit from 2.0-12.0 keV with a power law and Galactic absorption. The model was then extended below 2.0 keV and deviations from the model are seen. Rev 265, in

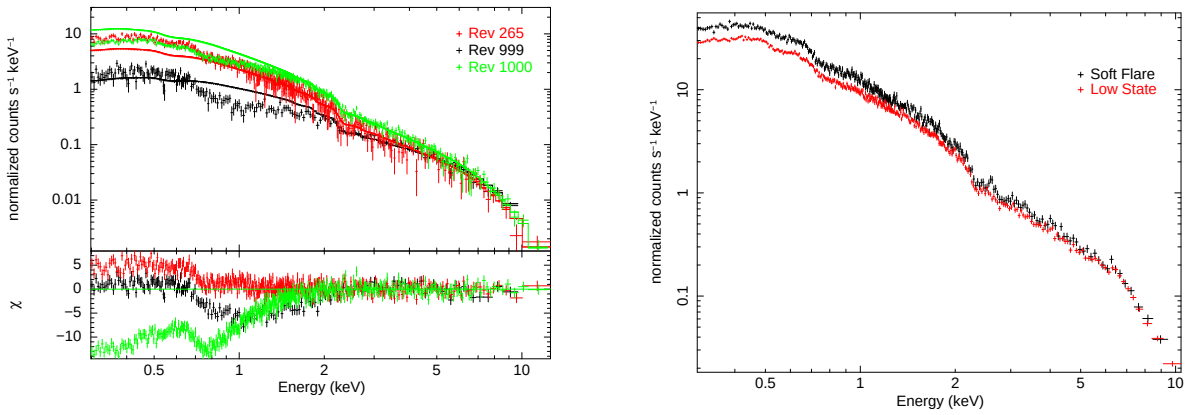

(a) (b)

Figure 30: (a) Differential spectra of Rev 265, 999 and 1000. Figure (b) Comparison spectra of regions 17 and 18, in black, to 16 and 19, in red, in Rev 265.

red, shows soft excess below 1.0 keV. Rev 999, in black, has no soft excess but is flatter and has a large absorption feature between 0.7-2.0 keV. Rev 1000, in green, also shows an absorption feature but also falls away from the model.

Rev 265 has a notable feature in its differential spectrum, soft excess. The hard band can be fitted quite well by a simple power law with a spectral index Γ of 2.18. When extended to below 2 keV there is a soft excess component. In addition there is a small notch near 0.7 keV indicating the presence of the warm absorber. It is not an unreasonable assumption to believe that the soft flares are the cause of this soft excess. If a new high flux spectrum is made by collecting the peaks again, but excluding those of the soft flares, this differential nearly eliminates the soft excess.

If just the soft flares are collected and differential spectrum is made, a difficulty arises. In order for the differential spectrum to be useful there needs to be some

separation between the high and low flux states. Figure 30b compares the soft flare, Regions 17 and 18 from Figure 20b, to the low quiet state on either side of it, Regions 16 and 19. It can be quite clearly seen in the spectra above 2.0 keV that these cases are the same. As such, the differential spectrum yields no useful information because the underlying variable component, i.e. the power law, can not be measured. Hence this soft excess component can not be explored using the differential spectrum in this manner. But if the original differential spectrum is used, a simple blackbody can be fit to the data, with a temperature of 130 eV and a radius of 1.5 x 10^5 km. These numbers are consistent with the idea that these flares are caused by a hot spot on the accretion disk. Flares, internal instabilities, initial irregularities, or other effects could easily cause this type of temperature in a 'hot spot' (Fukue, 2003). If a mass of 3 x 10^6 $M_\odot$ is assumed for the central black hole (Woo & Urry, 2002) and an inner radius of 1.24 r_g and an outer radius of 100 r_g this results in a disk of 6.4 x 10^{11} km^2 compared to an area of 7.1 x 10^{10} km^2 for the 'hot spot,' clearly a small fraction of the size of the whole disk. For more discussion on the hot spot see Section 6.10.2.

The other differential that has a soft excess component in it is Rev 1001. The soft excess seen in Rev 1001 is not nearly as large as what was seen in Rev 265. A quick look at the hardness ratio plot of Rev 1001 indicates a potential soft flare candidate. It is smaller than the soft flare seen in Rev 265, which is expected, given that the soft excess is smaller and the flux-flux plot for Rev 1001 lacks the large scatter that

Rev 265 had. Excluding this candidate from the high spectrum yields a differential spectrum similar to Rev 265 when its soft flares are removed.

Rev 999 has a very flat differential spectrum, when fit from 2.0-12.0 keV, it has a Γ=1.67±0.07. When the model is extended below 2.0 keV there is a large dip between 0.7-2.0 keV, but below 0.7 keV the model fits the data. While it is tempting to try and connect this dip with the warm absorber, the flatter power law must also be considered. If it is assumed that this initial Γ is a false slope this implies there are additional components in the differential spectrum. The most likely candidate for flattening the slope of the power law is a partial covering. Adding an ionized partial covering model not only steepens Γ to 1.95±0.08, but also explains the dip. It is explained by a moderately ionized cloud with, $\log \xi \approx 1.5$, which has a large absorption near 0.7 keV. This absorption ends below 0.55 keV due to the gas's transparency to photons below 0.55 keV. If the partial covering component is variable in Rev 999, the true power law slope and partial covering parameters can not be derived from the differential spectrum alone.

The differential spectrum for Rev 1000 is highly unusual. Fitting a power law in the hard band yields a steeper slope, Γ= 2.39, than in any of the other observations. Then when the model is extended below 2 keV, an odd residual is left. There is a clear absorption feature in the form of a notch near 0.7 keV, where either a warm absorber or a partial covering model, as in Rev 999, is affecting the spectrum. For energies below the notch, the data continues to fall away from the model rather than

coming back into agreement with the model as in Rev 999 or forming a soft excess like in Rev 265.

The question then becomes why Rev 1000 is different. Rev 1000 is the transition phase from the low flux levels of Rev 999 to the medium flux levels of the other 2005 observations. It is known from the flux-flux plots that there is a component present in Rev 999 and the early stage of Rev 1000 that disappears in the later stages of Rev 1000. If the change seen in branches of the flux-flux plots, Figure 22b, is due to a change in the partial covering, it is expected that the low state of Rev 1000 should have a thicker cloud covering it. The major result of the larger partial covering is to flatten the spectra as seen in Figure 29. When the spectra are subtracted in Rev 82, 265, or 1001-1004, the observed power law component has the same photon index Γ, but different flux levels. Thus what is being seen is really the difference between these flux levels and not the constant continuum components. This is not the case in Rev 1000. The observed photon index Γ and flux levels are different, resulting in a different comparison. The thick partial covering cloud used in Rev 999 and the early part of Rev 1000 creates a flatter observed Γ. What were the constant components have been modified and are no longer truly constant components. Hence, what is seen is a combination of two different slopes resulting in a false slope.

A true slope is more likely to be measured by taking a different differential spectrum of Rev 1000. If the medium flux states are collected and subtracted from the collected peaks, a differential is produced that looks much more similar to the others,

except for Rev 999. The individual spectra are more similar, showing the same slope between 2.0-12.0 keV but at different flux levels. And the Γ of this spectrum is also closer to that of the average. A simple power law fit has a Γ=2.12$\pm$0.02, which is within the error bars of the low end of the average of the other differential spectrum.

Rev 82 and 1002-1004 all have very similar shapes. All are well defined by a single power law. When that model is extended below 2 keV all have a clear notch from the warm absorber or from partial covering.

6.9.2. Composite Model

The X-Ray model above 2.0 keV consisted of a power law with fixed slope of Γ=2.18, with free normalization, a constant reflection with PEXRAV set at 35°, a narrow Gaussian at 6.4 keV and a small absorption line near 6.9 keV as needed. The soft model includes blurred ionized reflection, an absorption edge for the warm absorber near 0.70 keV and a Gaussian line near 0.46 keV as needed. All of these components are partially covered with an ionized cloud, modeled by ZXIPCF. These parameters can be found in Table 15 and 16 of Appendix D.

The power law is the most dominant component in the model. The fixed Γ of 2.18 was obtained from the differential spectra, see section 6.9.1. The flux-flux plots show linear behavior, which would rule out spectral pivoting. As such there is reason to believe that the slope seen in the differential spectra is the real power law slope.

The partial covering accounts for some of the variability seen in Mrk 766. Partial covering is where a cloud of some absorbing material covering some percent of the

primary source and the rest is seen directly. The branching seen in the flux-flux plot is explained by a difference in partial covering. In the case of Rev 999 and the early part of Rev 1000, a thicker cloud covers a smaller emission region. As the source transitions from the dim state of Rev 999 to the average state of Rev 1000 the emission region increases in size and a thinner cloud is needed. Due to a lack of additional side branches in the flux-flux plots, the later part of Rev 1000 to 1004 are assumed to have the same cloud. The average value of cloud density and ionization parameter were taken and fixed. The same fitting procedure was applied to Rev 82, 265 and 999. Rev 999 and the beginning of Rev 1000 are assumed to be caused by the same thicker cloud. As Rev 1000 ramps up, the source enters its average phase. Partial covering works reasonably well to explain the variability, but not in every case and does not explain the short term variability.

A blurred ionized relativistic reflection, as described in Section 2.3.5, was used to model the soft excess. The parameters of KDBLUR are the same as those from the LAOR profile fit to the Fe Kα line. The inner and outer radii are left the same, 1.24 r_g and 400 r_g, respectively. The angle is still 35°. The emission index, q, was left as a free parameter, but not allowed to vary more than 30% from the value found in Section 6.8. For REFLION, the illuminating photon index was linked to the power law's photon index, $\Gamma = 2.18$. Due to the fact there is a large, broad Fe line, this indicates a greater than solar abundance of Fe. It was not possible to estimate the Fe abundance in the time averaged spectra. Therefore a value of three times solar was

used. The ionization parameter, ξ, and normalization were left as free parameters. The ξ ranges from 100-350.

The short term variability is a combination of the ionized reflection and power law, as described in Section 2.3.5. The direct continuum is assumed to be located at a height above, but close to the central Kerr black hole. As the height of the direct continuum changes, the reflection component flux is either correlated, anti-correlated or nearly independent of the direct continuum flux. See Miniutti & Fabian (2004) for further details of the model. The ionized reflection is a constant component in the model, varying only within the error bars of the flux. As such it stays fixed while the power law continues to vary. This is the same model used by Vaughan & Fabian (2004) and Ponti et al. (2006) for MGC-6-30-15 and NGC 4051. However a partial covering component also plays a role. As the source brightens and dims, the change of power law component with a fixed slope controls the variability. See Section 6.10.1 for more discussion on this topic.

The warm absorber is crudely modeled here with a pair of absorption edges. The first edge is at around 0.68 keV and is due to the UTA Fe seen in the RGS data. In the lower flux states a second edge is sometimes needed near 0.50 keV. Both values float around, although the second edge seems to have a wider range of values. An additional absorption feature at 6.9 keV is seen in the spectrum above 2.0 keV. This is likely due to Fe. The line is very narrow and unresolvable. As such an optical depth can not be measured for this feature.

Finally, there is a last residual left near 0.48 keV. A Gaussian was used to fit this feature. This does not match any of the known lines of the RGS data. This line and the second absorption edge could be the result of REFLION's limitations rather than a true physical feature. REFLION can not alter any of the abundances other than Fe. The RGS data indicates an excess of N VII and a lack of O VII. In Rev 999 and 1000 the line is closer to 0.56 keV and 0.65 keV, which could be O VII and O VIII, both of which are seen promptly in the RGS data.

Eight characteristic spectra are shown Figure 31. Based on characteristic spectra of Figure 29, eight spectra have been picked to show their model components. The model components are indicated by the following colors. The direct power law is in red, the partially covered power law is in dark blue, ionized reflection in green, Compton reflection in light blue, blackbody in purple, the narrow Fe Kα line in magenta and the narrow line near 0.46 keV in orange. Region 16 is a minimum region before the soft flare Region 17. Region 17 shows a soft flare spectrum with a blackbody model. Aside from the blackbody model in Region 17, these regions appear very similar as expected from Figure 30b. Region 22 is a large normal flare from Rev 265 to show the difference between the soft flares and normal flares. Region 30 and 32 are from Rev 999 and show the effects of the thick partial covering model. The ionized reflection is now at a level relative to the power law's flux level so that it causes a suppression of the variability as seen in RMS spectra, see Figure 23. Region 39 and 40 are from Rev 1000 and show the effects of a thin partial covering model

and changes on the ionized reflection model. Region 60 from Rev 1002 shows the continued effects of the thin partial covering and constant ionized reflection. The power law flux level in Regions 16,17, 22, 39, 40 and 60 is well above the ionized reflection flux level. As such a majority of variability is a result of the change of the power law.

6.10. Discussion

6.10.1. Partial Covering

Partial Covering was used to explain the change seen between the quiet state of Rev 999 and the beginning of Rev 1000 to more average states of Rev 82, Rev 1001-1004 and most of Rev 1000. To explain the branching in the flux-flux plot and flattening of the low flux state spectra, the proposed scenario is where a thick cloud, $n_H \approx 16 \times 10^{22}$ cm^{-2}, partially obscures the emission region during Rev 999 and the beginning of Rev 1000, as illustrated in Figure 32a. A thinner cloud, with $n_H \approx 1.5 \times 10^{22}$ cm^{-2}, is then applied to the rest of Rev 1000 through Rev 1004, as illustrated in Figure 32b. A thicker partially ionized cloud also explains the RGS data of Rev 999. While models can not be directly compared, what can be said is that a partially ionized cloud of comparable column densities was used in both data sets.

A question that immediately arises from this scenario is how fast does this transition take place? The transition from the low flux branch region takes place in Rev 1000 and only Rev 1000. In order to see this transition better, it is worth looking at

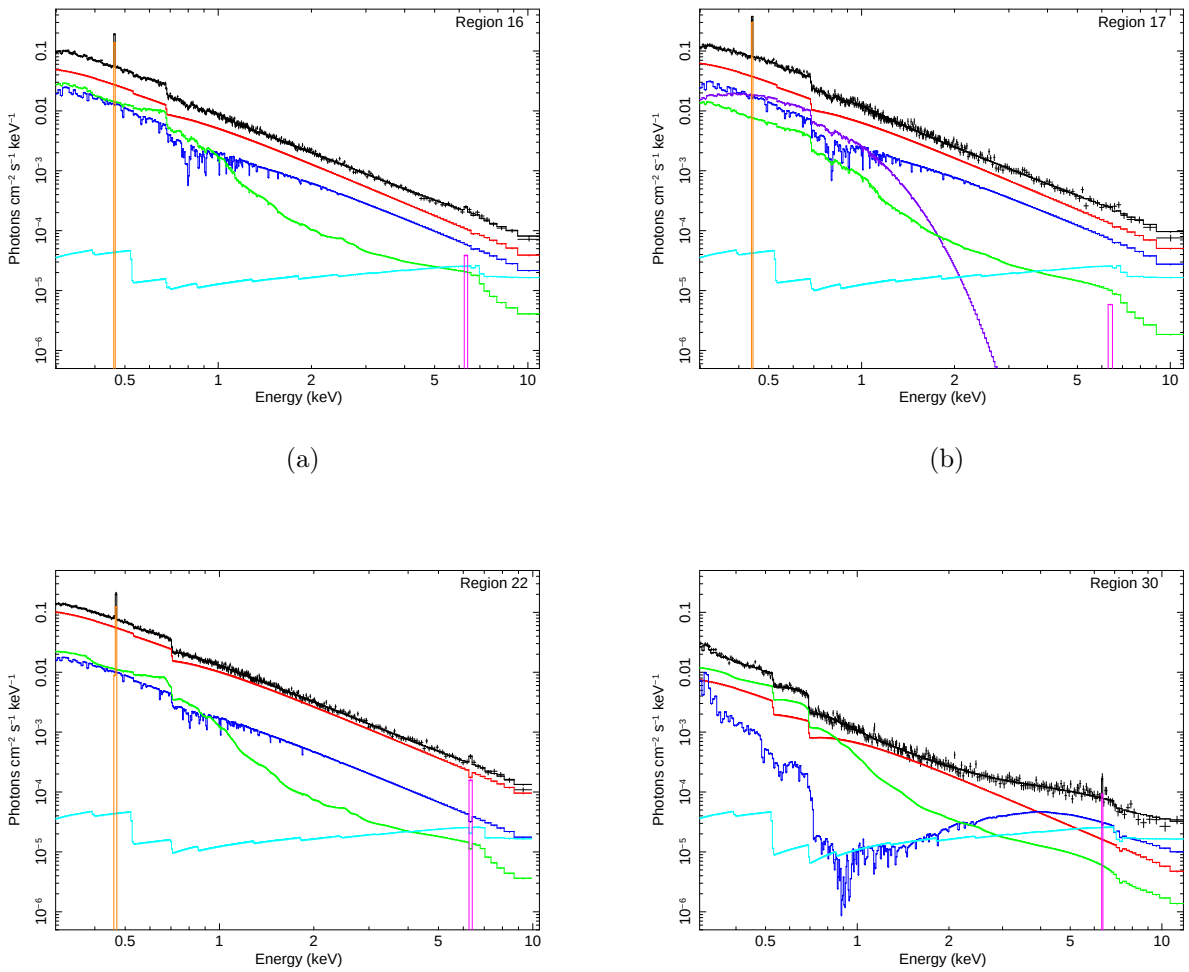

(a) (b) (c) (d)

Figure 31: Characteristic spectra of Mrk 766. Direct power law is in red, ionized reflection in green, the partially covered power law is in dark blue, Compton reflection in light blue, blackbody in purple, narrow Fe Kα line in magenta, the narrow line at 0.46 keV in orange. Region 16 of Rev 265 is the low flux region before the soft flares. Region 17 of Rev 265 is a soft flare region and has the same basic model as Region 16 but with the addition of a blackbody. Region 22 is a large normal flare of Rev 265. Region 30 is a very low state of Rev 999.

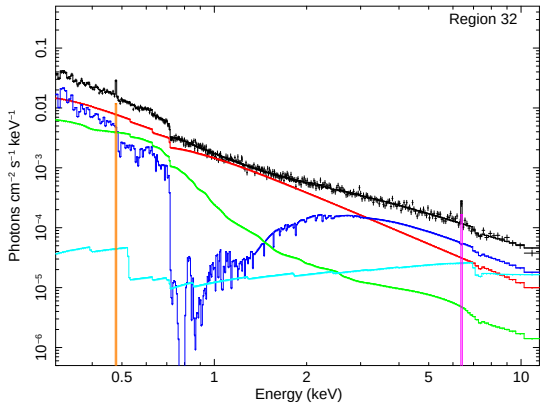

(e)

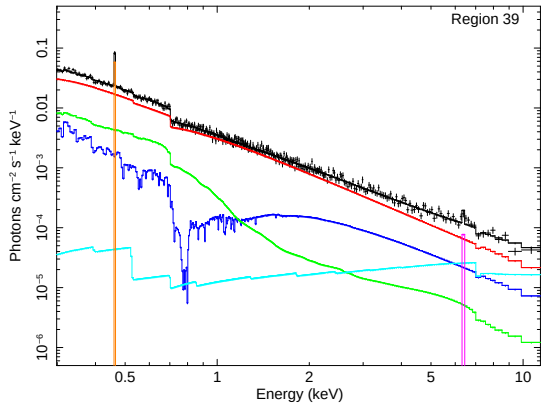

(f)

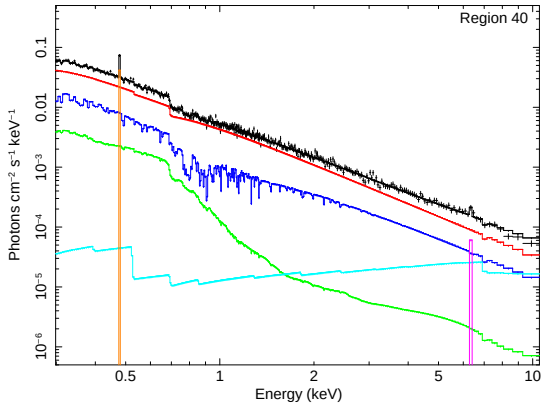

(g)

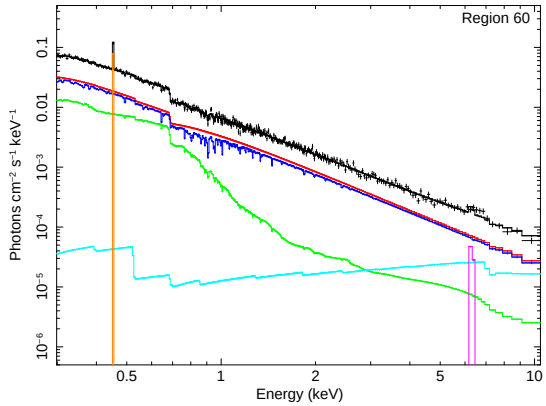

(h)

Figure 31 – Continued: Region 32 is a high state of Rev 999. Region 39 is a medium state of Rev 1000 and Region 40 is a high state of Rev 1000. Region 60 is a middle state of Rev 1002.

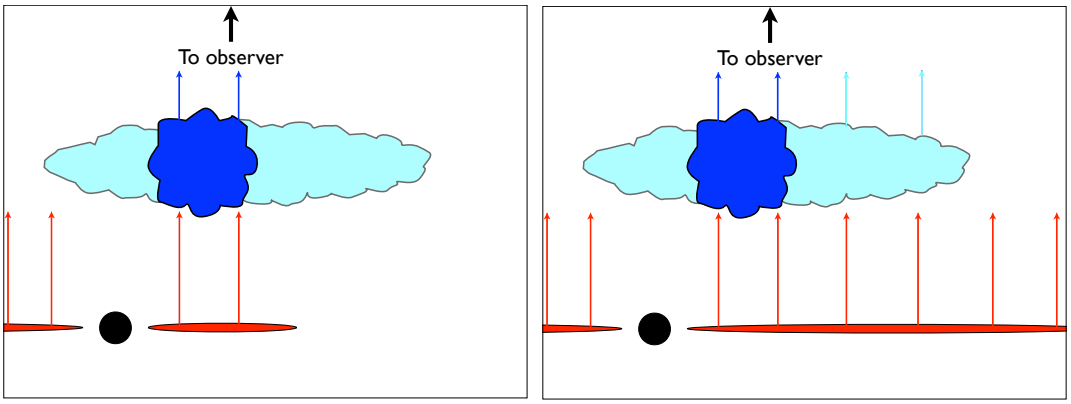

(a) (b)

Figure 32: Cartoons illustrating the scenario of partial covering by a lumpy cloud, items not drawn to scale. The primary emission region is in red, the reprocessed light from the thick cloud is in blue and the reprocessed light from the thin cloud is in cyan. Figure (a) shows the thick cloud partially covering the smaller emission region of the low flux source. Figure (b) shows the combination of the thick and thin clouds partially covering the source.

the flux-flux plot of only Rev 1000, see Figure 33. By labeling the different regions of Rev 1000 it can be clearly seen how the different regions relate to one another, in particular Regions 35, 36 and 37 of Figure 20. It can be seen that Region 36 is part of the Rev 999 branch and that Region 37 is part of the main branch. So by the time the lightcurve is ramping up in Region 37, the spectrum has returned to its average state. Therefore the transition happens during Region 36, a 10 ksec long region.

The next question is how does a large cloud of ionized gas change its column density almost an order of magnitude in under 10 ksec? Given how large such a cloud would have to be in order to partially cover the emission region it seems unlikely that the thick cloud dissipated into the thin cloud. The most likely scenario is a lumpy cloud; the thick cloud stays fixed and that the emission region has changed. When

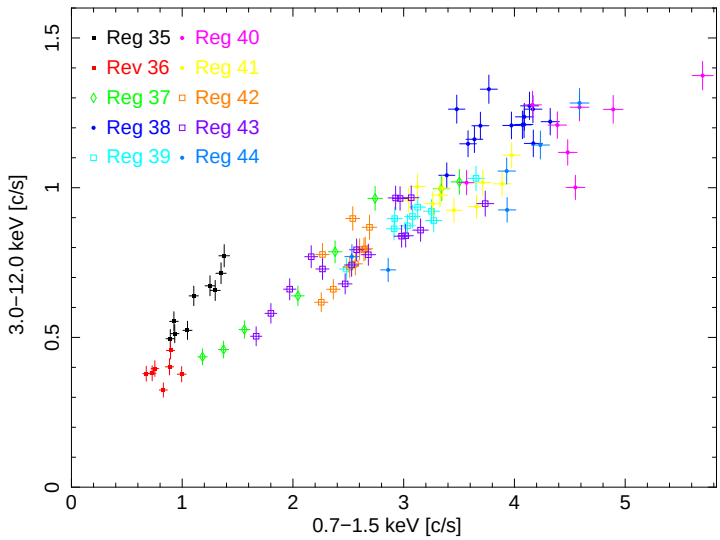

Figure 33: 0.7-1.5 vs. 3.0-12.0 keV flux-flux plot of Rev 1000 only. The flux-flux figure has been split out into the different regions and labeled. Closed squares are the low flux states of Region 35 and 36. Diamonds are the ramp phase. Closed circles are the flare states and open squares the non-flares. Note that Region 36 (red) is the pivot point of the side branch to the main branch.

the source is dim, such as in Regions 29-36, the emission region is small and covered by a thicker part of the cloud, see in Figure 32a. As the source brightens, the emission region grows and is no longer effectively covered by the thicker portion of the cloud. Instead, a thin portion of the cloud covers the larger emission region resulting an average of the two clouds being observed, see Figure 32b.

As noted for NGC 4051, Mrk 766 also has strong evidence of starburst activity. Rodriguez-Ardila & Viegas (2003) reported only upper limit detections of polycyclic aromatic hydrocarbon (PAH) emission for NGC 4051. For Mrk 766 they firmly observed 3.3 μm PAH emission. Starburst activity is noted for the ability to produce

inhomogeneous and turbulent torus-like structures (Wada & Norman, 2002). Molecular tori play an important role in obscuring the central regions of Seyfert 2s in the AGN unified model (Antonucci, 1993). The partial covering scenario suggested here could be connected to starburst activity seen in Mrk 766 as in NGC 4051 and other NSL1 galaxies.

For this reason, the partial covering cloud is incorporated in the medium and high flux states models. Relying only on partial covering to explain all the variability doesn't work. If partial covering were solely responsible for variability, a plot of the covering fraction vs. time would be anti-correlated to a plot of flux vs. time. The later part of Rev 1000 partial covering works reasonably well, but there is not a perfect correlation between the covering fraction and flux. Rev 1001 and 1003 have a complete breakdown of the relationship, with no clear pattern. As the reflection dominated component has been so successful in explaining the variability seen in MGC-6-30-15 (Vaughan & Fabian, 2004) and it is already being used here, its use to help explain the variability seen in Mrk 766 in combination with partial covering is a natural fit.

6.10.2. Soft flares

With only three definite soft flares in Rev 265 and a handful of candidate soft flares in Rev 1000, 1001 and 1002, the statistics for the study of this phenomenon is limited. Four primary emission mechanisms were considered: Power law, thermal bremsstrahlung, blackbody, and ionized reflection. The power law and bremsstrahlung

models yielded unacceptable model parameters and fit statistics The bremsstrahlung plasma temperature of $kT \sim 0.55$ keV is acceptable, but the electron density, $n_e \sim 10^{12}$ cm^{-3}, is too low for expected AGN type values (Barvainis, 1993). The power law model is a poor fit to the data, with a reduced $\chi^2 = 1.58$. A $\Gamma \sim 2.33$ is also much larger than $\Gamma = 2.18$, which been used in all other regions. And spectral pivoting is ruled out because of the lack of change seen in the 2.0-12.0 keV band of Figure 30b. The ionized reflection model, even being a highly flexible model, has problems in the interpretation. Miniutti & Fabian (2004) predict that when the direct continuum flux is high the ionized reflection flux should be nearly constant, see Miniutti & Fabian (2004) Figure 2. As the soft flares only increase in the soft excess this interpretation is problematic for this model. Therefore these models are ruled out.

That leaves only the blackbody. The blackbody model, like the ionized reflection model, yields an acceptable fit. The parameters result in a temperature higher than what an accretion disk should be able to support (Mineshige et al., 2000) and a radius that is well inside the event horizon of the central black hole. And as previously noted, this area is only a small fraction of the area of the whole accretion disk. Given that the radius is a few times 100,000 km, a hot spot on the disk is a more likely interpretation. The largest radius has a light crossing time of about 3 sec, which is much smaller than the time scale of the flare ≈ 2.6 ksec, meaning that the effect that caused the soft flare had more than enough time to propagate across this region.

If soft flares are the result of a hot spot on a standard Keplerian disk, the lightcurves prove to be problematic. For a Keplerian disk it is established that a hot spot on the disk should produce two peaks in a period of $\sim 100\ \frac{r_g}{c}$ for an orbital radius of 4 r_g, see Asaoka (1989); Bao (1992); Karas & Bao (1992); Karas (1996) or 1000-2000 ksec for a 3 x 10^6 $M_\odot$ black hole. In the case of Regions 17 and 18 of Figure 20, this may be fine as the hot spot could be orbiting closer. There are two separate peaks with a larger first peak and slightly broader second peak. However Region 12 has only a single peak, as do all the candidate soft flares. The solution to this problem may lie in non-Keplerian accretion disks. Fukue (2003) showed that sub-Keplerian advective disks are capable of producing aperiodic lightcurves. These can be single peaks or double peaks.

Possible causes of the soft flares are: X-ray flares, hydrodynamic shocks, magneto-hydrodynamic (MHD) instabilities, and disk oscillations. Hydrodynamic shocks and disk oscillations would have quasi-periodic oscillations, see Nagakura & Yamada (2008, 2009) whereas the soft flares in Mrk 766 appear to be random. But given the data set consisting of only three soft flares and a couple of candidates, it is difficult to say if the soft flares are truly random. MHD instabilities and X-ray flares would have a more random nature. X-ray flares in galactic black hole candidates (GBHC), like Cyg X-1, exhibit similar power spectra to what is seen in Mrk 766's power spectra. Numerical simulations of MHD instabilities (Machida & Matsumoto, 2003) and self-organized critical disk models (Negoro et al., 2001) predict a soft X-Ray

flare, but also a hardening of the peak of the flare and a hard X-Ray time lag, neither of which is seen in Mrk 766. Uttley et al. (2005) note that although 'shot-noise' models, such as those proposed by (Merloni & Fabian, 2001 and Mineshige et al., 1994), predict the Power Spectral Density (PSD) accurately, they do not reproduce a linear rms-flux relationship. Mrk 766 clearly has a linear rms-flux relationship, see Vaughan & Fabian (2003) for Rev 265 and Markowitz et al. (2007) for Rev 999-1004.

The time scales of the soft flares are difficult to assess. The main problem is that soft flares are superimposed on top of an already variable lightcurve. What is seen are only the flares bright enough to overcome the continuum lightcurve. Region 12 is a particularly difficult flare as it does not occur in isolation, like Regions 17 and 18, but Region 12 is the last of a series of flares before a quiet interval. So not only is the true rise obscured, but the true fall may also be obscured. In contrast, Regions 17 and 18 occur in a rather clean portion of the lightcurve. The 2.0-12.0 keV lightcurve, Figure 21b, clearly shows no behavior other than that of a stable region.

To overcome this difficultly the rise and fall times for soft flares are measured from the hardness ratio plot rather than the lightcurve. The start of the soft flare is assumed to be when the hardness ratio begins to soften. The peak count rate, measured from the lightcurve, is assumed to be the turning point between rising and falling. For comparison, four normal flares were also measured. These were measured directly from the lightcurve. What can be seen in Table 6 is that in general, the soft flares' rise and fall are sharper than their normal counterparts. The soft flares rise

Table 6: Time scales of soft flares and normal flares. The soft flares have sharper features that rise and fall quicker than the normal flare. The soft flares also show a more consistent rise and fall.

Region (Soft)	Rise time (sec)	Fall time (sec)
12	1000±125	1650±125
17	1550±125	1125±125
18	875±125	1850±125
Region (Normal)	Rise time (sec)	Fall time (sec)
11	3200±125	2500±125
14	2200±125	4300±125
20	3000±125	3800±125
22	4700±125	2500±125

Table 7: Table of 'hot spot' temperature and radii.

region	kT (keV)	Radius (10^5 km)
12	0.126±0.006	4.458
17	0.130±0.020	2.745
18	0.126±0.015	3.583

close to twice as fast. As for the soft flares themselves, Regions 12 and 18 exhibit very similar rising and falling behavior in about the same time scale. Region 17 rises slower but falls faster. Given the small data set and only three data points, the significance of this is undetermined.

Considering the limited nature of the current data set it is extremely difficult to do much but speculate on the causes. Searching for additional soft flares in this source and others will be critical to further understanding of this phenomenon.

6.11. Conclusion

Mrk 766 is a complex source. It exhibits both long term and short term variability. The long term variability seen here has been demonstrated to be caused by a change in the partial covering of the primary emission region. The short term variability is primarily caused by the variable power law component moving relative to the relatively constant ionized reflection component. These interpretations explain the features seen in the composite spectra, flux-flux plots and RMS spectra.

Using the RGS data the soft excess is best explained by the ionized reflection model. Other models do not explain the features seen in the RGS data as well as the broadened emission lines, typical of the ionized reflection model. When this is taken with the broad Fe line, the ionized reflection model is the most physically correct model.

An additional feature is also seen in the lightcurve of Mrk 766, soft flares. Currently these flares are not well understood. Additional data from this source and others will be needed to begin to understand them more completely. With the current data the best explanation is a hot spot on an advection dominated accretion disk. Further research will have to be done to see if the interpretation is correct.

CONCLUSION

The dynamical spectral method has been used extensively throughout this work. Several important regions have been identified and extensively studied. These key regions have proven to be essential in the understanding of these sources.

A summery of the major finding of this work is:

1. NGC 4051's variability was shown to be caused by a change in the primary emission region. A thick cloud partially covers this primary emission. As the emission region grows or shrinks, the covering fraction changes, resulting in the dramatic variations seen in this source. Further, it was demonstrated that there exists a unique region where the emission region has reached a true minimum phase and is no longer covered by the thick cloud. Additionally when the source was in it's low and minimum phases a thermal plasma feature was seen that suggests the presence of a nuclear starburst region.

2. IRAS F12397+3333 was shown to have the same type of dusty warm absorber as IRAS 13349+2438. A two phase warm absorber, a high ionization phase cloud and a low ionization phase cloud, was needed to model all of the lines seen. Features that have previously been identified as O VII and O VIII are in fact Fe absorption features. Like IRAS 13349+2438, the high ionization phase cloud was shown to have an upper limit consistent with being located in the Narrow-Line Region.

3. Mrk 766 is a highly complex source in terms of its variability. The long term variability has been shown to be caused by partial covering of a partially ionized gas

cloud. The short term variability is primarily caused by the flux of the power law component moving relative to that of the ionized reflection component. This ionized reflection component is also responsible for the soft excess and broad ionized Fe Kα seen in the source. On top of all of is, there is a feature currently being investigated as a hot spot on an advection dominated accretion disk.

4. Dynamic spectral analysis method led to the identification of the true minimum phase of NGC 4051 and periods when the thermal plasma feature is observable. The nature of the long term variability and soft flare of Mrk 766 was only discovered when using this method. These regions are key to understanding of these sources.

Possible future work using this method includes a new analysis of NGC 4051 due to the 15 additional observations made in 2009, NGC 3227, Mrk 335, Pks 0558-504 and 1H 0707-495. The new observations of NGC 4051 would allow for the further testing of the proposed model of partial covering. It would allow one the opportunity to see if this model continues to work or if perhaps a modification needs to be made. It also allows for the opportunity to look for further periods of extreme low flux levels.

NGC 3227 is another Narrow Line Seyfert 1 galaxy that exhibits starburst activity and rapid variability. Given the similarities to NGC 4051 and Mrk 766 one would expect a similar class of model would apply to this source.

Mark 335, Pks 0558-504 and 1H 0707-495 have been identified as potentially worthy candidates for dynamic spectral analysis. This is based on the fact that these sources exhibit similar levels of variability to NGC 4051 and Mrk 766 and multiple long

observations are available. This combination is ideal for further use of the dynamic spectral analysis methods used here.

The soft flare phenomenon will require much more work for better understanding. In addition to continued work on Mrk 766, more sources that exhibit this phenomenon will have to be identified. The dynamical spectral analysis method is ideally suited for identifying and analyzing these soft flares when they are found.

APPENDICES

APPENDIX A

XSPEC MODELS

List of XSPEC models used in this work.

The following is a list of XSPEC spectral models used in this work. A brief description of each model is given, followed by a list of the model parameters and their description. Further detail may be found in the XSPEC User's Guide (2010) from which these descriptions were taken.

BBODY

Blackbody spectrum

$A(E) = K \frac{8.0525 E^2 dE}{(kT)^4 (\exp(\frac{E}{kT}) - 1)}$

Model parameters

- kT Temperature measured in keV
- K Normalization defined as $\frac{L_{39}}{D_{10}^2}$, where L_{39} is the source luminosity in units of 10^{39} ergs sec^{-1} and D_{10} is the distance to the source in units of 10 kpc

BKNPOWER

Broken powerlaw

$A(E) = K E^{-\Gamma_1}$ for $E < E_{break}$

$A(E) = K E_{break}^{\Gamma_2 - \Gamma_1} E^{-\Gamma_2}$ for $E > E_{break}$

Model parameters

- Γ_1 Powerlaw photon index for $E < E_{break}$
- E_{break} Break point energy, units of keV
- Γ_2 Powerlaw photon index for $E > E_{break}$
- K Normalization defined as photons keV^{-1} cm^{-2} sec^{-1} at 1 keV

KDBLUR

Smooths a spectral model due to relativistic effects from proximity to a rotating black hole. Convolves the spectral model with kernel used in Laor (1991).

Model parameters

- q Emissivity index
- R_{in} Inner radius of accretion disk units of $\frac{GM}{c^2}$
- R_{out} Outer radius of accretion disk units of $\frac{GM}{c^2}$
- θ Inclination of accretion disk. Measured in degrees

LAOR

Doppler broadening emission line due to motion of the emitting gas in a thin Keplerian accretion disk rotating black hole based on the calculation of Laor (1991).

Model parameters

- E_L Line energy in units of keV
- q Emissivity index
- R_{in} Inner radius of accretion disk units of $\frac{GM}{c^2}$
- R_{out} Outer radius of accretion disk units of $\frac{GM}{c^2}$
- θ Inclination of accretion disk. Measured in degrees
- K Normalization defined as total photons cm^{-2} sec^{-1} in the line

MEKAL

Emission spectrum from a thermal plasma based on the calculations of Mewe and Kaastra and Fe L calculations by Liedahl. See Mewe et al. (1985), Mewe et al. (1986) and Liedahl et al. (1995).

Model parameters

- kT Plasma temperature in units of keV
- n_H Hydrogen density in units of cm^{-3}
- abund Abundances of metals relative to solar. Metals are C, N, O, Ne, Na, Mg, Al, Si, S, Ar, Ca, Fe and Ni.
- z Redshift
- switch Switch determines which type of code is run by mekal model. Spectral models can be calculated for each temperature or interpolated from pre-calculated tables.
- K Normalization defined as $\frac{10^{-14}}{4\pi(D_a(1+z))^2}\int n_e n_H dV$ where D_a is the angular diameter distance to the source in units of cm, n_e and n_H are the electron and hydrogen densities.

PEXRAV

Exponentially cut-off powerlaw reflected from neutral matter by Magdziarz & Zdziarski (1995). Output spectrum can be either the sum of the cut-off powelraw and reflection component or reflection component alone. In this work only the latter was used.

Model parameter

- Γ Powerlaw photon index
- E_c Cut-off energy in units of keV
- rel_{refl} Reflection scaling factor. $-1 < rel_{refl} < 0$ represents the reflection only component for an isotropic source above the disk.
- z Redshift
- abund Abundance of metal excluding Fe relative to solar
- feabund Abundance of Fe relative to solar
- $\cos\theta$ Cosine of inclination angle
- K Normalization defined as photons keV^{-1} cm^{-2} sec^{-1} at 1 keV

PHABS

Photo-electric absorption using cross-sections, $\sigma(E)$, from Balucinska-Church & McCammon (1992) with new He cross-section fromYan et al. (1998). Model excludes Thomson scattering.

$M(E) = \exp\left(-n_H \sigma(E)\right)$

Model parameters

- n_H Equivalent hydrogen column density in units of 10^{22} atoms cm^{-2}

POWERLAW

Simple photon powerlaw.

$A(E) = KE^{-\Gamma}$

Model parameters

- Γ Powerlaw photon index
- K Normalization defined as photons keV^{-1} cm^{-2} sec^{-1} at 1 keV

REFLIONX

Reflection by a constant density, optically thick atmosphere illuminated by powerlaw spectrum by Ross & Fabian (2005).

Model Parameters:

- feabund Fe abundance relative to solar
- Γ Illuminating powerlaw spectrum photon index
- ξ Ionization parameter. $\xi = \frac{4\pi F}{n}$, where F is the total illuminating flux and n is the hydrogen number density
- z Redshift
- K Normalization of reflected spectrum

WARMABS

Warm absorber model that uses XSTAR calculated level populations for elements 1-30.

Model Parameters:

- log n_H Hydrogen column density. n_H is in units of 10^{22} cm^{-2}
- log ξ Ionization parameter as defined by Tarter et al. (1969)
- xabund Abundance of elements 5-30 relative to solar
- z Redshift
- vturb Turbulent velocity in units of km sec^{-1}

ZEDGE

Redshifted absorption edge.

$M(E) = 1 \qquad \text{for E} < \text{E}_\text{c}$

$M(E) = \exp\left(-D\left(\frac{E(1+z)}{E_c}\right)^3\right) \qquad \text{for E} > \text{E}_\text{c}$

Model parameters

- E_c Threshold energy
- D Absorption depth at threshold
- z Redshift

ZGAUSS

Redshifted gaussian line profile.

$A(E) = \frac{K}{(1+z)\sigma^2\sqrt{2\pi}} \exp\left(\frac{1}{2}\left(\frac{(1+z)E-E_l}{\sigma}\right)^2\right)$

Model parameters

- E_L Line energy in units of keV
- σ Line width in units of keV
- z Redshift
- K Normalization defined as total photons cm^{-2} sec^{-1} in the line

ZPCFABS

A partial covering fraction absorption model. Fraction f of the source is covered, while the remaining fraction 1-f, is seen directly.

$M(E) = f\ \exp\left(-n_H\sigma(E)\right) + (1-f)$

$\sigma(E)$ is the photo-electric cross-section. Excludes Thomson scattering.

Model parameter

- n_H Equivalent hydrogen column density in units of 10^{22} atoms cm^{-2}
- f Dimensionless covering fraction
- z Redshift

ZXIPCF

Partial covering absorption by partially ionized material. Uses a grid of XSTAR photoionized absorption models. Fraction f of the source is covered, while the remaining fraction 1-f, is seen directly.

Model parameters

- n_H Equivalent hydrogen column density in units of 10^{22} atoms cm^{-2}
- log ξ Ionization parameter as defined by Tarter et al. (1969)
- f Dimensionless covering fraction
- z Redshift

APPENDIX B

NGC 4051 EPIC PARAMETER TABLES

Tables of fit parameters for each of the temporal regions for NGC 4051. These are divided into continuum components and atomic features. Table 8 is the continuum model, which was made of a power law that is partially covered by a neutral absorbing cloud and blackbody. Table 9 covers the atomic features, which include Fe Kα line, O VII and VIII line and warm absorber edge. Finally Table 10 shows the parameters for the thermal plasma model used in the 2002 data .

Table 8: Continuum model parameters for NGC 4051.

	Γ	norm[a]	kT[b]	norm[c]	CF %	χ^2 (d.o.f.)
1	$2.27^{+0.04}_{-0.04}$	$15.8^{+1.4}_{-1.3}$	$111.8^{+1.9}_{-1.9}$	$20.8^{+0.6}_{-0.5}$	$21.9^{+2.2}_{-2.2}$	1.08 (319)
2	$2.26^{+0.03}_{-0.03}$	$18.7^{+1.3}_{-1.1}$	$112.5^{+1.5}_{-1.5}$	$23.6^{+0.5}_{-0.5}$	$24.6^{+1.5}_{-1.6}$	1.09 (319)
3	$2.23^{+0.04}_{-0.04}$	$14.3^{+1.2}_{-1.2}$	$110.2^{+1.5}_{-1.4}$	$22.7^{+0.5}_{-0.5}$	$25.9^{+1.8}_{-1.8}$	1.07 (313)
4	$2.10^{+0.05}_{-0.05}$	$9.0^{+1.0}_{-0.8}$	$106.8^{+2.0}_{-2.0}$	$13.7^{+0.3}_{-0.3}$	$41.1^{+1.5}_{-1.7}$	1.00 (338)
5	$2.07^{+0.05}_{-0.05}$	$9.6^{+1.0}_{-0.9}$	$106.2^{+1.4}_{-1.4}$	$19.0^{+0.4}_{-0.4}$	$27.5^{+1.9}_{-2.0}$	1.06 (338)
6	$2.03^{+0.07}_{-0.07}$	$6.0^{+0.8}_{-0.8}$	$106.6^{+1.7}_{-1.6}$	$9.4^{+0.2}_{-0.2}$	$59.3^{+1.2}_{-1.2}$	1.11 (340)
7	$2.20^{+0.04}_{-0.04}$	$10.8^{+1.1}_{-0.9}$	$108.3^{+1.6}_{-1.6}$	$18.7^{+0.4}_{-0.4}$	$17.7^{+2.3}_{-2.4}$	1.05 (323)
8	$2.30^{+0.03}_{-0.03}$	$19.8^{+1.3}_{-1.2}$	$113.7^{+1.2}_{-1.2}$	$29.7^{+0.5}_{-0.5}$	$26.1^{+1.6}_{-1.7}$	1.12 (307)
9	$2.30^{+0.03}_{-0.03}$	$16.6^{+1.1}_{-1.2}$	$111.7^{+1.3}_{-1.3}$	$25.2^{+0.5}_{-0.5}$	$23.8^{+1.8}_{-1.8}$	1.25 (312)
10	$2.30^{+0.04}_{-0.04}$	$17.6^{+1.4}_{-1.3}$	$110.0^{+1.5}_{-1.5}$	$25.9^{+0.5}_{-0.6}$	$24.5^{+2.0}_{-2.2}$	1.05 (319)
	Γ	norm[a]	kT[b]	norm[c]	CF %	χ^2 (d.o.f.)
11	$2.00^{+0.02}_{-0.06}$	$4.27^{+1.66}_{-0.62}$	$114.6^{+3.3}_{-3.5}$	$11.71^{+0.34}_{-0.35}$	$13.8^{+3.5}_{-6.6}$	1.11 (323)
12	$2.16^{+0.25}_{-0.19}$	$3.80^{+2.88}_{-1.39}$	$92.8^{+10.9}_{-10.6}$	$4.83^{+0.68}_{-0.52}$	$69.0^{+3.9}_{-4.6}$	1.12 (268)
13	$2.12^{+0.15}_{-0.08}$	$4.12^{+1.56}_{-8.16}$	$115.9^{+5.2}_{-4.9}$	$5.77^{+0.25}_{-0.33}$	$35.1^{+3.4}_{-4.0}$	1.13 (315)
14	$2.17^{+0.15}_{-0.06}$	$3.94^{+0.12}_{-0.96}$	$93.0^{+2.5}_{-5.6}$	$4.55^{+0.24}_{-0.26}$	$65.4^{+6.7}_{-4.4}$	1.02 (320)
15	$2.01^{+0.06}_{-0.08}$	$1.95^{+0.07}_{-0.43}$	$100.6^{+4.1}_{-4.8}$	$6.34^{+0.31}_{-0.30}$	$23.0^{+8.0}_{-9.4}$	1.04 (317)
16	2.1 (fixed)	$1.03^{+0.04}_{-0.04}$	$86.3^{+4.0}_{-3.8}$	$4.96^{+0.30}_{-0.25}$	-	1.09 (295)

Notes. [a] Units 10^{-3} photons keV^{-1} cm^{-2} sec^{-1}. [b] Units in eV. [c] Units in 10^{-5} L_{39}/D_{10}^2 where L_{39} is the luminosity in 10^{39} ergs sec^{-1} and D_{10} is the distance in 10 kpc.

Table 9: Atomic feature final model fit parameters

	Fe $K\alpha$[a]	σ_{Fe} [b]	Line Flux[c]	O VIII[a]	Line Flux[c]	Edge[d]	τ
1	$6.33^{+0.04}_{-0.03}$	-	$2.82^{+0.86}_{-0.94}$	$0.63^{+0.01}_{-0.01}$	$4.29^{+0.79}_{-0.86}$	$0.75^{+0.01}_{-0.02}$	$0.13^{+0.02}_{-0.02}$
2	$6.34^{+0.06}_{-0.08}$	$117.5^{+156.7}_{-79.9}$	$3.60^{+1.07}_{-1.91}$	$0.63^{+0.01}_{-0.02}$	$3.64^{+0.76}_{-0.74}$	$0.74^{+0.01}_{-0.02}$	$0.13^{+0.02}_{-0.02}$
3	$6.38^{+0.07}_{-0.10}$	< 753	$1.47^{+1.06}_{-0.72}$	$0.65^{+0.01}_{-0.02}$	$2.76^{+0.67}_{-0.65}$	$0.76^{+0.01}_{-0.02}$	$0.15^{+0.02}_{-0.02}$
4	$6.46^{+0.03}_{-0.04}$	< 77	$2.07^{+0.74}_{-0.61}$	$0.62^{+0.01}_{-0.02}$	$1.68^{+0.58}_{-0.50}$	$0.75^{+0.01}_{-0.01}$	$0.23^{+0.03}_{-0.03}$
5	$6.38^{+0.03}_{-0.03}$	< 63	$2.20^{+0.76}_{-0.63}$	$0.62^{+0.01}_{-0.01}$	$3.39^{+0.55}_{-0.54}$	$0.76^{+0.01}_{-0.02}$	$0.24^{+0.02}_{-0.03}$
6	$6.37^{+0.04}_{-0.04}$	< 101	$1.93^{+0.61}_{-0.68}$	$0.61^{+0.01}_{-0.03}$	$1.06^{+0.36}_{-0.30}$	$0.73^{+0.01}_{-0.01}$	$0.32^{+0.04}_{-0.04}$
7	$6.39^{+0.05}_{-0.06}$	< 129	$1.66^{+0.80}_{-0.74}$	$0.61^{+0.02}_{-0.02}$	$2.84^{+0.74}_{-0.61}$	$0.75^{+0.01}_{-0.02}$	$0.13^{+0.02}_{-0.02}$
8	$6.38^{+0.06}_{-0.07}$	$166.0^{+79.8}_{-61.2}$	$5.07^{+1.71}_{-1.32}$	$0.63^{+0.02}_{-0.02}$	$3.50^{+0.69}_{-0.94}$	$0.79^{+0.03}_{-0.04}$	$0.09^{+0.02}_{-0.02}$
9	$6.31^{+0.06}_{-0.07}$	< 221	$3.12^{+1.57}_{-0.97}$	$0.63^{+0.02}_{-0.02}$	$2.26^{+0.79}_{-0.74}$	$0.75^{+0.02}_{-0.02}$	$0.10^{+0.02}_{-0.02}$
10	$6.43^{+0.22}_{-0.20}$	< 532	$3.51^{+2.22}_{-1.97}$	$0.63^{+0.01}_{-0.02}$	$2.92^{+0.79}_{-0.79}$	$0.74^{+0.02}_{-0.02}$	$0.08^{+0.02}_{-0.02}$
	Fe $K\alpha$[a]	σ_{Fe} [b]	Line Flux[c]	O VII[a]	Line Flux[c]	Edge[d]	τ
11	$6.38^{+0.05}_{-0.02}$	< 147.6	$1.52^{+0.88}_{-0.64}$	-	-	$0.72^{+0.01}_{-0.01}$	$0.38^{+0.06}_{-0.06}$
12	$6.45^{+0.09}_{-0.10}$	< 156.6	$1.73^{+0.11}_{-0.10}$	$0.55^{+0.02}_{-0.02}$	$2.47^{+1.02}_{-1.03}$	$0.74^{+0.02}_{-0.02}$	$0.55^{+0.17}_{-0.27}$
13	$6.45^{+0.06}_{-0.06}$	< 138.0	$1.45^{+0.70}_{-0.65}$	-	-	$0.70^{+0.02}_{-0.01}$	$0.38^{+0.07}_{-0.04}$
14	$6.40^{+0.03}_{-0.03}$	< 110.5	$1.53^{+0.49}_{-0.47}$	$0.56^{+0.01}_{-0.01}$	$1.46^{+0.52}_{-0.42}$	$0.72^{+0.01}_{-0.01}$	$0.58^{+0.17}_{-0.12}$
15	$6.44^{+0.06}_{-0.06}$	< 180.7	$1.66^{+0.82}_{-0.69}$	-	-	$0.73^{+0.01}_{-0.01}$	$0.53^{+0.12}_{-0.15}$
16	$6.45^{+0.04}_{-0.04}$	$138.1^{+75.8}_{-46.0}$	$2.17^{+0.64}_{-0.51}$	$0.56^{+0.01}_{-0.01}$	$1.82^{+0.32}_{-0.45}$	$0.73^{+0.02}_{-0.01}$	$0.38^{+0.11}_{-0.16}$

Notes. [a] Line Energy in units of keV. [b] Line width in units of eV. [c] Flux in line, units of photons cm^{-2} sec^{-1}. [d] Edge energy in units of keV.

Table 10: Thermal plasma model parameters. 2002 data only.

	kT[a]	norm[b]
11	-	-
12	$0.71^{+0.08}_{-0.06}$	$4.16^{+2.30}_{-1.38}$
13	-	-
14	$0.67^{+0.03}_{-0.04}$	$4.01^{+1.68}_{-0.73}$
15	$0.69^{+0.04}_{-0.05}$	$3.41^{+1.03}_{-0.95}$
16	$0.72^{+0.03}_{-0.03}$	$3.89^{+0.43}_{-0.75}$

Notes. [a] Mekal plasma temp in units of keV. [b] Mekal normalization, see Appendix A for definition.

APPENDIX C

MRK 766 RGS PARAMETER TABLES

Listed in the following tables are numerous atomic features seen in the RGS data of Mrk 766. These include the relativistically broadened emission lines, narrow emission lines and narrow absorption lines.

Table 11: Table of relativistically broadened emission lines. Line energies are fixed at their respective laboratory values.

	Rev 82		Rev 265		Rev 999	
Line	Flux[a]	EW[b]	Flux[a]	EW[b]	Flux[a]	EW[b]
C VI Lyα	$2.13^{+0.24}_{-0.24}$	$28.7^{+5.6}_{-5.3}$	$2.59^{+0.20}_{-0.20}$	$18.1^{+2.2}_{-2.3}$	$1.23^{+0.14}_{-0.14}$	$51.4^{+12.5}_{-9.5}$
N VII Lyα	$2.90^{+0.22}_{-0.22}$	$74.1^{+9.4}_{-9.0}$	$4.62^{+0.17}_{-0.17}$	$59.6^{+4.2}_{-2.6}$	$1.18^{+0.11}_{-0.11}$	$83.1^{+16.6}_{-16.8}$
O VIII Lyα	$2.46^{+0.19}_{-0.19}$	$83.6^{+12.8}_{-9.8}$	$4.68^{+0.15}_{-0.15}$	$84.1^{+4.1}_{-4.3}$	$1.06^{+0.10}_{-0.09}$	$125.1^{+24.9}_{-18.4}$

Notes. [a] Flux in line, units of 10^{-3} photons cm^{-2} sec^{-1}. [b] Equivalent width in units of eV.

Table 11 continued

	Rev 1000		Rev 1001		Rev 1002	
Line	Flux[a]	EW[b]	Flux[a]	EW[b]	Flux[a]	EW[b]
C VI Lyα	$1.10^{+0.15}_{-0.16}$	$21.4^{+6.9}_{-6.1}$	$1.65^{+0.17}_{-0.18}$	$25.1^{+4.2}_{-4.8}$	$1.81^{+0.17}_{-0.17}$	$22.3^{+3.7}_{-2.8}$
N VII Lyα	$1.22^{+0.13}_{-0.12}$	$41.5^{+8.4}_{-9.1}$	$1.56^{+0.13}_{-0.13}$	$41.7^{+6.2}_{-5.8}$	$1.75^{+0.14}_{-0.14}$	$39.0^{+4.9}_{-5.6}$
O VIII Lyα	$1.33^{+0.12}_{-0.11}$	$68.1^{+11.1}_{-11.9}$	$1.71^{+0.12}_{-0.12}$	$66.0^{+9.7}_{-6.9}$	$2.02^{+0.12}_{-0.12}$	$95.5^{+9.3}_{-9.7}$

Notes. [a] Flux in line, units of 10^{-3} photons cm^{-2} sec^{-1}. [b] Equivalent width in units of eV.

Table 11 continued

	Rev 1003	
Line	Flux[a]	EW[b]
C VI Lyα	$1.36^{+0.18}_{-0.18}$	$19.6^{+4.8}_{-5.2}$
N VII Lyα	$1.39^{+0.14}_{-0.14}$	$34.8^{+5.2}_{-7.2}$
O VIII Lyα	$1.43^{+0.13}_{-0.13}$	$52.0^{+10.1}_{-6.5}$

Notes. [a] Flux in line, units of 10^{-3} photons cm^{-2} sec^{-1}. [b] Equivalent width in units of eV.

Table 12: Table for O VII forbidden line. Mrk 766 shows a strong O VII forbidden line in all observations. Wavelength of source, line flux and the equivalent width are shown for each observation.

	$\lambda^{a}{}_{\rm source}$	Flux[b]	EW[c]
Rev 82	$22.09^{+0.01}_{-0.01}$	$5.88^{+2.82}_{-2.27}$	$2.0^{+1.3}_{-1.5}$
Rev 265	$22.09^{+0.01}_{-0.03}$	$3.27^{+1.80}_{-1.70}$	$5.5^{+7.7}_{-5.4}$
Rev 999	$22.10^{+0.03}_{-0.00}$	$5.07^{+1.08}_{-1.39}$	$5.7^{+3.1}_{-2.5}$
Rev 1000	$22.08^{+0.01}_{-0.01}$	$5.86^{+1.38}_{-1.37}$	$3.1^{+1.3}_{-1.5}$
Rev 1001	$22.09^{+0.01}_{-0.02}$	$5.10^{+1.86}_{-1.23}$	$2.0^{+1.1}_{-1.3}$
Rev 1002	$22.10^{+0.02}_{-0.00}$	$3.93^{+1.59}_{-1.59}$	$1.2^{+1.3}_{-0.9}$
Rev 1003	$22.08^{+0.01}_{-0.03}$	$4.14^{+2.15}_{-1.16}$	< 2.5

Notes. [a] Wavelength, in units Å. [b] Flux in line, in units of 10^{-5} photons cm^{-2} sec^{-1}. [c] Equivalent width in units of eV.

Table 13: Table of other narrow lines seen in Mrk 766. Several lines make inconsistent appearence in the RGS spectra of Mrk 766. Listed are the observations the detection is made from, line identity, wavelength of source, laboratory wavelength, line flux and the equivalent width.

Obs	Line	$\lambda_{\rm source}$	$\lambda_{\rm lab}$	Flux[a]	EW[b]
Rev 265	C V 1s-2p	$33.73^{+0.03}_{-0.02}$	33.73	$7.38^{+2.60}_{-3.15}$	< 8.4
Rev 999	O VII 1s-2p (i)	$21.75^{+0.01}_{-0.02}$	21.80	$2.56^{+1.46}_{-0.71}$	$2.7^{+2.7}_{-2.2}$
Rev 999	N VI 1s-2s	$29.52^{+0.73}_{-0.02}$	29.53	$3.10^{+1.37}_{-1.05}$	$1.6^{+1.4}_{-1.5}$
Rev 999	Ne IX 1s-2p (f)	$13.67^{+0.04}_{-0.04}$	13.70	$0.89^{+0.34}_{-0.53}$	$4.5^{+4.4}_{-4.4}$
Rev 1003	Ne IX 1s-2p (f)	$13.70^{+0.00}_{-0.01}$	13.70	$2.05^{+0.41}_{-1.24}$	$3.1^{+1.5}_{-2.3}$

Table 14: Absorption column densities. A large number of narrow absorption lines are seen in every observation. Listed are the measured column densities for each species in each observation.

Line	Rev 82[a]	Rev 265[a]	Rev 999[a]	Rev 1000[a]
C V	$9.96^{+27.54}_{-5.93}\ 10^{14}$	-	$1.37^{+1.67}_{-1.10}\ 10^{15}$	$1.56^{+1.26}_{-1.16}\ 10^{15}$
C VI	$1.26^{+1.34}_{-0.90}\ 10^{15}$	$2.42^{+1.57}_{-71.66}\ 10^{15}$	-	$2.39^{+5.23}_{-1.44}\ 10^{15}$
N VI	$3.96^{+0.62}_{-0.91}\ 10^{16}$	-	-	-
N VII	$2.60^{+5.81}_{-1.20}\ 10^{15}$	$6.23^{+3.51}_{-2.18}\ 10^{15}$	$9.19^{+22.00}_{-8.64}\ 10^{16}$	-
O VII	$2.46^{+4.32}_{-1.76}\ 10^{15}$	$7.14^{+15.03}_{-2.59}\ 10^{15}$	-	-
O VIII	-	$1.81^{+1.96}_{-0.81}\ 10^{16}$	-	-
Ne IX	-	$3.76^{+16.87}_{-3.51}\ 10^{15}$	-	$1.90^{+61.68}_{-1.68}\ 10^{17}$
Fe IX	-	$8.50^{+47.38}_{-3.35}\ 10^{15}$	-	-
Fe X	$1.41^{+20.19}_{-1.34}\ 10^{16}$	-	-	$2.26^{+6.48}_{-1.20}\ 10^{16}$
Fe IX	-	$3.26^{+177.65}_{-6.13}\ 10^{17}$	-	-
Fe XII	-	$2.27^{+29.09}_{-1.95}\ 10^{17}$	$8.41^{+358}_{-7.88}\ 10^{16}$	$5.92^{+16.76}_{-3.34}\ 10^{16}$
Fe XIII	$2.34^{+58.83}_{-2.09}\ 10^{16}$	-	$9.45^{+666}_{-9.15}\ 10^{17}$	$9.43^{+20.69}_{-6.73}\ 10^{15}$
Fe XIV	-	-	-	-
Fe XV	-	-	$9.80^{+206}_{-9.73}\ 10^{18}$	-
Fe XVII	$9.99^{+250}_{--9.73}\ 10^{16}$	$3.20^{+7.08}_{-2.17}\ 10^{15}$	-	$1.98^{+1149}_{-0.87}\ 10^{15}$
Fe XVIII	$2.89^{+177}_{-280}\ 10^{17}$	$1.95^{+15.80}_{-1.42}\ 10^{16}$	-	$1.08^{+1.62}_{-0.61}\ 10^{16}$
Fe XXI	-	$1.97^{+14.72}_{-1.43}\ 10^{16}$	$1.89^{+89.60}_{-1.86}\ 10^{18}$	$7.19^{+11.96}_{-4.18}\ 10^{15}$

Notes. [a] Column density in units of cm^{-2}.

Table 14 continued

Line	Rev 1001[a]	Rev 1002[a]	Rev 1003[a]
C V	-	$1.69^{+7.46}_{-1.17}\ 10^{15}$	-
C VI	-	$6.49^{+49.94}_{-3.11}\ 10^{14}$	$3.28^{+60.08}_{-2.82}\ 10^{14}$
N VI	-	-	$< 1.41\ 10^{16}$
N VII	$2.11^{+1.88}_{-1.00}\ 10^{15}$	$2.98^{+10.15}_{-1.31}\ 10^{15}$	$1.96^{+1.88}_{-1.14}\ 10^{15}$
O VII	-	-	$5.33^{+9.46}_{-3.04}\ 10^{15}$
O VIII	$4.72^{+3.39}_{-3.90}\ 10^{15}$	-	$6.47^{+6.04}_{-4.75}\ 10^{15}$
Ne IX	-	-	$4.06^{+101}_{-3.40}\ 10^{16}$
Fe IX	$6.84^{+13.99}_{-4.11}\ 10^{15}$	$2.56^{+39.33}_{-1.92}\ 10^{16}$	-
Fe X	$5.06^{+21.64}_{-3.58}\ 10^{16}$	$1.64^{+14.76}_{-1.18}\ 10^{16}$	$2.22^{+41.93}_{-1.87}\ 10^{17}$
Fe IX	$1.09^{+1.94}_{-0.91}\ 10^{16}$	$2.08^{+8.99}_{-1.52}\ 10^{16}$	-
Fe XII	-	$1.43^{+49.82}_{-1.18}\ 10^{17}$	$6.26^{+32.36}_{-4.55}\ 10^{16}$
Fe XIII	$9.70^{+54.04}_{-6.44}\ 10^{16}$	$2.87^{+103}_{-2.55}\ 10^{17}$	$4.63^{+25.28}_{-2.94}\ 10^{16}$
Fe XIV	-	$9.34^{+337}_{-7.50}\ 10^{16}$	-
Fe XV	-	-	-
Fe XVII	$7.03^{+66.52}_{-3.13}\ 10^{16}$	$5.98^{+106}_{-5.63}\ 10^{16}$	$1.09^{+47.78}_{-9.94}\ 10^{17}$
Fe XVIII	$1.33^{+3.27}_{-0.83}\ 10^{16}$	$3.22^{+398}_{-3.17}\ 10^{19}$	$2.57^{+28.21}_{-2.00}\ 10^{16}$
Fe XXI	-	$1.18^{+148}_{-1.12}\ 10^{18}$	$4.24^{+32.71}_{-3.46}\ 10^{16}$

Notes. [a] Column density in units of cm^{-2}.

APPENDIX D

MRK 766 EPIC PARAMETER TABLES

EPIC model parameters for Mrk 766. Only free parameters are shown here. Fixed parameters and model components are discussed in Chapter 6. Continuum model, Table 15, consists of a Power Law Component (PLC), a Reflection Dominated Component (RDC) and a component partially covered by a partially ionized cloud. Atomic features, Table 16, are a narrow Fe Kα line, an additional narrow emission line and an absorption edge.

Table 15: Continuum model parameters.

Rev 82	PLC norm[a]	q[b]	ξ[c]	RDC norm[d]	χ^2 (dof)
1	$9.02^{+0.22}_{-0.22}$	$3.64^{+0.80}_{-1.07}$	$252.2^{+28.9}_{-25.4}$	$1.33^{+0.20}_{-0.20}$	328.48(360)
2	$7.55^{+0.13}_{-0.13}$	$3.11^{+0.47}_{-0.43}$	$224.2^{+16.3}_{-15.2}$	$1.87^{+0.22}_{-0.23}$	316.44(366)
3	$5.48^{+0.11}_{-0.11}$	$3.93^{+0.42}_{-0.37}$	$285.1^{+16.3}_{-15.6}$	$2.03^{+0.14}_{-0.14}$	359.39(351)
4	$5.66^{+0.11}_{-0.11}$	$2.72^{+1.23}_{-1.25}$	$224.6^{+6.2}_{-6.0}$	$3.39^{+0.16}_{-0.16}$	324.92(331)
5	$6.31^{+0.09}_{-0.09}$	$3.23^{+0.19}_{-0.17}$	$199.9^{+3.5}_{-6.9}$	$5.00^{+0.19}_{-0.19}$	322.17(344)
6	$6.48^{+0.12}_{-0.12}$	$3.86^{+0.28}_{-0.25}$	$200.1^{+4.4}_{-8.5}$	$6.19^{+0.29}_{-0.30}$	375.44(338)
7	$8.72^{+0.16}_{-0.16}$	$3.58^{+0.43}_{-0.38}$	$200.1^{+7.5}_{-13.2}$	$4.64^{+0.36}_{-0.36}$	337.27(343)
8	$7.33^{+0.14}_{-0.14}$	$3.45^{+0.38}_{-0.32}$	$202.3^{+6.8}_{-8.6}$	$4.48^{+0.30}_{-0.30}$	358.76(344)
9	$8.03^{+0.19}_{-0.19}$	$3.79^{+0.58}_{-0.49}$	$306.3^{+23.5}_{-21.9}$	$2.50^{+0.21}_{-0.21}$	373.42(343)

Rev 82	n_H[e]	ξ[f]	CF %[g]	Soft Flux[h]	Hard Flux[i]
1	$0.96^{+0.28}_{-0.26}$	$1.73^{+0.19}_{-0.20}$	$52.8^{+7.3}_{-7.7}$	$2.41^{+0.08}_{-0.08}$	$3.02^{+0.07}_{-0.05}$
2	$0.78^{+0.12}_{-0.11}$	$1.25^{+0.11}_{-0.10}$	$56.6^{+13.7}_{-13.9}$	$1.88^{+0.04}_{-0.04}$	$2.56^{+0.03}_{-0.04}$
3	$0.80^{+0.16}_{-0.14}$	$1.09^{+0.12}_{-0.14}$	$43.8^{+3.8}_{-3.8}$	$1.60^{+0.04}_{-0.03}$	$1.98^{+0.03}_{-0.03}$
4	$1.04^{+0.15}_{-0.11}$	$1.09^{+0.07}_{-0.07}$	$56.0^{+12.6}_{-12.6}$	$1.65^{+0.03}_{-0.03}$	$2.03^{+0.03}_{-0.03}$
5	$0.78^{+0.17}_{-0.17}$	$1.10^{+0.06}_{-0.06}$	$58.6^{+12.3}_{-12.4}$	$1.84^{+0.03}_{-0.03}$	$2.22^{+0.03}_{-0.03}$
6	$0.40^{+0.50}_{-0.57}$	$1.23^{+0.10}_{-0.10}$	$70.9^{+15.2}_{-15.4}$	$2.11^{+0.04}_{-0.04}$	$2.35^{+0.03}_{-0.04}$
7	$0.67^{+0.16}_{-0.13}$	$1.60^{+0.20}_{-0.16}$	$53.7^{+6.1}_{-6.3}$	$2.57^{+0.05}_{-0.06}$	$2.97^{+0.05}_{-0.03}$
8	$0.36^{+0.55}_{-0.55}$	$1.24^{+0.11}_{-0.11}$	$48.9^{+6.0}_{-6.2}$	$2.21^{+0.04}_{-0.06}$	$2.58^{+0.05}_{-0.03}$
9	$0.84^{+0.93}_{-0.67}$	$1.14^{+1.73}_{-1.55}$	< 49.1	$2.65^{+0.07}_{-0.07}$	$2.85^{+0.03}_{-0.04}$

Notes. [a] Power law normalization, with units of photons keV^{-1} cm^{-2} sec^{-1} at 1 keV. [b] Emissivity index. [c] Ionization parameter, see Ross & Fabian (2005). [d] REFLION normalization, see Ross & Fabian (2005). [e] Partial covering neutral hydrogen column density in units of atoms cm^{-2}. [f] Ionization parameter, see Tarter et al. (1969). [g] Covering Fraction. [h] Flux from 0.3-2.0 keV in units of 10^{-2} photons cm^{-2} sec^{-1}. [i] Flux from 2.0-10.0 keV in units of 10^{-3} photons cm^{-2} sec^{-1}.

Table 15 continued

Rev 265	PLC norm[a]	q[b]	ξ[c]	RDC norm[d]	χ^2 (dof)
10	$10.56^{+0.11}_{-0.11}$	$3.20^{+0.17}_{-0.16}$	$235.0^{+4.9}_{-4.8}$	$4.90^{+0.16}_{-0.16}$	408.92 (330)
11	$13.27^{+0.15}_{-0.15}$	$3.61^{+0.20}_{-0.20}$	$386.9^{+16.6}_{-16.0}$	$2.95^{+0.11}_{-0.11}$	396.72 (334)
12	$9.65^{+0.12}_{-0.12}$	$3.34^{+0.16}_{-0.15}$	$360.4^{+60.6}_{-55.6}$	$2.00^{+0.15}_{-0.21}$	368.34 (307)
13	$10.65^{+0.14}_{-0.14}$	$3.55^{+0.24}_{-0.22}$	$360.4^{+14.5}_{-14.0}$	$3.20^{+0.12}_{-0.12}$	375.77 (334)
14	$13.71^{+0.14}_{-0.14}$	$3.38^{+0.25}_{-0.22}$	$202.5^{+4.6}_{-6.7}$	$6.13^{+0.28}_{-0.29}$	369.48 (342)
15	$10.52^{+0.14}_{-1.39}$	$3.92^{+0.32}_{-0.28}$	$226.2^{+6.1}_{-6.0}$	$5.78^{+0.25}_{-0.28}$	347.16 (336)
16	$9.14^{+0.09}_{-0.09}$	$3.55^{+0.17}_{-0.16}$	$254.6^{+6.1}_{-6.0}$	$3.08^{+0.10}_{-0.10}$	407.02 (341)
17	$11.80^{+0.25}_{-0.25}$	$3.35^{+0.83}_{-0.52}$	< 400.1	$1.66^{+0.69}_{-0.62}$	335.53 (327)
18	$12.09^{+0.18}_{-0.21}$	$3.61^{+0.92}_{-0.92}$	< 547.0	< 8.25	345.11 (330)
19	$10.68^{+0.14}_{-0.14}$	$3.48^{+0.39}_{-0.31}$	$321.4^{+18.7}_{-17.7}$	$2.19^{+0.14}_{-0.13}$	333.51 (343)
20	$13.82^{+0.14}_{-0.14}$	$3.61^{+0.26}_{-0.26}$	$215.1^{+6.9}_{-6.7}$	$3.51^{+0.20}_{-0.20}$	362.52 (349)
21	$9.83^{+0.10}_{-0.10}$	$3.69^{+0.22}_{-0.20}$	$208.4^{+3.7}_{-3.7}$	$6.36^{+0.22}_{-0.22}$	364.03 (333)
22	$14.76^{+0.15}_{-0.15}$	$3.18^{+0.42}_{-0.39}$	$223.0^{+10.8}_{-10.3}$	$2.77^{+0.22}_{-0.22}$	319.23 (352)
23	$13.07^{+0.18}_{-0.18}$	$3.22^{+0.55}_{-0.51}$	$249.7^{+17.5}_{-16.3}$	$2.36^{+0.23}_{-0.23}$	372.50 (352)
24	$10.50^{+0.15}_{-0.15}$	$3.15^{+0.31}_{-0.30}$	$385.2^{+24.7}_{-23.2}$	$2.00^{+0.11}_{-0.11}$	358.48 (340)
25	$11.27^{+0.15}_{-0.15}$	$3.35^{+0.62}_{-0.53}$	$258.1^{+19.8}_{-18.5}$	$1.84^{+0.19}_{-0.19}$	402.19 (357)
26	$11.86^{+0.20}_{-0.18}$	$3.42^{+0.45}_{-0.39}$	$321.8^{+21.5}_{-19.9}$	$2.41^{+0.16}_{-0.17}$	363.88 (342)
27	$11.75^{+0.19}_{-0.19}$	$3.42^{+0.44}_{-0.37}$	$336.8^{+23.3}_{-23.3}$	$2.28^{+0.15}_{-0.17}$	288.95 (302)
28	$10.40^{+0.11}_{-0.11}$	$3.43^{+0.27}_{-0.24}$	$328.9^{+14.3}_{-13.7}$	$2.36^{+0.10}_{-0.11}$	367.90 (336)

Rev 265	n_H[e]	ξ[f]	CF %[g]	Soft Flux[h]	Hard Flux[i]
10	$0.91^{+0.22}_{-0.21}$	$1.90^{+0.14}_{-0.16}$	$31.9^{+13.8}_{-13.7}$	$3.65^{+0.05}_{-0.04}$	$3.70^{+0.03}_{-0.02}$
11	$0.34^{+0.62}_{-0.05}$	$1.88^{+2.53}_{-1.87}$	$26.9^{+33.9}_{-23.8}$	$4.70^{+0.05}_{-0.06}$	$4.71^{+0.03}_{-0.03}$
12	0.50 fixed	1.73 fixed	47.7 fixed	$4.68^{+0.03}_{-0.03}$	$3.96^{+0.05}_{-0.05}$
13	$0.50^{+0.09}_{-0.08}$	$1.73^{+0.13}_{-0.13}$	$47.2^{+5.1}_{-5.2}$	$3.69^{+0.05}_{-0.06}$	$3.81^{+0.03}_{-0.03}$
14	$0.36^{+0.10}_{-0.09}$	$1.10^{+0.20}_{-0.29}$	$30.0^{+14.0}_{-14.1}$	$4.21^{+0.05}_{-0.05}$	$4.66^{+0.04}_{-0.03}$
15	$0.29^{+0.08}_{-0.06}$	$1.14^{+0.20}_{-0.16}$	$37.4^{+5.2}_{-5.3}$	$3.46^{+0.05}_{-0.06}$	$3.70^{+0.02}_{-0.03}$
16	$0.28^{+0.02}_{-0.02}$	$1.74^{+0.07}_{-0.07}$	$40.7^{+20.9}_{-17.8}$	$2.96^{+0.03}_{-0.03}$	$3.21^{+0.02}_{-0.02}$
17	0.92 fixed	1.73 fixed	35.6 fixed	$4.07^{+0.28}_{-0.26}$	$4.00^{+0.14}_{-0.10}$
18	0.92 fixed	1.73 fixed	35.6 fixed	$3.90^{+0.04}_{-0.05}$	$3.93^{+0.05}_{-0.05}$
19	$0.92^{+0.24}_{-0.19}$	$1.72^{+0.15}_{-0.15}$	$35.1^{+4.0}_{-4.1}$	$3.20^{+0.04}_{-0.05}$	$3.67^{+0.03}_{-0.03}$
20	$0.25^{+0.02}_{-0.02}$	$1.84^{+0.24}_{-0.21}$	< 86.9	$4.11^{+0.05}_{-0.04}$	$4.62^{+0.04}_{-0.04}$
21	$0.27^{+0.06}_{-0.05}$	$1.44^{+0.14}_{-0.14}$	$46.4^{+5.6}_{-5.8}$	$3.28^{+0.04}_{-0.04}$	$3.45^{+0.03}_{-0.03}$
22	$0.27^{+0.31}_{-0.20}$	$1.95^{+0.74}_{-0.48}$	$25.6^{+25.8}_{-10.4}$	$4.28^{+0.07}_{-0.06}$	$4.95^{+0.04}_{-0.05}$
23	$0.53^{+0.15}_{-0.12}$	$2.13^{+0.17}_{-0.16}$	$55.7^{+8.4}_{-18.4}$	$3.74^{+0.05}_{-0.06}$	$4.40^{+0.04}_{-0.04}$
24	$0.63^{+0.18}_{-0.14}$	$1.66^{+0.19}_{-0.19}$	$36.4^{+5.2}_{-5.3}$	$3.31^{+0.06}_{-0.05}$	$3.66^{+0.03}_{-0.04}$
25	$0.54^{+0.08}_{-0.07}$	$1.65^{+0.11}_{-0.11}$	$61.7^{+15.2}_{-15.4}$	$3.02^{+0.05}_{-0.05}$	$3.78^{+0.04}_{-0.06}$
26	$0.28^{+1.22}_{-0.27}$	$1.92^{+0.47}_{-0.20}$	< 64.4	$3.76^{+0.05}_{-0.06}$	$4.13^{+0.05}_{-0.05}$
27	< 0.70	$2.10^{+0.58}_{-0.46}$	$19.2^{+29.7}_{-10.7}$	$3.73^{+0.07}_{-0.05}$	$4.09^{+0.04}_{-0.03}$
28	< 0.70	$2.16^{+0.35}_{-0.35}$	$17.2^{+23.3}_{-16.1}$	$3.39^{+0.04}_{-0.04}$	$3.67^{+0.03}_{-0.02}$

Table 15 continued

Rev 999	PLC norm[a]	q[b]	ξ[c]	RDC norm[d]	χ^2 (dof)
29	$3.26^{+0.09}_{-0.09}$	$4.06^{+0.14}_{-0.14}$	$182.7^{+4.4}_{-5.2}$	$3.41^{+0.10}_{-0.10}$	329.18 (315)
30	$3.21^{+0.08}_{-0.08}$	$4.10^{+0.17}_{-0.17}$	$216.5^{+3.5}_{-3.5}$	$1.93^{+0.06}_{-0.06}$	306.30 (320)
31	$5.38^{+0.09}_{-0.09}$	$4.08^{+0.75}_{-0.55}$	$129.5^{+8.3}_{-7.9}$	$1.23^{+0.15}_{-0.15}$	339.94 (361)
32	$5.37^{+0.07}_{-0.07}$	$4.05^{+0.31}_{-0.29}$	$114.1^{+2.4}_{-2.4}$	$3.30^{+0.19}_{-0.20}$	432.41 (354)
33	$3.98^{+0.11}_{-0.11}$	$4.07^{+0.30}_{-0.29}$	$198.0^{+7.0}_{-10.9}$	$1.57^{+0.10}_{-0.10}$	296.78 (352)
34	$3.30^{+0.10}_{-0.10}$	$4.06^{+0.15}_{-0.14}$	$214.1^{+2.9}_{-2.9}$	$2.62^{+0.07}_{-0.08}$	323.78 (316)

Rev 999	n_H[e]	ξ[f]	CF %[g]	Soft Flux[h]	Hard Flux[i]
29	$23.00^{+3.35}_{-1.71}$	$1.65^{+0.19}_{-0.19}$	$71.9^{+1.8}_{-1.9}$	$0.55^{+0.01}_{-0.01}$	$0.71^{+0.02}_{-0.02}$
30	$18.83^{+1.32}_{-1.26}$	$1.92^{+0.05}_{-0.16}$	$71.3^{+1.7}_{-1.8}$	$0.58^{+0.02}_{-0.02}$	$0.77^{+0.02}_{-0.02}$
31	$12.28^{+0.70}_{-0.67}$	$1.95^{+0.02}_{-0.02}$	$73.7^{+1.1}_{-1.1}$	$0.67^{+0.01}_{-0.01}$	$1.22^{+0.02}_{-0.02}$
32	$8.82^{+0.47}_{-0.87}$	$1.81^{+0.04}_{-0.04}$	$66.4^{+0.9}_{-0.9}$	$0.84^{+0.01}_{-0.01}$	$1.40^{+0.02}_{-0.02}$
33	$13.83^{+1.78}_{-1.13}$	$1.90^{+0.04}_{-0.10}$	$70.1^{+1.8}_{-2.0}$	$0.59^{+0.01}_{-0.02}$	$0.95^{+0.02}_{-0.02}$
34	$22.06^{+2.83}_{-1.67}$	$1.57^{+0.18}_{-0.18}$	$73.6^{+1.8}_{-1.9}$	$0.55^{+0.01}_{-0.01}$	$0.72^{+0.02}_{-0.02}$

Table 15 continued

Rev 1000	PLC norm[a]	q[b]	ξ[c]	RDC norm[d]	χ^2 (dof)
35	$4.03^{+0.10}_{-0.10}$	$3.89^{+0.29}_{-0.27}$	$116.5^{+3.4}_{-3.3}$	$3.58^{+0.28}_{-0.29}$	325.97 (354)
36	$2.65^{+0.09}_{-0.09}$	$3.94^{+0.19}_{-0.18}$	$166.6^{+4.36}_{-4.51}$	$2.84^{+0.10}_{-0.11}$	352.35 (327)
37	$3.79^{+0.08}_{-0.08}$	$3.58^{+0.19}_{-0.18}$	$102.5^{+1.3}_{-1.4}$	$1.09^{+0.65}_{-0.67}$	326.43 (345)
38	$7.36^{+0.07}_{-0.07}$	$3.59^{+0.62}_{-0.50}$	$90.3^{+9.78}_{-9.15}$	$4.99^{+0.65}_{-0.66}$	404.68 (378)
39	$5.01^{+0.08}_{-0.07}$	$4.05^{+0.74}_{-0.58}$	$235.8^{+15.4}_{-14.5}$	$1.33^{+0.13}_{-0.14}$	410.60 (361)
40	$7.28^{+0.08}_{-0.08}$	$3.99^{+1.29}_{-0.98}$	$198.3^{+21.8}_{-35.2}$	$0.93^{+0.20}_{-0.20}$	473.78 (366)
41	$5.74^{+0.07}_{-0.07}$	$3.91^{+0.58}_{-0.48}$	$202.5^{+9.7}_{-15.8}$	$1.62^{+0.16}_{-0.16}$	424.42 (368)
42	$4.52^{+0.07}_{-0.07}$	$4.01^{+2.55}_{-1.89}$	$374.8^{+80.8}_{-73.3}$	$0.99^{+0.69}_{-0.77}$	426.03 (368)
43	$4.51^{+0.05}_{-0.05}$	$4.10^{+0.68}_{-0.58}$	$225.2^{+13.4}_{-13.2}$	$0.99^{+0.10}_{-0.10}$	386.89 (362)
44	$6.65^{+0.09}_{-0.10}$	$3.47^{+0.88}_{-0.26}$	$107.8^{+4.34}_{-4.13}$	$4.95^{+0.52}_{-0.51}$	358.29 (366)

Rev 1000	n_H[e]	ξ[f]	CF %[g]	Soft Flux[h]	Hard Flux[i]
35	$9.56^{+1.03}_{-0.97}$	$1.79^{+0.09}_{-0.09}$	$65.5^{+1.8}_{-1.9}$	$0.66^{+0.01}_{-0.02}$	$1.08^{+0.03}_{-0.02}$
36	$19.60^{+2.07}_{-1.92}$	$1.90^{+0.07}_{-0.24}$	$67.2^{+2.6}_{-2.7}$	$0.52^{+0.01}_{-0.02}$	$0.69^{+0.02}_{-0.02}$
37	$3.83^{+1.05}_{-0.82}$	$1.87^{+0.13}_{-0.14}$	$38.1^{+2.8}_{-3.0}$	$1.06^{+0.02}_{-0.02}$	$1.40^{+0.02}_{-0.02}$
38	$2.09^{+0.28}_{-0.26}$	$1.37^{+0.10}_{-0.11}$	$39.0^{+1.8}_{-1.8}$	$1.57^{+0.02}_{-0.02}$	$2.39^{+0.02}_{-0.02}$
39	$2.15^{+0.68}_{-0.52}$	$1.10^{+0.22}_{-0.25}$	$35.5^{+2.8}_{-3.1}$	$1.25^{+0.02}_{-0.02}$	$1.73^{+0.02}_{-0.02}$
40	$2.46^{+0.75}_{-0.53}$	$2.09^{+0.11}_{-0.11}$	$30.4^{+13.2}_{-13.3}$	$1.80^{+0.03}_{-0.03}$	$2.39^{+0.02}_{-0.02}$
41	$1.96^{+0.13}_{-0.12}$	$1.47^{+0.08}_{-0.08}$	$50.7^{+29.3}_{-30.0}$	$1.44^{+0.03}_{-0.02}$	$1.96^{+0.02}_{-0.02}$
42	$3.05^{+0.59}_{-0.60}$	$2.05^{+0.07}_{-0.07}$	$46.0^{+13.0}_{-13.1}$	$1.07^{+0.03}_{-0.02}$	$1.52^{+0.02}_{-0.02}$
43	$2.63^{+0.37}_{-0.33}$	$1.91^{+0.07}_{-0.09}$	$41.4^{+2.3}_{-2.4}$	$1.61^{+0.02}_{-0.03}$	$1.53^{+0.02}_{-0.02}$
44	$2.25^{+2.03}_{-1.60}$	$2.18^{+0.13}_{-0.14}$	$37.8^{+3.7}_{-3.9}$	$1.72^{+0.03}_{-0.03}$	$2.20^{+0.03}_{-0.02}$

Table 15 continued

Rev 1001	PLC norm[a]	q[b]	ξ[c]	RDC norm[d]	χ^2 (dof)
1	$5.98^{+0.11}_{-0.11}$	$3.78^{+0.46}_{-0.38}$	$163.0^{+9.6}_{-9.1}$	$4.06^{+0.32}_{-0.33}$	362.59 (350)
2	$5.65^{+0.05}_{-0.05}$	$3.51^{+0.32}_{-0.28}$	$219.5^{+6.5}_{-6.7}$	$1.68^{+0.86}_{-0.94}$	419.88 (360)
3	$6.36^{+0.08}_{-0.08}$	$3.83^{+0.89}_{-0.66}$	$150.4^{+15.0}_{-13.7}$	$1.72^{+0.26}_{-0.26}$	331.64 (366)
4	$7.10^{+0.08}_{-0.08}$	$3.87^{+0.29}_{-0.27}$	$204.7^{+5.1}_{-5.5}$	$3.41^{+0.17}_{-0.17}$	370.04 (344)
5	$7.80^{+0.08}_{-0.08}$	$3.42^{+0.48}_{-0.39}$	$197.4^{+9.5}_{-15.4}$	$1.97^{+0.18}_{-0.18}$	408.57 (353)
6	$7.96^{+0.09}_{-0.09}$	$3.65^{+0.51}_{-0.48}$	$333.8^{+27.8}_{-25.8}$	$1.07^{+0.88}_{-0.89}$	393.32 (366)
7	$5.99^{+0.08}_{-0.08}$	$3.63^{+0.46}_{-0.42}$	$359.0^{+25.5}_{-25.4}$	$1.01^{+0.65}_{-0.71}$	393.45 (372)
8	$5.22^{+0.05}_{-0.05}$	$3.88^{+0.58}_{-0.46}$	$144.5^{+7.9}_{-7.6}$	$2.00^{+0.18}_{-0.18}$	384.53 (364)
9	$6.16^{+0.10}_{-0.10}$	$3.43^{+0.46}_{-0.41}$	$241.3^{+12.3}_{-12.5}$	$1.86^{+0.14}_{-0.15}$	351.22 (350)

Rev 1001	n_H[e]	ξ[f]	CF %[g]	Soft Flux[h]	Hard Flux[i]
1	$0.78^{+0.13}_{-0.12}$	$1.44^{+0.11}_{-0.10}$	$56.7^{+14.4}_{-14.6}$	$1.66^{+0.03}_{-0.04}$	$2.08^{+0.03}_{-0.03}$
2	$0.72^{+0.16}_{-0.16}$	$1.30^{+0.06}_{-0.06}$	$55.2^{+12.2}_{-12.3}$	$1.45^{+0.02}_{-0.02}$	$1.96^{+0.01}_{-0.02}$
3	$1.50^{+0.50}_{-0.63}$	$1.56^{+0.19}_{-0.18}$	$30.3^{+13.1}_{-13.3}$	$1.58^{+0.03}_{-0.02}$	$2.14^{+0.03}_{-0.02}$
4	$0.93^{+0.65}_{-0.39}$	$1.57^{+0.67}_{-0.29}$	$15.2^{+23.5}_{-13.7}$	$2.19^{+0.03}_{-0.03}$	$2.48^{+0.03}_{-0.02}$
5	$1.19^{+0.91}_{-0.73}$	$2.02^{+0.11}_{-0.14}$	$27.4^{+12.7}_{-12.8}$	$2.07^{+0.03}_{-0.02}$	$2.57^{+0.02}_{-0.03}$
6	$0.97^{+0.10}_{-0.10}$	$1.46^{+0.06}_{-0.06}$	$57.2^{+12.4}_{-12.4}$	$1.97^{+0.03}_{-0.03}$	$2.68^{+0.02}_{-0.02}$
7	$1.77^{+0.33}_{-0.29}$	$0.69^{+0.16}_{-0.11}$	$35.6^{+4.3}_{-2.2}$	$1.35^{+0.02}_{-0.02}$	$2.02^{+0.02}_{-0.02}$
8	$1.77^{+0.24}_{-0.22}$	$1.77^{+0.10}_{-0.10}$	$41.5^{+2.5}_{-2.5}$	$1.29^{+0.02}_{-0.01}$	$1.77^{+0.02}_{-0.02}$
9	$0.59^{+0.88}_{-0.57}$	$1.22^{+0.12}_{-0.11}$	$55.4^{+14.1}_{-14.2}$	$1.67^{+0.04}_{-0.03}$	$2.15^{+0.03}_{-0.03}$

Table 15 continued

Rev 1002	PLC norm[a]	q[b]	ξ[c]	RDC norm[d]	χ^2 (dof)
1	$10.01^{+0.15}_{-0.11}$	$3.37^{+2.13}_{-2.13}$	< 273.6	< 7.47	347.71 (379)
2	$6.39^{+0.10}_{-0.10}$	$3.39^{+0.56}_{-0.49}$	$366.6^{+34.4}_{-30.7}$	$0.94^{+0.08}_{-0.08}$	362.39 (360)
3	$5.34^{+0.08}_{-0.08}$	$3.67^{+0.37}_{-0.30}$	$234.2^{+8.5}_{-8.3}$	$2.19^{+0.12}_{-0.13}$	386.77 (353)
4	$6.63^{+0.12}_{-0.12}$	$3.60^{+0.74}_{-0.57}$	$200.1^{+12.1}_{-20.7}$	$1.97^{+0.24}_{-0.24}$	364.66 (360)
5	$7.75^{+0.15}_{-0.15}$	$3.50^{+0.56}_{-0.45}$	$246.5^{+14.6}_{-13.9}$	$2.38^{+0.20}_{-0.20}$	389.65 (354)
6	$8.73^{+0.13}_{-0.13}$	$3.65^{+0.79}_{-0.59}$	$186.4^{+17.6}_{-19.3}$	$2.19^{+0.29}_{-0.29}$	406.47 (362)
7	$7.58^{+0.09}_{-0.09}$	$3.43^{+0.40}_{-0.37}$	$185.8^{+12.6}_{-11.8}$	$2.66^{+0.21}_{-0.21}$	347.84 (349)
8	$7.74^{+0.12}_{-0.12}$	$3.20^{+0.43}_{-0.39}$	$243.3^{+13.3}_{-12.6}$	$1.98^{+0.16}_{-0.16}$	374.37 (350)
9	$8.80^{+0.15}_{-0.15}$	$4.08^{+1.58}_{-1.12}$	$212.6^{+32.4}_{-45.2}$	$1.19^{+0.32}_{-0.34}$	361.39 (374)
10	$7.71^{+0.10}_{-0.10}$	$3.23^{+0.38}_{-0.33}$	$101.5^{+2.1}_{-3.6}$	$7.37^{+0.66}_{-0.65}$	377.44 (360)
11	$9.52^{+0.13}_{-0.14}$	$3.12^{+1.10}_{-0.93}$	$88.8^{+14.0}_{-20.9}$	$3.55^{+1.17}_{-1.15}$	406.54 (378)
12	$10.44^{+0.16}_{-0.16}$	$3.53^{+0.85}_{-0.71}$	$191.7^{+20.1}_{-28.8}$	$2.01^{+0.37}_{-0.37}$	361.61 (368)
13	$9.41^{+0.13}_{-0.13}$	$3.37^{+0.89}_{-0.70}$	$140.7^{+17.0}_{-15.2}$	$2.15^{+0.41}_{-0.43}$	427.42 (365)
14	$8.40^{+0.10}_{-0.10}$	$3.45^{+0.32}_{-0.28}$	$199.3^{+5.6}_{-10.7}$	$3.65^{+0.22}_{-0.22}$	357.96 (347)
15	$10.94^{+0.19}_{-0.19}$	$3.48^{+0.76}_{-0.62}$	$191.3^{+16.0}_{-21.9}$	$2.75^{+0.43}_{-0.38}$	376.82 (360)
16	$10.77^{+0.20}_{-0.19}$	$3.09^{+0.80}_{-0.69}$	$215.1^{+17.7}_{-17.5}$	$2.06^{+0.29}_{-0.29}$	389.88 (351)
17	$8.71^{+0.12}_{-0.12}$	$3.71^{+0.54}_{-0.45}$	$139.3^{+8.3}_{-7.9}$	$4.52^{+0.48}_{-0.48}$	389.61 (356)
18	$7.43^{+0.10}_{-0.10}$	$3.45^{+0.58}_{-0.49}$	$145.9^{+11.1}_{-10.4}$	$2.55^{+0.31}_{-0.31}$	360.40 (368)

Rev 1002	n_H[e]	ξ[f]	CF %[g]	Soft Flux[h]	Hard Flux[i]
1	$1.41^{+0.36}_{-0.31}$	$1.36^{+0.15}_{-0.16}$	$38.1^{+3.4}_{-3.5}$	$2.14^{+0.04}_{-0.02}$	$3.20^{+0.05}_{-0.02}$
2	$0.49^{+0.66}_{-0.45}$	$1.42^{+0.11}_{-0.10}$	$63.9^{+14.9}_{-15.1}$	$1.75^{+0.02}_{-0.02}$	$2.23^{+0.03}_{-0.04}$
3	$0.71^{+0.66}_{-0.62}$	$1.35^{+0.06}_{-0.07}$	$67.8^{+13.0}_{-13.1}$	$1.45^{+0.02}_{-0.02}$	$1.89^{+0.03}_{-0.02}$
4	$1.62^{+0.94}_{-0.67}$	$1.30^{+0.34}_{-0.41}$	$24.4^{+14.2}_{-14.5}$	$1.70^{+0.04}_{-0.03}$	$2.24^{+0.03}_{-0.03}$
5	< 0.84	$1.62^{+0.13}_{-0.12}$	< 0.99	$2.26^{+0.03}_{-0.05}$	$2.70^{+0.04}_{-0.03}$
6	$0.70^{+0.20}_{-0.16}$	$1.35^{+0.19}_{-0.18}$	$36.4^{+4.7}_{-4.9}$	$2.23^{+0.04}_{-0.04}$	$2.91^{+0.04}_{-0.04}$
7	$0.45^{+0.62}_{-0.29}$	$2.36^{+1.21}_{-1.21}$	$48.4^{+11.1}_{-11.3}$	$2.23^{+0.03}_{-0.03}$	$2.61^{+0.03}_{-0.02}$
8	$0.29^{+0.38}_{-0.21}$	$1.59^{+0.17}_{-0.17}$	$56.6^{+8.8}_{-9.8}$	$2.30^{+0.05}_{-0.03}$	$2.69^{+0.03}_{-0.03}$
9	$1.85^{+0.54}_{-0.45}$	$1.61^{+0.22}_{-0.22}$	$39.9^{+3.9}_{-4.0}$	$2.02^{+0.06}_{-0.06}$	$2.83^{+0.04}_{-0.03}$
10	$0.67^{+0.43}_{-0.11}$	$1.49^{+0.13}_{-0.13}$	$42.0^{+4.0}_{-4.1}$	$2.02^{+0.03}_{-0.02}$	$2.64^{+0.03}_{-0.03}$
11	$2.47^{+1.26}_{-1.11}$	$1.29^{+0.18}_{-0.17}$	$29.5^{+12.7}_{-12.6}$	$2.00^{+0.03}_{-0.03}$	$3.04^{+0.03}_{-0.02}$
12	$1.88^{+1.21}_{-0.86}$	$1.02^{+0.41}_{-0.40}$	$27.6^{+13.0}_{-13.1}$	$2.27^{+0.05}_{-0.06}$	$3.30^{+0.04}_{-0.03}$
13	$1.39^{+0.98}_{-0.98}$	$1.60^{+0.17}_{-0.18}$	$35.6^{+5.2}_{-7.2}$	$2.05^{+0.04}_{-0.04}$	$2.91^{+0.03}_{-0.03}$
14	$1.37^{+0.16}_{-0.15}$	$1.67^{+0.07}_{-0.07}$	$57.0^{+12.7}_{-12.6}$	$2.24^{+0.03}_{-0.04}$	$2.77^{+0.03}_{-0.03}$
15	$2.90^{+0.64}_{-1.45}$	$1.75^{+0.16}_{-0.16}$	$46.9^{+3.0}_{-3.0}$	$2.52^{+0.04}_{-0.07}$	$3.41^{+0.05}_{-0.04}$
16	$1.70^{+0.61}_{-0.47}$	$2.25^{+1.62}_{-1.56}$	$42.5^{+6.6}_{-6.8}$	$2.92^{+0.08}_{-0.06}$	$3.54^{+0.05}_{-0.04}$
17	$1.54^{+0.31}_{-0.28}$	$1.42^{+0.14}_{-0.14}$	$43.7^{+3.0}_{-3.0}$	$2.10^{+0.03}_{-0.03}$	$2.85^{+0.03}_{-0.03}$
18	$2.40^{+0.63}_{-0.91}$	$1.57^{+0.08}_{-0.12}$	$48.8^{+3.8}_{-3.5}$	$1.62^{+0.03}_{-0.03}$	$2.37^{+0.03}_{-0.02}$

Table 15 continued

Rev 1003	PLC norm[a]	q[b]	ξ[c]	RDC norm[d]	χ^2 (dof)
72	$6.93^{+0.12}_{-0.12}$	$3.36^{+0.62}_{-0.52}$	$245.5^{+18.5}_{-17.3}$	$1.50^{+0.16}_{-0.16}$	333.29 (354)
73	$8.91^{+0.14}_{-0.14}$	$3.41^{+1.17}_{-0.83}$	$211.5^{+22.5}_{-30.6}$	$1.28^{+0.26}_{-0.26}$	357.33 (360)
74	$6.94^{+0.15}_{-0.15}$	$3.64^{+1.49}_{-1.02}$	$245.0^{+36.8}_{-31.5}$	$1.00^{+0.21}_{-0.20}$	335.50 (366)
75	$10.38^{+0.21}_{-0.21}$	$3.39^{+1.53}_{-1.78}$	$223.3^{+40.1}_{-43.5}$	$1.10^{+0.31}_{-0.30}$	335.25 (370)
76	$8.80^{+0.15}_{-0.15}$	$3.55^{+1.00}_{-0.71}$	$96.0^{+7.3}_{-16.2}$	$5.80^{+1.26}_{-1.19}$	337.26 (372)
77	$7.30^{+0.18}_{-0.18}$	$3.41^{+0.70}_{-0.57}$	$267.7^{+21.4}_{-19.8}$	$2.01^{+0.20}_{-0.20}$	340.29 (361)
78	$7.48^{+0.20}_{-0.20}$	$3.63^{+0.63}_{-0.55}$	$345.4^{+37.0}_{-33.5}$	$1.86^{+0.19}_{-0.19}$	341.85 (364)
79	$8.71^{+0.20}_{-0.20}$	$3.19^{+1.62}_{-1.65}$	$233.4^{+48.5}_{-47.4}$	$0.90^{+0.27}_{-0.27}$	388.01 (369)
80	$7.32^{+0.13}_{-0.13}$	$3.34^{+0.81}_{-0.70}$	$295.2^{+77.6}_{-69.7}$	$0.60^{+0.79}_{-0.59}$	381.10 (375)
81	$8.07^{+0.14}_{-0.14}$	$3.01^{+2.29}_{-2.18}$	$72.8^{+20.3}_{-16.0}$	$3.95^{+1.61}_{-1.62}$	389.31 (377)
82	$7.34^{+0.12}_{-0.12}$	$3.40^{+1.74}_{-2.96}$	$113.2^{+12.8}_{-11.6}$	$1.76^{+0.57}_{-0.58}$	366.58 (378)
83	$7.67^{+0.16}_{-0.16}$	$3.74^{+2.34}_{-1.17}$	$318.4^{+63.0}_{-52.5}$	$0.81^{+0.87}_{-0.16}$	402.12 (366)
84	$7.96^{+0.14}_{-0.15}$	$3.46^{+3.81}_{-3.26}$	$111.1^{+25.6}_{-44.7}$	$1.25^{+0.82}_{-0.81}$	359.13 (338)
85	$7.06^{+0.17}_{-0.17}$	$3.66^{+1.07}_{-0.84}$	$230.7^{+25.0}_{-22.7}$	$1.72^{+0.29}_{-0.29}$	365.68 (367)
86	$6.38^{+0.10}_{-0.10}$	$3.63^{+2.23}_{-1.15}$	$107.7^{+11.5}_{-18.7}$	$2.04^{+0.71}_{-0.71}$	376.18 (368)
87	$7.05^{+0.15}_{-0.15}$	$3.40^{+1.17}_{-0.74}$	$122.5^{+10.5}_{-9.7}$	$3.36^{+0.66}_{-0.66}$	318.28 (371)
88	$3.87^{+0.11}_{-0.11}$	$3.70^{+0.59}_{-0.47}$	$199.9^{+10.2}_{-18.9}$	$2.48^{+0.27}_{-0.27}$	323.68 (345)
89	$5.02^{+0.07}_{-0.07}$	$3.70^{+0.49}_{-0.39}$	$199.9^{+7.7}_{-14.5}$	$1.97^{+0.16}_{-0.16}$	368.88 (361)
90	$6.33^{+0.15}_{-0.15}$	$3.70^{+0.98}_{-0.71}$	$128.7^{+12.2}_{-11.2}$	$2.93^{+0.58}_{-0.58}$	387.80 (370)
91	$3.79^{+0.10}_{-0.10}$	$3.59^{+0.78}_{-0.60}$	$199.7^{+10.3}_{-23.1}$	$1.70^{+0.21}_{-0.23}$	383.84 (352)

Rev 1003	n_H[e]	ξ[f]	CF %[g]	Soft Flux[h]	Hard Flux[i]
72	$0.45^{+1.51}_{-0.14}$	$1.37^{+0.26}_{-0.25}$	$36.8^{+6.9}_{-7.2}$	$1.97^{+0.03}_{-0.04}$	$2.42^{+0.04}_{-0.03}$
73	$0.84^{+0.34}_{-0.24}$	$1.58^{+0.21}_{-0.22}$	$33.9^{+5.5}_{-5.7}$	$2.28^{+0.06}_{-0.05}$	$2.96^{+0.04}_{-0.03}$
74	$1.26^{+0.66}_{-0.51}$	$1.66^{+0.42}_{-0.27}$	$32.6^{+9.5}_{-6.7}$	$1.81^{+0.05}_{-0.05}$	$2.37^{+0.05}_{-0.04}$
75	$1.11^{+7.08}_{-0.90}$	$1.20^{+1.14}_{-1.20}$	$28.1^{+16.7}_{-16.2}$	$2.61^{+0.07}_{-0.07}$	$3.44^{+0.04}_{-0.04}$
76	$1.57^{+0.62}_{-0.47}$	$1.52^{+0.25}_{-0.26}$	$31.6^{+6.4}_{-6.4}$	$2.12^{+0.04}_{-0.04}$	$2.90^{+0.03}_{-0.03}$
77	$1.14^{+0.23}_{-0.21}$	$1.09^{+0.12}_{-0.12}$	$51.3^{+13.4}_{-13.5}$	$1.84^{+0.05}_{-0.04}$	$2.48^{+0.04}_{-0.04}$
78	$0.79^{+0.37}_{-0.13}$	$0.70^{+1.22}_{-0.26}$	$51.6^{+14.9}_{-15.1}$	$1.91^{+0.05}_{-0.06}$	$2.61^{+0.06}_{-0.03}$
79	$1.61^{+0.69}_{-0.51}$	$1.60^{+0.34}_{-0.30}$	$36.6^{+5.4}_{-5.7}$	$2.08^{+0.07}_{-0.06}$	$2.84^{+0.06}_{-0.03}$
80	$0.78^{+0.31}_{-0.17}$	$0.95^{+0.30}_{-0.24}$	$37.2^{+4.1}_{-4.1}$	$1.82^{+0.04}_{-0.03}$	$2.50^{+0.03}_{-0.03}$
81	$1.36^{+0.86}_{-0.57}$	$1.06^{+0.42}_{-0.31}$	$24.2^{+14.4}_{-14.6}$	$1.90^{+0.03}_{-0.04}$	$2.68^{+0.04}_{-0.03}$
82	$0.96^{+0.34}_{-0.17}$	$1.22^{+0.13}_{-0.23}$	$45.7^{+3.7}_{-4.8}$	$1.64^{+0.03}_{-0.04}$	$2.43^{+0.04}_{-0.03}$
83	$0.87^{+0.56}_{-0.37}$	$1.09^{+0.41}_{-0.31}$	$21.4^{+15.2}_{-15.4}$	$1.99^{+0.05}_{-0.05}$	$2.61^{+0.04}_{-0.04}$
84	$1.81^{+2.00}_{-1.00}$	$1.41^{+0.66}_{-0.72}$	$29.1^{+15.2}_{-15.5}$	$1.88^{+0.05}_{-0.03}$	$2.62^{+0.05}_{-0.04}$
85	$1.02^{+0.77}_{-0.46}$	$0.87^{+0.50}_{-0.32}$	$23.8^{+15.5}_{-15.8}$	$1.86^{+0.05}_{-0.06}$	$2.42^{+0.05}_{-0.05}$
86	$0.98^{+0.32}_{-0.29}$	$1.72^{+0.21}_{-0.18}$	$39.4^{+5.8}_{-6.0}$	$1.57^{+0.03}_{-0.03}$	$2.16^{+0.03}_{-0.03}$
87	$0.85^{+0.28}_{-0.22}$	$1.52^{+0.20}_{-0.18}$	$44.8^{+6.2}_{-6.5}$	$1.79^{+0.05}_{-0.04}$	$2.38^{+0.04}_{-0.05}$
88	$0.72^{+0.42}_{-0.20}$	$1.11^{+0.25}_{-0.24}$	$44.5^{+6.3}_{-6.6}$	$1.15^{+0.04}_{-0.03}$	$1.42^{+0.04}_{-0.04}$
89	$1.45^{+0.29}_{-0.23}$	$1.23^{+0.12}_{-0.11}$	$40.8^{+2.6}_{-2.7}$	$1.24^{+0.02}_{-0.02}$	$1.73^{+0.03}_{-0.02}$
90	< 4.39	$1.73^{+0.29}_{-0.19}$	$39.2^{+3.6}_{-3.9}$	$1.32^{+0.03}_{-0.04}$	$1.92^{+0.04}_{-0.03}$
91	< 5.04	$1.97^{+0.12}_{-0.23}$	$41.2^{+4.1}_{-4.3}$	$0.92^{+0.03}_{-0.02}$	$1.24^{+0.03}_{-0.03}$

Table 15 continued

Rev 1004	PLC norm[a]	q[b]	ξ[c]	RDC norm[d]	χ^2 (dof)
92	$4.70^{+0.08}_{-0.08}$	$3.90^{+0.77}_{-0.59}$	$219.0^{+11.4}_{-11.3}$	$1.45^{+0.14}_{-0.14}$	326.23 (353)
93	$4.60^{+0.10}_{-0.10}$	$3.98^{+0.76}_{-0.72}$	$356.7^{+38.3}_{-19.9}$	$0.91^{+0.10}_{-0.10}$	372.95 (358)
94	$7.36^{+0.14}_{-0.14}$	$3.57^{+1.51}_{-0.96}$	$134.9^{+17.0}_{-8.8}$	$2.23^{+0.53}_{-0.53}$	404.75 (385)
95	$5.32^{+0.13}_{-0.13}$	$3.7.2^{+0.56}_{-0.45}$	$312.2^{+20.7}_{-19.5}$	$2.00^{+0.15}_{-0.15}$	425.62 (383)

Rev 1004	n_H[e]	ξ[f]	CF %[g]	Soft Flux[h]	Hard Flux[i]
92	$3.71^{+0.79}_{-0.85}$	$2.18^{+0.07}_{-0.07}$	$48.5^{+3.5}_{-3.7}$	$1.22^{+0.02}_{-0.03}$	$1.57^{+0.02}_{-0.03}$
93	$2.40^{+2.59}_{-0.59}$	$1.46^{+0.19}_{-0.21}$	$38.6^{+3.5}_{-3.7}$	$1.16^{+0.03}_{-0.03}$	$1.59^{+0.03}_{-0.03}$
94	$0.74^{+0.15}_{-0.13}$	$1.03^{+0.18}_{-0.24}$	$47.9^{+4.1}_{-4.1}$	$1.67^{+0.04}_{-0.04}$	$2.44^{+0.04}_{-0.04}$
95	$0.38^{+0.06}_{-0.05}$	$0.43^{+0.14}_{-0.09}$	$72.3^{+3.6}_{-41.8}$	$1.32^{+0.03}_{-0.03}$	$1.95^{+0.03}_{-0.04}$

Table 16: Atomic feature model parameters.

Rev 82	Fe flux[a]	Line[b]	Flux[c]	Edge[d]	τ[e]
1	< 24.74	$0.459^{+0.018}_{-0.016}$	$6.28^{+2.48}_{-2.44}$	$0.688^{+0.018}_{-0.016}$	$0.358^{+0.072}_{-0.071}$
2	$19.68^{+9.77}_{-9.84}$	$0.473^{+0.013}_{-0.012}$	$4.99^{+1.50}_{-1.44}$	$0.635^{+0.048}_{-0.041}$	$0.134^{+0.067}_{-0.032}$
3	$8.53^{+7.23}_{-7.23}$	$0.409^{+0.067}_{-0.038}$	$4.21^{+2.09}_{-1.90}$	$0.680^{+0.022}_{-0.014}$	$0.273^{+0.046}_{-0.048}$
4	$7.97^{+6.92}_{-6.94}$	$0.476^{+0.013}_{-0.017}$	$4.04^{+1.14}_{-1.05}$	$0.627^{+0.017}_{-0.015}$	$0.289^{+0.057}_{-0.057}$
5	$11.86^{+6.32}_{-6.33}$	$0.459^{+0.011}_{-0.012}$	$5.10^{+1.13}_{-1.06}$	$0.612^{+0.012}_{-0.015}$	$0.259^{+0.049}_{-0.043}$
6	$11.64^{+9.09}_{-9.05}$	$0.441^{+0.046}_{-0.110}$	$2.58^{+2.04}_{-1.69}$	$0.616^{+0.026}_{-0.024}$	$0.218^{+0.055}_{-0.055}$
7	< 12.12	$0.446^{+0.022}_{-0.053}$	$6.02^{+2.41}_{-2.28}$	$0.691^{+0.019}_{-0.015}$	$0.266^{+0.048}_{-0.050}$
8	$12.84^{+10.35}_{-10.55}$	$0.470^{+0.016}_{-0.016}$	$6.58^{+1.71}_{-1.71}$	$0.636^{+0.033}_{-0.026}$	$0.209^{+0.060}_{-0.060}$
9	< 9.36	$0.465^{+0.017}_{-0.016}$	$6.88^{+2.24}_{-2.27}$	$0.710^{+0.009}_{-0.014}$	$0.454^{+0.047}_{-0.056}$

Notes. [a] Narrow Fe Kα line flux in units of photons cm^{-2} sec^{-1}. [b] Line energy in units of keV. [c] Flux in units of photons cm^{-2} sec^{-1}. [d] Edge energy in units of keV. [e] Optical depth.

Table 16 continued

Rev 265	Fe flux[a]	Line[b]	Flux[c]	Edge[d]	τ[e]
10	$11.46^{+8.24}_{-8.34}$	$0.453^{+0.009}_{-0.004}$	$14.58^{+1.57}_{-1.56}$	$0.685^{+0.008}_{-0.004}$	$0.416^{+0.024}_{-0.028}$
11	< 17.37	$0.473^{+0.009}_{-0.011}$	$11.60^{+1.82}_{-1.82}$	$0.716^{+0.005}_{-0.005}$	$0.446^{+0.025}_{-0.022}$
12	< 10.46	$0.467^{+0.015}_{-0.023}$	$6.19^{+2.76}_{-2.75}$	$0.694^{+0.011}_{-0.006}$	$0.215^{+0.025}_{-0.025}$
13	< 15.69	$0.465^{+0.010}_{-0.010}$	$8.97^{+1.66}_{-1.66}$	$0.702^{+0.007}_{-0.008}$	$0.327^{+0.028}_{-0.028}$
14	$15.23^{+8.26}_{-11.85}$	$0.474^{+0.008}_{-0.013}$	$8.46^{+1.80}_{-1.80}$	$0.697^{+0.009}_{-0.008}$	$0.306^{+0.028}_{-0.028}$
15	< 19.09	$0.467^{+0.014}_{-0.013}$	$7.00^{+1.97}_{-1.74}$	$0.685^{+0.014}_{-0.005}$	$0.289^{+0.031}_{-0.030}$
16	$7.41^{+5.44}_{-5.47}$	$0.465^{+0.008}_{-0.004}$	$8.48^{+1.09}_{-0.99}$	$0.685^{+0.007}_{-0.006}$	$0.338^{+0.023}_{-0.024}$
17	< 13.01	$0.444^{+0.021}_{-0.018}$	$8.56^{+2.98}_{-3.11}$	$0.696^{+0.009}_{-0.008}$	$0.413^{+0.047}_{-0.047}$
18	< 16.28	$0.420^{+0.026}_{-0.038}$	$8.76^{+3.80}_{-3.57}$	$0.698^{+0.012}_{-0.010}$	$0.331^{+0.030}_{-0.037}$
19	$15.84^{+9.27}_{-9.13}$	$0.480^{+0.011}_{-0.012}$	$6.05^{+1.48}_{-1.50}$	$0.703^{+0.009}_{-0.008}$	$0.350^{+0.031}_{-0.031}$
20	< 15.33	$0.471^{+0.012}_{-0.009}$	$7.59^{+1.62}_{-1.62}$	$0.705^{+0.006}_{-0.007}$	$0.408^{+0.027}_{-0.027}$
21	$13.41^{+7.39}_{-7.39}$	$0.454^{+0.011}_{-0.011}$	$8.15^{+1.51}_{-1.53}$	$0.685^{+0.008}_{-0.007}$	$0.330^{+0.025}_{-0.025}$
22	$24.03^{+10.19}_{-10.29}$	$0.474^{+0.009}_{-0.011}$	$8.20^{+1.84}_{-1.85}$	$0.712^{+0.007}_{-0.006}$	$0.425^{+0.029}_{-0.028}$
23	$25.06^{+11.83}_{-12.45}$	$0.479^{+0.013}_{-0.015}$	$5.55^{+1.97}_{-2.27}$	$0.686^{+0.008}_{-0.010}$	$0.360^{+0.041}_{-0.037}$
24	< 16.27	$0.473^{+0.011}_{-0.015}$	$6.54^{+1.73}_{-1.61}$	$0.696^{+0.008}_{-0.008}$	$0.382^{+0.034}_{-0.035}$
25	$20.60^{+10.73}_{-10.51}$	$0.460^{+0.023}_{-0.028}$	$3.06^{+1.77}_{-1.94}$	$0.679^{+0.015}_{-0.016}$	$0.211^{+0.039}_{-0.036}$
26	< 20.74	$0.459^{+0.015}_{-0.033}$	$5.29^{+2.44}_{-2.34}$	$0.704^{+0.009}_{-0.011}$	$0.377^{+0.040}_{-0.040}$
27	< 21.80	$0.456^{+0.017}_{-0.027}$	$5.66^{+2.51}_{-2.23}$	$0.705^{+0.009}_{-0.011}$	$0.399^{+0.040}_{-0.038}$
28	$7.74^{+6.61}_{-6.61}$	$0.459^{+0.009}_{-0.021}$	$6.06^{+1.44}_{-1.43}$	$0.703^{+0.007}_{-0.007}$	$0.415^{+0.028}_{-0.028}$

Table 16 continued

Rev 999	Fe flux[a]	Line[b]	Flux[c]	Edge[d]	τ[e]
29	$6.37^{+3.41}_{-3.31}$	$0.542^{+0.005}_{-0.005}$	$6.07^{+0.71}_{-0.71}$	$0.714^{+0.009}_{-0.006}$	$0.721^{+0.054}_{-0.051}$
30	$5.60^{+3.29}_{-3.32}$	$0.535^{+0.020}_{-0.027}$	$6.10^{+2.18}_{-1.91}$	$0.702^{+0.008}_{-0.009}$	$0.641^{+0.052}_{-0.050}$
31	$9.09^{+4.08}_{-4.10}$	$0.476^{+0.009}_{-0.016}$	$1.46^{+0.48}_{-0.46}$	$0.693^{+0.011}_{-0.013}$	$0.391^{+0.052}_{-0.050}$
32	$9.32^{+3.47}_{-3.47}$	$0.486^{+0.019}_{-0.027}$	$0.71^{+0.40}_{-0.41}$	$0.724^{+0.010}_{-0.012}$	$0.350^{+0.037}_{-0.035}$
33	< 8.97	-	-	$0.695^{+0.014}_{-0.014}$	$0.472^{+0.066}_{-0.065}$
34	$5.98^{+3.14}_{-3.70}$	$0.543^{+0.005}_{-0.005}$	$5.97^{+0.71}_{-0.71}$	$0.717^{+0.008}_{-0.006}$	$0.741^{+0.054}_{-0.052}$

Table 16 continued

Rev 1000	Fe flux[a]	Line[b]	Flux[c]	Edge[d]	τ[e]
35	< 7.08	$0.592^{+0.017}_{-0.016}$	$1.42^{+0.53}_{-0.53}$	$0.729^{+0.013}_{-0.013}$	$0.507^{+0.065}_{-0.064}$
36	$6.99^{+4.01}_{-4.02}$	$0.400^{+0.016}_{-0.071}$	$2.09^{+1.09}_{-1.08}$	$0.695^{+0.011}_{-0.010}$	$0.686^{+0.066}_{-0.063}$
37	$8.68^{+5.22}_{-5.22}$	$0.583^{+0.020}_{-0.020}$	$1.61^{+0.74}_{-0.74}$	$0.690^{+0.012}_{-0.011}$	$0.380^{+0.047}_{-0.047}$
38	$10.90^{+4.69}_{-4.69}$	$0.462^{+0.020}_{-0.015}$	$1.91^{+0.65}_{-0.65}$	$0.704^{+0.007}_{-0.010}$	$0.343^{+0.029}_{-0.028}$
39	$10.10^{+5.37}_{-5.39}$	$0.468^{+0.012}_{-0.008}$	$3.71^{+0.92}_{-0.73}$	$0.712^{+0.012}_{-0.009}$	$0.408^{+0.041}_{-0.036}$
40	$7.84^{+5.70}_{-5.65}$	$0.486^{+0.012}_{-0.025}$	$2.18^{+0.88}_{-0.88}$	$0.702^{+0.009}_{-0.010}$	$0.347^{+0.032}_{-0.031}$
41	$8.26^{+4.82}_{-4.81}$	$0.470^{+0.012}_{-0.009}$	$3.24^{+0.76}_{-0.76}$	$0.695^{+0.016}_{-0.016}$	$0.206^{+0.032}_{-0.034}$
42	$7.29^{+4.89}_{-4.49}$	$0.471^{+0.015}_{-0.016}$	$2.16^{+0.67}_{-0.75}$	$0.661^{+0.017}_{-0.015}$	$0.311^{+0.041}_{-0.043}$
43	$8.36^{+3.80}_{-3.56}$	$0.427^{+0.036}_{-0.024}$	$3.36^{+1.20}_{-1.23}$	$0.683^{+0.013}_{-0.009}$	$0.305^{+0.028}_{-0.031}$
44	< 11.39	$0.471^{+0.012}_{-0.016}$	$3.31^{+1.09}_{-1.01}$	$0.691^{+0.010}_{-0.009}$	$0.423^{+0.041}_{-0.042}$

Table 16 continued

Rev 1001	Fe flux[a]	Line[b]	Flux[c]	Edge[d]	τ[e]
1	< 12.95	$0.459^{+0.015}_{-0.022}$	$3.85^{+1.37}_{-1.33}$	$0.660^{+0.031}_{-0.027}$	$0.174^{+0.049}_{-0.051}$
2	$6.85^{+3.61}_{-3.61}$	$0.468^{+0.012}_{-0.010}$	$2.17^{+0.58}_{-0.58}$	$0.675^{+0.010}_{-0.011}$	$0.243^{+0.027}_{-0.026}$
3	$7.07^{+5.60}_{-5.50}$	$0.461^{+0.010}_{-0.010}$	$3.95^{+0.95}_{-0.96}$	$0.705^{+0.010}_{-0.012}$	$0.335^{+0.033}_{-0.038}$
4	$5.88^{+5.67}_{-5.49}$	$0.449^{+0.012}_{-0.015}$	$5.14^{+1.15}_{-1.09}$	$0.704^{+0.007}_{-0.006}$	$0.431^{+0.028}_{-0.027}$
5	$10.11^{+6.20}_{-6.13}$	$0.456^{+0.012}_{-0.010}$	$5.59^{+1.05}_{-1.10}$	$0.713^{+0.005}_{-0.010}$	$0.431^{+0.031}_{-0.031}$
6	$7.62^{+5.73}_{-5.89}$	$0.501^{+0.015}_{-0.028}$	$1.81^{+0.80}_{-0.80}$	$0.689^{+0.020}_{-0.016}$	$0.155^{+0.029}_{-0.030}$
7	< 8.82	$0.468^{+0.013}_{-0.023}$	$1.89^{+0.71}_{-0.72}$	$0.703^{+0.008}_{-0.008}$	$0.432^{+0.033}_{-0.034}$
8	$6.87^{+3.85}_{-3.67}$	$0.453^{+0.015}_{-0.019}$	$2.03^{+0.66}_{-0.64}$	$0.680^{+0.010}_{-0.007}$	$0.334^{+0.027}_{-0.028}$
9	< 9.69	$0.461^{+0.023}_{-0.025}$	$2.49^{+1.22}_{-1.16}$	$0.682^{+0.015}_{-0.018}$	$0.236^{+0.045}_{-0.044}$

Table 16 continued

Rev 1002	Fe flux[a]	Line[b]	Flux[c]	Edge[d]	τ[e]
1	$11.72^{+9.93}_{-10.41}$	$0.462^{+0.025}_{-0.008}$	$3.24^{+1.54}_{-1.51}$	$0.716^{+0.018}_{-0.019}$	$0.220^{+0.045}_{-0.044}$
2	< 12.14	$0.468^{+0.018}_{-0.013}$	$3.03^{+1.05}_{-1.12}$	$0.703^{+0.016}_{-0.015}$	$0.221^{+0.039}_{-0.035}$
3	$8.112^{+5.13}_{-5.16}$	$0.450^{+0.018}_{-0.041}$	$2.03^{+0.95}_{-0.94}$	$0.627^{+0.032}_{-0.035}$	$0.157^{+0.052}_{-0.042}$
4	< 12.78	$0.453^{+0.033}_{-0.036}$	$2.38^{+1.54}_{-1.52}$	$0.691^{+0.011}_{-0.014}$	$0.408^{+0.051}_{-0.048}$
5	< 10.14	$0.465^{+0.028}_{-0.033}$	$2.96^{+1.89}_{-1.83}$	$0.666^{+0.018}_{-0.024}$	$0.261^{+0.056}_{-0.052}$
6	$11.77^{+9.91}_{-9.62}$	$0.465^{+0.012}_{-0.034}$	$4.05^{+1.64}_{-1.64}$	$0.702^{+0.015}_{-0.015}$	$0.305^{+0.040}_{-0.047}$
7	$10.80^{+7.21}_{-7.21}$	$0.460^{+0.013}_{-0.013}$	$4.95^{+1.25}_{-1.26}$	$0.694^{+0.009}_{-0.008}$	$0.403^{+0.034}_{-0.035}$
8	< 8.48	$0.471^{+0.012}_{-0.012}$	$4.93^{+1.32}_{-1.37}$	$0.689^{+0.010}_{-0.013}$	$0.310^{+0.043}_{-0.039}$
9	< 13.12	$0.501^{+0.038}_{-0.041}$	$1.52^{+1.21}_{-1.21}$	$0.680^{+0.022}_{-0.021}$	$0.225^{+0.049}_{-0.049}$
10	< 8.13	$0.471^{+0.009}_{-0.017}$	$4.15^{+0.99}_{-0.99}$	$0.687^{+0.009}_{-0.010}$	$0.330^{+0.037}_{-0.035}$
11	$12.73^{+9.03}_{-8.93}$	$0.482^{+0.017}_{-0.024}$	$1.39^{+1.35}_{-1.11}$	$0.710^{+0.009}_{-0.012}$	$0.463^{+0.049}_{-0.043}$
12	< 13.52	$0.495^{+0.016}_{-0.033}$	$3.28^{+1.66}_{-1.39}$	$0.700^{+0.009}_{-0.013}$	$0.459^{+0.047}_{-0.047}$
13	< 16.75	$0.465^{+0.009}_{-0.015}$	$4.48^{+1.41}_{-1.45}$	$0.713^{+0.008}_{-0.016}$	$0.376^{+0.039}_{-0.041}$
14	< 14.51	$0.454^{+0.009}_{-0.010}$	$7.29^{+1.32}_{-1.17}$	$0.695^{+0.013}_{-0.016}$	$0.253^{+0.032}_{-0.035}$
15	< 17.86	$0.492^{+0.015}_{-0.036}$	$4.15^{+1.81}_{-1.87}$	$0.709^{+0.016}_{-0.018}$	$0.282^{+0.049}_{-0.050}$
16	< 26.03	$0.471^{+0.023}_{-0.009}$	$4.74^{+2.24}_{-2.43}$	$0.722^{+0.013}_{-0.014}$	$0.396^{+0.047}_{-0.050}$
17	$11.13^{+8.58}_{-8.57}$	$0.483^{+0.009}_{-0.012}$	$5.31^{+1.38}_{-1.26}$	$0.707^{+0.014}_{-0.015}$	$0.288^{+0.040}_{-0.041}$
18	$12.60^{+6.55}_{-6.55}$	$0.465^{+0.009}_{-0.017}$	$3.56^{+1.01}_{-1.03}$	$0.690^{+0.012}_{-0.011}$	$0.312^{+0.040}_{-0.040}$

Table 16 continued

Rev 1003	Fe flux[a]	Line[b]	Flux[c]	Edge[d]	τ[e]
72	$14.37^{+8.07}_{-8.14}$	$0.467^{+0.017}_{-0.013}$	$3.85^{+1.42}_{-1.44}$	$0.705^{+0.012}_{-0.012}$	$0.365^{+0.047}_{-0.046}$
73	< 9.36	$0.474^{+0.013}_{-0.012}$	$5.41^{+1.66}_{-1.66}$	$0.697^{+0.011}_{-0.014}$	$0.342^{+0.050}_{-0.045}$
74	$14.89^{+11.21}_{-11.17}$	$0.439^{+0.033}_{-0.041}$	$3.60^{+2.09}_{-2.09}$	$0.692^{+0.018}_{-0.016}$	$0.321^{+0.061}_{-0.062}$
75	< 16.20	$0.495^{+0.032}_{-0.045}$	$2.62^{+2.15}_{-2.16}$	$0.699^{+0.011}_{-0.013}$	$0.476^{+0.063}_{-0.060}$
76	< 10.11	$0.446^{+0.020}_{-0.024}$	$4.49^{+1.83}_{-1.74}$	$0.705^{+0.012}_{-0.014}$	$0.335^{+0.048}_{-0.046}$
77	< 9.44	$0.477^{+0.028}_{-0.021}$	$3.72^{+1.65}_{-1.65}$	$0.620^{+0.621}_{-0.620}$	< 0.143
78	< 12.37	$0.445^{+0.017}_{-0.017}$	$6.67^{+2.22}_{-2.21}$	$0.733^{+0.031}_{-0.031}$	$0.183^{+0.059}_{-0.062}$
79	< 19.31	$0.471^{+0.025}_{-0.030}$	$2.98^{+2.14}_{-2.03}$	$0.692^{+0.020}_{-0.022}$	$0.290^{+0.065}_{-0.064}$
80	< 9.24	$0.458^{+0.015}_{-0.015}$	$3.50^{+1.40}_{-1.32}$	$0.692^{+0.015}_{-0.016}$	$0.254^{+0.047}_{-0.045}$
81	< 12.13	$0.474^{+0.018}_{-0.016}$	$4.17^{+1.54}_{-1.56}$	$0.697^{+0.015}_{-0.013}$	$0.384^{+0.058}_{-0.061}$
82	< 10.10	$0.504^{+0.022}_{-0.016}$	$2.32^{+1.06}_{-1.06}$	$0.650^{+0.035}_{-0.026}$	$0.158^{+0.064}_{-0.067}$
83	< 14.66	$0.449^{+0.040}_{-0.123}$	$3.37^{+2.00}_{-2.03}$	$0.695^{+0.020}_{-0.015}$	$0.326^{+0.054}_{-0.057}$
84	< 11.72	$0.474^{+0.021}_{-0.022}$	$3.15^{+1.81}_{-1.64}$	$0.702^{+0.014}_{-0.014}$	$0.415^{+0.062}_{-0.061}$
85	< 19.83	$0.474^{+0.021}_{-0.020}$	$4.20^{+1.87}_{-1.97}$	$0.708^{+0.019}_{-0.017}$	$0.346^{+0.068}_{-0.066}$
86	$12.96^{+8.66}_{-8.67}$	$0.435^{+0.019}_{-0.013}$	$4.77^{+1.59}_{-1.45}$	$0.701^{+0.016}_{-0.016}$	$0.322^{+0.048}_{-0.052}$
87	< 9.11	$0.449^{+0.021}_{-0.025}$	$4.49^{+1.90}_{-1.94}$	$0.659^{+0.034}_{-0.026}$	$0.241^{+0.063}_{-0.074}$
88	< 15.55	$0.419^{+0.025}_{-0.019}$	$5.67^{+2.03}_{-1.98}$	$0.650^{+0.029}_{-0.029}$	$0.260^{+0.083}_{-0.084}$
89	$12.81^{+5.32}_{-5.34}$	$0.459^{+0.016}_{-0.010}$	$3.23^{+0.08}_{-0.08}$	$0.680^{+0.016}_{-0.014}$	$0.254^{+0.39}_{-0.041}$
90	< 16.62	-	-	$0.709^{+0.016}_{-0.016}$	$0.445^{+0.088}_{-0.084}$
91	$9.29^{+7.11}_{-7.12}$	$0.438^{+0.025}_{-0.026}$	$2.57^{+1.25}_{-1.38}$	$0.671^{+0.018}_{-0.014}$	$0.409^{+0.079}_{-0.075}$

Table 16 continued

Rev 1004	Fe flux[a]	Line[b]	Flux[c]	Edge[d]	τ[e]
92	$11.16^{+5.77}_{-5.65}$	$0.457^{+0.030}_{-0.088}$	$1.78^{+0.96}_{-0.90}$	$0.680^{+0.016}_{-0.012}$	$0.356^{+0.044}_{-0.044}$
93	< 5.76	$0.440^{+0.030}_{-0.047}$	$2.36^{+1.20}_{-1.13}$	$0.708^{+0.015}_{-0.015}$	$0.332^{+0.050}_{-0.051}$
94	$21.59^{+14.03}_{-7.91}$	$0.466^{+0.021}_{-0.023}$	$3.12^{+1.60}_{-1.46}$	$0.680^{+0.041}_{-0.038}$	$0.126^{+0.058}_{-0.060}$
95	< 16.01	$0.451^{+0.028}_{-0.025}$	$2.48^{+1.39}_{-1.37}$	$0.808^{+0.039}_{-0.037}$	$0.124^{+0.053}_{-0.055}$

REFERENCES CITED

Adams, T. F. 1977, ApJS, 33, 19

Alfvén, H. & Herlofson, N. 1950, Physical Review, 78, 616

Antonucci, R. 1993, ARA&A, 31, 473

Antonucci, R. R. J. & Miller, J. S. 1985, ApJ, 297, 621

Aretxaga, I., Le Mignant, D., Melnick, J., Terlevich, R. J., & Boyle, B. J. 1998, MNRAS, 298, L13

Arévalo, P., McHardy, I. M., Markowitz, A., Papadakis, I. E., Turner, T. J., Miller, L., & Reeves, J. 2008, MNRAS, 387, 279

Arnaud, K., Dorman, B., & Gordon, C. 2010, XSPEC An X-Ray Spectral Fitting Package: User's Guide for version 12.6.0, 12th edn., NASA/GSFC, Greenbelt, MD 20771

Arnaud, K. A. 1996, in Astronomical Society of the Pacific Conference Series, Vol. 101, Astronomical Data Analysis Software and Systems V, ed. G. H. Jacoby & J. Barnes, 17–+

Asaoka, I. 1989, PASJ, 41, 763

Aschenbach, B., Citterio, O., Ellwood, J. M., Jensen, P., Dekorte, P., Peacock, A., & Willingale, R. 1987, The high throughput X-ray Spectroscopy Mission. Report of the Telescope Working Group, 53–+

Baldwin, J. A., Robinson, L. B., Wampler, E. J., & Burbidge, E. M. 1975, ApJL, 195, L55

Ballantyne, D. R., Fabian, A. C., & Ross, R. R. 2002a, MNRAS, 329, L67

Ballantyne, D. R., Ross, R. R., & Fabian, A. C. 2002b, MNRAS, 336, 867

Balucinska-Church, M. & McCammon, D. 1992, ApJ, 400, 699

Bao, G. 1992, A&A, 257, 594

Barré, H., Nye, H., & Janin, G. 1999, ESA Bulletin, 100, 15

Barvainis, R. 1993, ApJ, 412, 513

Behar, E., Rasmussen, A. P., Blustin, A. J., Sako, M., Kahn, S. M., Kaastra, J. S., Branduardi-Raymont, G., & Steenbrugge, K. C. 2003, ApJ, 598, 232

Behar, E., Sako, M., & Kahn, S. M. 2001, ApJ, 563, 497

Behar, E., Sako, M., & Kahn, S. M. 2001, ApJ, 563, 497

Blandford, R. D. & Rees, M. J. 1978, PhysScr, 17, 265

Blandford, R. D. & Znajek, R. L. 1977, MNRAS, 179, 433

Block, D. L. & Sauvage, M. 2000, A&A, 353, 72

Boller, T., Brandt, W. N., Fabian, A. C., & Fink, H. H. 1997, MNRAS, 289, 393

Boller, T., Fabian, A. C., Sunyaev, R., Trümper, J., Vaughan, S., Ballantyne, D. R., Brandt, W. N., Keil, R., & Iwasawa, K. 2002, MNRAS, 329, L1

Boller, T., Tanaka, Y., Fabian, A., Brandt, W. N., Gallo, L., Anabuki, N., Haba, Y., & Vaughan, S. 2003, MNRAS, 343, L89

Branduardi-Raymont, G., Sako, M., Kahn, S. M., Brinkman, A. C., Kaastra, J. S., & Page, M. J. 2001, A&A, 365, L140

Canalizo, G., Max, C., Whysong, D., Antonucci, R., & Dahm, S. E. 2003, ApJ, 597, 823

Clavel, J., Wamsteker, W., & Glass, I. S. 1989, ApJ, 337, 236

Dahari, O. & De Robertis, M. M. 1988a, ApJS, 67, 249

—. 1988b, ApJ, 331, 727

de Chambure, D., Lainé, R., van Katwijk, K., & Kletzkine, P. 1999, ESA Bulletin, 100, 30

den Herder, J. W., Brinkman, A. C., Kahn, S. M., Branduardi-Raymont, G., Thomsen, K., Aarts, H., Audard, M., Bixler, J. V., den Boggende, A. J., Cottam, J., Decker, T., Dubbeldam, L., Erd, C., Goulooze, H., Güdel, M., Guttridge, P., Hailey, C. J., Janabi, K. A., Kaastra, J. S., de Korte, P. A. J., van Leeuwen, B. J., Mauche, C., McCalden, A. J., Mewe, R., Naber, A., Paerels, F. B., Peterson, J. R., Rasmussen, A. P., Rees, K., Sakelliou, I., Sako, M., Spodek, J., Stern, M., Tamura, T., Tandy, J., de Vries, C. P., Welch, S., & Zehnder, A. 2001, A&A, 365, L7

Dickey, J. M. & Lockman, F. J. 1990, ARA&A, 28, 215

Draine, B. T. & Lee, H. M. 1984, ApJ, 285, 89

Edelson, R., Turner, T. J., Pounds, K., Vaughan, S., Markowitz, A., Marshall, H., Dobbie, P., & Warwick, R. 2002, ApJ, 568, 610

Elvis, M., Maccacaro, T., Wilson, A. S., Ward, M. J., Penston, M. V., Fosbury, R. A. E., & Perola, G. C. 1978, MNRAS, 183, 129

Epstein, E. E., Fogarty, W. G., Hackney, K. R., Hackney, R. L., Leacock, R. J., Pomphrey, R. B., Scott, R. L., Smith, A. G., Hawkins, R. W., Roeder, R. C., Gary, B. L., Penston, M. V., Tritton, K. P., Bertaud, C., Véron, M. P., Wlérick, G., Bernard, A., Bigay, J. H., Merlin, P., Durand, A., Sause, G., Becklin, E. E., Neugebauer, G., & Wynn-Williams, C. G. 1972, ApJL, 178, L51+

Fanaroff, B. L. & Riley, J. M. 1974, MNRAS, 167, 31P

Fath, E. A. 1909, Lick Observatory Bulletin, 5, 71

Fukue, J. 2003, PASJ, 55, 1121

Fukumura, K. 2006, PhD thesis, Montana State University

Gallo, L. C., Tanaka, Y., Boller, T., Fabian, A. C., Vaughan, S., & Brandt, W. N. 2004, MNRAS, 353, 1064

Greenstein, J. L. 1963, Nature, 197, 1041

Greenstein, J. L. & Matthews, T. A. 1963, Nature, 197, 1041

Grupe, D., Beuermann, K., Thomas, H.-C., Mannheim, K., & Fink, H. H. 1998, A&A, 330, 25

Grupe, D., Mathur, S., & Komossa, S. 2004, ApJ, 127, 3161

Guainazzi, M., Nicastro, F., Fiore, F., Matt, G., McHardy, I., Orr, A., Barr, P., Fruscione, A., Papadakis, I., Parmar, A. N., Uttley, P., Perola, G. C., & Piro, L. 1998, MNRAS, 301, L1

Guilbert, P. W. & Rees, M. J. 1988, MNRAS, 233, 475

Haardt, F. & Maraschi, L. 1991, ApJL, 380, L51

Haardt, F., Maraschi, L., & Ghisellini, G. 1994, ApJL, 432, L95

Haba, Y., Kunieda, H., Misaki, K., Terashima, Y., Kaastra, J. S., Mewe, R., Fabian, A. C., & Iwasawa, K. 2003, ApJ, 599, 949

Haba, Y., Liebmann, A. C., Fukumura, K., Kunieda, H., & Tsuruta, S. 2008, PASJ, 60, 1257

Halpern, J. P. 1984, ApJ, 281, 90

Heckman, T. M., Blitz, L., Wilson, A. S., Armus, L., & Miley, G. K. 1989, ApJ, 342, 735

Iwasawa, K., Fabian, A. C., Mushotzky, R. F., Brandt, W. N., Awaki, H., & Kunieda, H. 1996a, MNRAS, 279, 837

Iwasawa, K., Fabian, A. C., Reynolds, C. S., Nandra, K., Otani, C., Inoue, H., Hayashida, K., Brandt, W. N., Dotani, T., Kunieda, H., Matsuoka, M., & Tanaka, Y. 1996b, MNRAS, 282, 1038

Jansen, F., Lumb, D., Altieri, B., Clavel, J., Ehle, M., Erd, C., Gabriel, C., Guainazzi, M., Gondoin, P., Much, R., Munoz, R., Santos, M., Schartel, N., Texier, D., & Vacanti, G. 2001, A&A, 365, L1

Kahn, S. M. 1990, in IAU Colloq. 115: High Resolution X-ray Spectroscopy of Cosmic Plasmas, ed. P. Gorenstein & M. Zombeck, 365–375

Kallman, T. R. 2010, XSTAR - A Spectral Analysis Tool, 2nd edn., NASA/GSF, Greenbelt, MD

Karas, V. 1996, ApJ, 470, 743

Karas, V. & Bao, G. 1992, A&A, 257, 531

Kaspi, S., Brandt, W. N., George, I. M., Netzer, H., Crenshaw, D. M., Gabel, J. R., Hamann, F. W., Kaiser, M. E., Koratkar, A., Kraemer, S. B., Kriss, G. A., Mathur, S., Mushotzky, R. F., Nandra, K., Peterson, B. M., Shields, J. C., Turner, T. J., & Zheng, W. 2002, ApJ, 574, 643

Kato, S., Fukue, J., & Mineshige, S. 2008, Black-Hole Accretion Disks Towards a New Paradigm (Kyoto University Press)

Kawaguchi, T. 2003, ApJ, 593, 69

Khachikian, E. Y. & Weedman, D. W. 1974, ApJ, 192, 581

Krolik, J. H. 1999, Active Galactic Nuclei: From the Central Black Hole to the Galactic Environment, Princeton Series in Astrophysics (Princeton University Press)

Kunieda, H., Hayakawa, S., Tawara, Y., Koyama, K., Tsuruta, S., & Leighly, K. 1992, ApJ, 384, 482

Lamer, G., McHardy, I. M., Uttley, P., & Jahoda, K. 2003, MNRAS, 338, 323

Laor, A. 1991, ApJ, 376, 90

Lebofsky, M. J. & Rieke, G. H. 1980, Nature, 284, 410

Lee, J. C., Ogle, P. M., Canizares, C. R., Marshall, H. L., Schulz, N. S., Morales, R., Fabian, A. C., & Iwasawa, K. 2001, ApJL, 554, L13

Lehnert, M. D., van Breugel, W. J. M., Heckman, T. M., & Miley, G. K. 1999, ApJS, 124, 11

Leighly, K. M., Mushotzky, R. F., Yaqoob, T., Kunieda, H., & Edelson, R. 1996, ApJ, 469, 147

Levenson, N. A., Weaver, K. A., & Heckman, T. M. 2001, ApJS, 133, 269

Liedahl, D. A., Osterheld, A. L., & Goldstein, W. H. 1995, ApJL, 438, L115

Lightman, A. P. & White, T. R. 1988, ApJ, 335, 57

Machida, M. & Matsumoto, R. 2003, ApJ, 585, 429

Magdziarz, P. & Zdziarski, A. A. 1995, MNRAS, 273, 837

Markowitz, A., Papadakis, I., Arévalo, P., Turner, T. J., Miller, L., & Reeves, J. N. 2007, ApJ, 656, 116

Mason, K. O., Branduardi-Raymont, G., Ogle, P. M., Page, M. J., Puchnarewicz, E. M., Behar, E., Córdova, F. A., Davis, S., Maraschi, L., McHardy, I. M., O'Brien, P. T., Priedhorsky, W. C., & Sasseen, T. P. 2003, ApJ, 582, 95

Mason, K. O., Breeveld, A., Much, R., Carter, M., Cordova, F. A., Cropper, M. S., Fordham, J., Huckle, H., Ho, C., Kawakami, H., Kennea, J., Kennedy, T., Mittaz, J., Pandel, D., Priedhorsky, W. C., Sasseen, T., Shirey, R., Smith, P., & Vreux, J.-M. 2001, A&A, 365, L36

Mathur, S., Elvis, M., & Wilkes, B. 1995, ApJ, 452, 230

McHardy, I. 1988, Memorie della Societa Astronomica Italiana, 59, 239

McHardy, I. M., Papadakis, I. E., Uttley, P., Page, M. J., & Mason, K. O. 2004, MNRAS, 348, 783

McLeod, K. K. & McLeod, B. A. 2001, ApJ, 546, 782

Merloni, A. & Fabian, A. C. 2001, MNRAS, 328, 958

Mewe, R., Gronenschild, E. H. B. M., & van den Oord, G. H. J. 1985, A&AS, 62, 197

Mewe, R., Lemen, J. R., & van den Oord, G. H. J. 1986, A&AS, 65, 511

Miller, J. S. & Goodrich, R. W. 1990, ApJ, 355, 456

Miller, L., Turner, T. J., Reeves, J. N., George, I. M., Kraemer, S. B., & Wingert, B. 2007, A&A, 463, 131

Miller, L., Turner, T. J., Reeves, J. N., George, I. M., Porquet, D., Nandra, K., & Dovciak, M. 2006, A&A, 453, L13

Mineshige, S., Kawaguchi, T., Takeuchi, M., & Hayashida, K. 2000, PASJ, 52, 499

Mineshige, S., Takeuchi, M., & Nishimori, H. 1994, ApJL, 435, L125

Miniutti, G. & Fabian, A. C. 2004, MNRAS, 349, 1435

Murphy, E. M., Lockman, F. J., Laor, A., & Elvis, M. 1996, ApJS, 105, 369

Mushotzky, R. F., Done, C., & Pounds, K. A. 1993, ARA&A, 31, 717

Nagakura, H. & Yamada, S. 2008, ApJL, 689, 391

—. 2009, ApJ, 696, 2026

Nandra, K., George, I. M., Mushotzky, R. F., Turner, T. J., & Yaqoob, T. 1997a, ApJ, 476, 70

—. 1997b, ApJ, 477, 602

Nandra, K., O'Neill, P. M., George, I. M., & Reeves, J. N. 2007, MNRAS, 382, 194

Nandra, K. & Pounds, K. A. 1994, MNRAS, 268, 405

Negoro, H., Kitamoto, S., & Mineshige, S. 2001, ApJ, 554, 528

Netzer, H., Kaspi, S., Behar, E., Brandt, W. N., Chelouche, D., George, I. M., Crenshaw, D. M., Gabel, J. R., Hamann, F. W., Kraemer, S. B., Kriss, G. A., Nandra, K., Peterson, B. M., Shields, J. C., & Turner, T. J. 2003, ApJ, 599, 933

Ogle, P. M., Mason, K. O., Page, M. J., Salvi, N. J., Cordova, F. A., McHardy, I. M., & Priedhorsky, W. C. 2004, ApJ, 606, 151

Ohsuga, K., Mineshige, S., & Watarai, K. 2003, ApJ, 596, 429

Oke, J. B. & Gunn, J. E. 1974, ApJL, 189, L5+

Osterbrock, D. E. 1978, PhysScr, 17, 137

—. 1981, ApJ, 249, 462

Osterbrock, D. E. & Ferland, G. J. 2006, Astrophysics of Gaseous Nebuae and Active Galactic Nuclei, 2nd edn. (University Science Books)

Osterbrock, D. E. & Pogge, R. W. 1985, ApJ, 297, 166

Page, M. J., Mason, K. O., Carrera, F. J., Clavel, J., Kaastra, J. S., Puchnarewicz, E. M., Santos-Lleo, M., Brunner, H., Ferrigno, C., George, I. M., Paerels, F., Pounds, K. A., & Trudolyubov, S. P. 2001, A&A, 365, L152

Papadakis, I. E. & Lawrence, A. 1993, MNRAS, 261, 612

Peterson, B. M. 1997, An Introduction to Active Galactic Nuclei (Cambridge University Press)

Ponti, G., Cappi, M., Dadina, M., & Malaguti, G. 2004, A&A, 417, 451

Ponti, G., Miniutti, G., Cappi, M., Maraschi, L., Fabian, A. C., & Iwasawa, K. 2006, MNRAS, 368, 903

Pounds, K. A., Reeves, J. N., King, A. R., & Page, K. L. 2004, MNRAS, 350, 10

Pounds, K. A., Reeves, J. N., Page, K. L., Wynn, G. A., & O'Brien, P. T. 2003, MNRAS, 342, 1147

Rafanelli, P., Schulz, H., Barbieri, C., Komossa, S., Mebold, U., Baruffolo, A., & Radovich, M. 1997, A&A, 327, 901

Ranalli, P., Comastri, A., & Setti, G. 2003, A&A, 399, 39

Rees, M. J., Silk, J. I., Werner, M. W., & Wickramasinghe, N. C. 1969, Nature, 223, 788

Reynolds, C. S. 1997, MNRAS, 286, 513

Rieke, G. H. 1978, ApJ, 226, 550

Rodriguez-Ardila, A. & Viegas, S. M. 2003, MNRAS, 340, L33

Ross, R. R. & Fabian, A. C. 1993, MNRAS, 261, 74

—. 2005, MNRAS, 358, 211

Ross, R. R., Fabian, A. C., & Mineshige, S. 1992, MNRAS, 258, 189

Ross, R. R., Fabian, A. C., & Young, A. J. 1999, MNRAS, 306, 461

Ross, R. R., Weaver, R., & McCray, R. 1978, ApJ, 219, 292

Ryle, M. & Sandage, A. 1964, ApJ, 139, 419

Sako, M., Kahn, S. M., Behar, E., Kaastra, J. S., Brinkman, A. C., Boller, T., Puchnarewicz, E. M., Starling, R., Liedahl, D. A., Clavel, J., & Santos-Lleo, M. 2001, A&A, 365, L168

Sako, M., Kahn, S. M., Branduardi-Raymont, G., Kaastra, J. S., Brinkman, A. C., Page, M. J., Behar, E., Paerels, F., Kinkhabwala, A., Liedahl, D. A., & den Herder, J. W. 2003, ApJ, 596, 114

Sanders, D. B., Phinney, E. S., Neugebauer, G., Soifer, B. T., & Matthews, K. 1989, ApJ, 347, 29

Schmidt, M. 1963, Nature, 197, 1040

—. 1969, ARRS, 7, 527

Schmitt, J. L. 1968, Nature, 218, 663

Seyfert, C. K. 1943, ApJ, 97, 28

Shakura, N. I. & Sunyaev, R. A. 1973, A&A, 24, 337

Shklovskii, I. S. 1953, Radioastronomiia., ed. Shklovskii, I. S.

Slipher, V. M. 1917, Lowell Observatory Bulletin, 3, 59

Strüder, L., Briel, U., Dennerl, K., Hartmann, R., Kendziorra, E., Meidinger, N., Pfeffermann, E., Reppin, C., Aschenbach, B., Bornemann, W., Bräuninger, H., Burkert, W., Elender, M., Freyberg, M., Haberl, F., Hartner, G., Heuschmann, F., Hippmann, H., Kastelic, E., Kemmer, S., Kettenring, G., Kink, W., Krause, N., Müller, S., Oppitz, A., Pietsch, W., Popp, M., Predehl, P., Read, A., Stephan, K. H., Stötter, D., Trümper, J., Holl, P., Kemmer, J., Soltau, H., Stötter, R., Weber, U., Weichert, U., von Zanthier, C., Carathanassis, D., Lutz, G., Richter, R. H., Solc, P., Böttcher, H., Kuster, M., Staubert, R., Abbey, A., Holland, A., Turner, M., Balasini, M., Bignami, G. F., La Palombara, N., Villa, G., Buttler, W., Gianini, F., Lainé, R., Lumb, D., & Dhez, P. 2001, A&A, 365, L18

Tanaka, Y., Nandra, K., Fabian, A. C., Inoue, H., Otani, C., Dotani, T., Hayashida, K., Iwasawa, K., Kii, T., Kunieda, H., Makino, F., & Matsuoka, M. 1995, Nature, 375, 659

Tarter, C. B., Tucker, W. H., & Salpeter, E. E. 1969, ApJ, 156, 943

Taylor, R. D., Uttley, P., & McHardy, I. M. 2003, MNRAS, 342, L31

Timmer, J. & Koenig, M. 1995, A&A, 300, 707

Tornikoski, M., Valtaoja, E., Terasranta, H., Lainela, M., Bramwell, M., & Botti, L. C. L. 1993, AJ, 105, 1680

Tran, H. D., Miller, J. S., & Kay, L. E. 1992, ApJ, 397, 452

Turner, M. J. L., Abbey, A., Arnaud, M., Balasini, M., Barbera, M., Belsole, E., Bennie, P. J., Bernard, J. P., Bignami, G. F., Boer, M., Briel, U., Butler, I., Cara, C., Chabaud, C., Cole, R., Collura, A., Conte, M., Cros, A., Denby, M., Dhez, P., Di Coco, G., Dowson, J., Ferrando, P., Ghizzardi, S., Gianotti, F., Goodall, C. V., Gretton, L., Griffiths, R. G., Hainaut, O., Hochedez, J. F., Holland, A. D., Jourdain, E., Kendziorra, E., Lagostina, A., Laine, R., La Palombara, N., Lortholary, M., Lumb, D., Marty, P., Molendi, S., Pigot, C., Poindron, E., Pounds, K. A., Reeves, J. N., Reppin, C., Rothenflug, R., Salvetat, P., Sauvageot, J. L., Schmitt, D., Sembay, S., Short, A. D. T., Spragg, J., Stephen, J., Strüder, L., Tiengo, A., Trifoglio, M., Trümper, J., Vercellone, S., Vigroux, L., Villa, G., Ward, M. J., Whitehead, S., & Zonca, E. 2001, A&A, 365, L27

Turner, T. J., Miller, L., Reeves, J. N., & Kraemer, S. B. 2007, A&A, 475, 121

Ulrich, M. 1988, MNRAS, 230, 121

Uttley, P., McHardy, I. M., & Vaughan, S. 2005, MNRAS, 359, 345

Uttley, P., Taylor, R. D., McHardy, I. M., Page, M. J., Mason, K. O., Lamer, G., & Fruscione, A. 2004, MNRAS, 347, 1345

van der Klis, M. 1997, in Statistical Challenges in Modern Astronomy II, ed. G. J. Babu & E. D. Feigelson, 321–+

van Katwijk, K., van der Laan, T., & Stramaccioni, D. 1999, ESA Bulletin, 100, 44

Vaughan, S., Edelson, R., Warwick, R. S., & Uttley, P. 2003a, MNRAS, 345, 1271

Vaughan, S. & Fabian, A. C. 2003, MNRAS, 341, 496

—. 2004, MNRAS, 348, 1415

Vaughan, S., Fabian, A. C., & Nandra, K. 2003b, MNRAS, 339, 1237

Verner, D. A., Ferland, G. J., Korista, K. T., & Yakovlev, D. G. 1996, ApJ, 465, 487

von Montigny, C., Bertsch, D. L., Chiang, J., Dingus, B. L., Esposito, J. A., Fichtel, C. E., Fierro, J. M., Hartman, R. C., Hunter, S. D., Kanbach, G., Kniffen, D. A., Lin, Y. C., Mayer-Hasselwander, H. A., Michelson, P. F., Nolan, P. L., Radecke, H. D., Schneid, E., Sreekumar, P., Thompson, D. J., & Willis, T. 1995, A&A, 299, 680

Wada, K. & Norman, C. A. 2002, ApJL, 566, L21

Weedman, D. W. 1976, ApJ, 208, 30

Wills, B. J., Grupe, D., & Leighly, K. 2007, in Bulletin of the American Astronomical Society, Vol. 38, Bulletin of the American Astronomical Society, 795–+

Wilson, A. S. & Colbert, E. J. M. 1995, ApJ, 438, 62

Woo, J. & Urry, C. M. 2002, ApJ, 579, 530

Yan, M., Sadeghpour, H. R., & Dalgarno, A. 1998, ApJ, 496, 1044

Zdziarski, A. A., Johnson, W. N., Done, C., Smith, D., & McNaron-Brown, K. 1995, ApJL, 438, L63